

HEAT TRANSFER AND CONVECTION

IN LIQUID METAL

By

CHRISTINE ELIZABETH HARRISON

B.Sc., The University of British Columbia, 1981

A THESIS SUBMITTED IN PARTIAL FULFILLMENT OF
THE REQUIREMENTS FOR THE DEGREE OF
MASTER OF APPLIED SCIENCE

in

THE FACULTY OF GRADUATE STUDIES
(Department of Metallurgical Engineering)

We accept this thesis as conforming
to the required standard

THE UNIVERSITY OF BRITISH COLUMBIA

April 1984

© CHRISTINE ELIZABETH HARRISON, 1984

In presenting this thesis in partial fulfilment of the requirements for an advanced degree at the University of British Columbia, I agree that the Library shall make it freely available for reference and study. I further agree that permission for extensive copying of this thesis for scholarly purposes may be granted by the head of my department or by his or her representatives. It is understood that copying or publication of this thesis for financial gain shall not be allowed without my written permission.

Department of METALLURGICAL ENGINEERING

The University of British Columbia
1956 Main Mall
Vancouver, Canada
V6T 1Y3

Date April 26, 1984

ABSTRACT

This investigation was undertaken to examine the heat flow characteristics of a liquid metal system in which fluid flow is present due to buoyancy forces. Previous investigations of heat flow in liquids has been confined to transparent materials, which have very different flow characteristics compared to liquid metals.

Measurements were made on liquid tin contained in a thin square cavity which had a temperature difference imposed across the cell to produce natural convection. The heat flow across the cell was calculated from the measured temperature difference across the cold end plate and the thermal conductivity of the plate. Using the calculated heat flow and the measured temperature difference across the melt the effective thermal conductivity of the melt was calculated. Two cell sizes were studied. The thermal conductivity of the cold end plate was found to have a significant effect on the heat transfer through the cell.

Radioactive tracers were used to observe the flow pattern in the melt and to measure the flow velocity as a function of the temperature difference across the cell. The technique involved insertion of radioactive Sn^{113} into the melt, then quenching the sample after a given

length of time. The sample was then autoradiographed to determine the path of the tracer after insertion into the melt. The flow was found to be very fast for the smaller of the two cell sizes which exhibited three-dimensional flow characteristics. The larger cell produced laminar, two-dimensional flow. A correlation was observed between the time per cycle and the temperature difference across the large cell.

The study also includes a finite-difference model which was developed to provide further insight into the thermal and fluid flow behaviour of the melt. The model examines the effect of nonuniform temperatures along the ends and bottom of the cell on the temperature and velocity fields and is used to compare the response of liquid tin and liquid steel to identical temperature differences. Results from the model indicate that either a temperature drop along the hot and cold ends of the cell or the presence of a linear gradient along the bottom of the cell would decrease the maximum fluid velocity in the cell.

The present investigation shows that the enhancement of the thermal conductivity due to the presence of natural convection in the liquid metal can be as high as ten times the stagnant thermal conductivity. However the degree of enhancement is influenced by the thermal resistance at the boundaries.

TABLE OF CONTENTS

1.0 INTRODUCTION	
1.1 Fluid Flow	1
1.1.1 Natural convection	2
1.1.2 Forced convection	7
1.2 Convection In Industrial Processes	10
1.3 Examination Of Previous Investigations	12
1.4 Heat Transfer Analysis	16
2.0 EXPERIMENTAL DESIGN	
2.1 Design Of Experimental Cells	22
2.1.1 Cell I	24
2.1.2 Cell II	26
2.1.3 Cell III	27
2.2 Fluid Flow Measurement	29
2.3 Temperature Measurement	31
3.0 EXPERIMENTAL RESULTS	
3.1 Results From Cell I	34
3.1.1 Calculation of effective thermal conductivity	34
3.1.2 Discussion of results from cell I	37
3.2 Results From Cell II	38
3.3 Results From Cell III	40
3.3.1 Results of quench tests	42
3.3.2 Temperature measurement	49

3.0 EXPERIMENTAL RESULTS(cont'd)

3.3 Results From Cell III (Continued)

3.3.3 Calculation of effective thermal conductivity	57
---	----

4.0 MATHEMATICAL MODEL

4.1 Governing Equations	60
-------------------------	----

4.1.1 Dimensionless variables	63
-------------------------------	----

4.1.2 Stream function and vorticity	65
-------------------------------------	----

4.2 Initial And Boundary Conditions	67
-------------------------------------	----

4.3 Finite Difference Equations	68
---------------------------------	----

4.4 Results Of Computer Runs	75
------------------------------	----

5.0 SUMMARY REMARKS	97
---------------------	----

REFERENCE LIST	100
----------------	-----

APPENDIX I. List of Symbols	102
-----------------------------	-----

APPENDIX II. Chart for Argon Flow Rate Conversion	104
---	-----

APPENDIX III. Computer Program	105
--------------------------------	-----

LIST OF TABLES

	PAGE
TABLE I Comparison of Fluid Properties	5
TABLE II Properties of Liquid Tin	23
TABLE III Comparison of Thermal Resistances	39
TABLE IV Calculation of Effective Thermal Conductivity	58

LIST OF FIGURES

	PAGE
FIGURE 1.1 Fluid flow progression after start of casting. ¹	3
FIGURE 1.2 Flow patterns induced by electromagnetic stirring. ¹⁶	8
FIGURE 1.3 Effect of input stream on fluid flow in liquid pool (a) Flow patterns induced by different types of input streams ¹⁷ (b) Example of how input stream induces flow below the mould. ¹⁸	9
FIGURE 1.4 Fluid flow at solid-liquid interface. ¹⁹	11
FIGURE 1.5 Convection currents in a solidifying ingot. ²⁰	11
FIGURE 1.6 Temperature isotherms for (a) purely conductive heat flow and (b) convective heat flow ($T_2 > T_1$). ⁸	13
FIGURE 1.7 Vertical (x) velocity plotted versus horizontal position across mid-plane of cavity ($x=0.5$) according to (a) the analytical model of Batchelor and (b) the numerical model of Stewart which shows velocity profiles for $Pr=0.0127$ and various Grashof numbers.	15
FIGURE 1.8 Correlation observed by Stewart between the time to complete one cycle around cell and the temperature difference across the cell for average melt temperatures of 237°C, 260°C and 305°C. ⁸	17
FIGURE 1.9 Radiographs from experiments of Stewart showing (a) two-dimensional laminar flow and (b) three-dimensional vortex flow. ⁸	18
FIGURE 2.1 Design of experimental cell I	25
FIGURE 2.2 Design of experimental cell III	28
FIGURE 2.3 Location of thermocouples in experimental cells a) cell I, b) cell II and c) cell III (thermocouple location is marked by T).	32

- FIGURE 3.1 Graph showing results from cell I with top of cell covered and uncovered. Slopes were calculated using linear regression of data points. The correlation coefficient is given in brackets. 35
- FIGURE 3.2 Quenched samples from cell II (a) Tracer is well mixed ($\Delta T = 6^{\circ}\text{C}$, time prior to quench ≈ 30 sec), (b) Sample showing vortex motion ($\Delta T = 8^{\circ}\text{C}$, time prior to quench ≈ 30 sec), (c) Sample exhibiting turbulent flow ($\Delta T = 5^{\circ}\text{C}$, time prior to quench ≈ 25 sec). 41
- FIGURE 3.3 Examples of inadequate quenches from cell III (a) Sample quenched by rapidly filling inside of furnace with water and (b) Sample quenched using water jets aimed at side walls. 43
- FIGURE 3.4 Successful quench sample achieved using composite cell wall design. 44
- FIGURE 3.5 Quenched samples from cell III (a) $\Delta T = 7.6^{\circ}\text{C}$, time prior to quench = 20 sec (b) $\Delta T = 7.2^{\circ}\text{C}$, time prior to quench = 21 sec. 45
- FIGURE 3.5 (Continued) Quenched samples from cell III (c) $\Delta T = 1.4^{\circ}\text{C}$, time prior to quench = 22 sec, (d) $\Delta T = 4.4^{\circ}\text{C}$, time prior to quench = 11 sec. 46
- FIGURE 3.5 (Continued) Quenched samples from cell III (e) $\Delta T = 2.4^{\circ}\text{C}$, time prior to quench = 18 sec. 47
- FIGURE 3.6 Relationship between time required per cycle and the temperature difference across the melt (Temperatures in melt were measured using a thermocouple probe). 48
- FIGURE 3.7 Graph of temperature differences across cold end versus temperature difference across melt for (a) experiment A which used a heater and argon cooling to produce the temperature difference across melt. Slopes indicated on graph were calculated using linear regression of data points. 50

FIGURE 3.7	(Continued) Graph of temperature differences across cold end versus temperature difference across melt for b) experiment B which only used argon cooling to produce the temperature difference across melt. Slopes indicated on graph were calculated using linear regression of data points.	51
FIGURE 3.8	Graphs showing behaviour of temperature differences across (a) the cold end and (b) the melt versus argon flow rate for experiment A.	53
FIGURE 3.9	Graphs showing behaviour of temperature differences across (a) the cold end and (b) the melt versus argon flow rate for experiment B.	54
FIGURE 3.10	Graphs of temperature at centre of outside face of cold end versus argon flow rate for (a) experiment A and (b) experiment B.	55
FIGURE 4.1	System of reference for mathematical model.	61
FIGURE 4.2	Grid system used in mathematical model.	70
FIGURE 4.3	Isotherm distribution for $Pr=0.0127$ and (a) $Gr=1.0 \times 10^4$, (b) $Gr=1.0 \times 10^5$ and (c) $Gr=1.0 \times 10^6$.	77
FIGURE 4.4	Streamline plot for $Pr=0.0127$ and (a) $Gr=1.0 \times 10^4$, (b) $Gr=1.0 \times 10^5$ and (c) $Gr=1.0 \times 10^6$.	78
FIGURE 4.5	Nusselt number versus vertical (x) position along cold wall for $Pr=0.0127$ and $Gr=1.0 \times 10^4$, 1.0×10^5 and 1.0×10^6 .	79
FIGURE 4.6	Normalized velocity field for $Pr=0.0127$ and (a) $Gr=10^5$ (maximum velocity = 487.44) and (b) $Gr=10^6$ (maximum velocity = 1185.09). Velocities given are dimensionless velocities.	80
FIGURE 4.7	Isotherm plots with $Pr=0.0127$ and $Gr=1.0 \times 10^5$. Solid line indicates profiles for isothermal ends and dashed line indicates those for (a) a 5% drop along ends and (b) a 10% drop along ends.	81

- FIGURE 4.8 Isotherm plots with $Pr=0.0127$ and $Gr=1.0 \times 10^6$. Solid line indicates profiles for isothermal ends and dashed line indicates those for (a) a 5% drop along ends and (b) a 10% drop along ends. 82
- FIGURE 4.9 Streamline plot with $Pr=0.0127$ and $Gr=1.0 \times 10^6$ with (a) isothermal ends and (b) 10% drop along both ends (with coldest temperature at top). 83
- FIGURE 4.10 Isotherm plot with linear temperature gradient along bottom (isothermal ends and insulated top surface) with $Pr=0.0127$ and (a) $Gr=1.0 \times 10^5$ and (b) $Gr=1.0 \times 10^6$. 85
- FIGURE 4.11 Streamline plots with linear temperature gradient along bottom (isothermal ends and insulated top surface) with $Pr=0.0127$ and (a) $Gr=1.0 \times 10^5$ and (b) $Gr=1.0 \times 10^6$. 86
- FIGURE 4.12 Isotherm plots with linear temperature gradient along bottom and 10% temperature drop along ends with $Pr=0.0127$ and (a) $Gr=1.0 \times 10^5$ and (b) $Gr=1.0 \times 10^6$. 87
- FIGURE 4.13 Isotherm distribution for a temperature difference of 0.01°C across cell for (a) liquid tin ($Pr=0.0127$ and $Gr=3.6 \times 10^4$) and (b) liquid steel ($Pr=0.11$ and $Gr=6.0 \times 10^3$). 89
- FIGURE 4.14 Isotherm distribution for a temperature difference of 0.5°C across cell for (a) liquid tin ($Pr=0.0127$ and $Gr=1.8 \times 10^6$) and (b) liquid steel ($Pr=0.0127$ and $Gr=3.0 \times 10^5$). 90
- FIGURE 4.15 Streamline distribution for a temperature difference of 0.01°C across cell for (a) liquid tin ($Pr=0.0127$ and $Gr=3.6 \times 10^4$) and (b) liquid steel ($Pr=0.11$ and $Gr=6.0 \times 10^3$). 91
- FIGURE 4.16 Streamline distribution for a temperature difference of 0.5°C across cell for (a) liquid tin ($Pr=0.0127$ and $Gr=1.8 \times 10^6$) and (b) liquid steel ($Pr=0.11$ and $Gr=3.0 \times 10^5$). 92
- FIGURE 4.17 Vertical (x) velocity versus horizontal (y) position at $x=0.5$ for a temperature difference of 0.01°C across cell in (a) liquid tin ($Pr=0.0127$ and $Gr=3.6 \times 10^4$) and (b) liquid steel ($Pr=0.11$ and $Gr=6.0 \times 10^3$). 93

FIGURE 4.18 Vertical (x) velocity versus horizontal (y) position at $x=0.5$ for a temperature difference of 0.5°C across cell in (a) liquid tin ($\text{Pr}=0.0127$ and $\text{Gr}=1.8\times 10^6$) and (b) liquid steel ($\text{Pr}=0.11$ and $\text{Gr}=3.0\times 10^5$).

94

FIGURE 4.19 Plot of local Nusselt number versus position along cold wall for tin and steel at temperature differences of 0.01°C and 0.5°C .

95

ACKNOWLEDGEMENTS

I would like to thank my supervisor, Dr. Fred Weinberg for his patience and guidance throughout this investigation. I would also like to thank the technical staff at the Department of Metallurgy for their valuable assistance during the course of this work.

Financial support was provided by the Alcan Fellowship and a grant from the National Science and Engineering Council.

1. INTRODUCTION

An analysis of many metallurgical processes involves knowledge of the temperature distribution in the system. In recent years this problem has been approached by using a heat transfer mathematical model analysis to estimate thermal profiles. To do this analysis requires data related to boundary conditions and thermal properties of the materials involved. If the system contains liquid the task becomes more difficult since heat flow through a liquid is markedly influenced by fluid flow in the liquid. Such is the case for solidification processes in large ingots, continuous casting and crystal growth as well as heat loss determinations in ladles and tundishes. No quantitative information is available for heat transfer in a liquid metal with fluid flow present. In practise, an estimated heat transfer coefficient is used which consists of the atomic thermal conductivity multiplied by an arbitrary number.

The present investigation was undertaken to determine the heat transfer through a liquid metal with known fluid flow in the melt.

1.1 FLUID FLOW

Fluid flow in a liquid metal can result from natural convection or be induced by mechanical or electrical means to produce forced

convection in the liquid.

1.1.1 Natural Convection

Natural convection is caused by thermal or compositional gradients which give rise to density changes in the fluid. The effect of the buoyancy force produces the fluid motion. Thermal convection can be present even at very low temperature differences as shown by Cole and Bolling¹ in Figure 1.1. Compositional differences are almost always produced during solidification as solute segregates into the melt. Convection from this cause is most pronounced when the solute and solvent are significantly different in density. Such density differences cause complex flow patterns which change appreciably with time and are therefore difficult to clearly define.

The geometry and physical properties of the system greatly affect the fluid flow. The geometry refers to the shape of the boundaries and the presence of any barrier in the fluid. In many cases the boundaries can be very involved, which is especially true for solidification where the size and shape of the liquid pool is continually changing with time. In addition the boundary itself is not clear, consisting of a partially solid and liquid region. The system is too complicated to investigate directly and a simpler steady-state geometry is required.

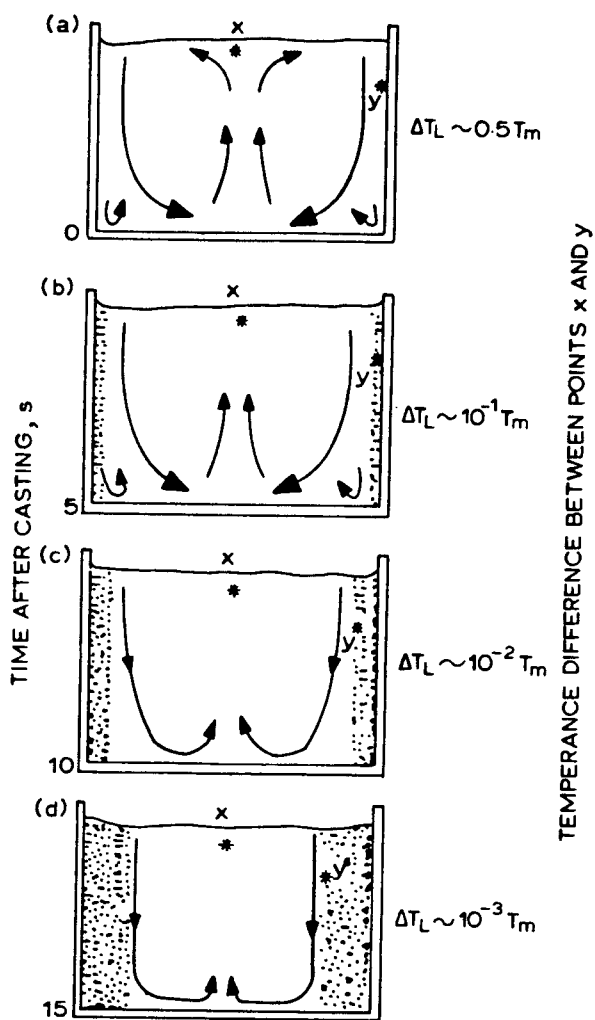


FIGURE 1.1 Fluid flow progression after start of casting.¹

Many of the studies on heat transfer and natural convection have been undertaken because of the interest in heat transfer in nuclear reactors, solar collectors and other industrial systems. Consequently the geometries studied have attempted to duplicate the pipes and ducts encountered in these applications. These geometries often cannot be directly related to those encountered in liquid pools in solidification or other applications where large volumes of liquid metal are contained in a vessel, which makes it difficult to apply the heat transfer results.

In addition, most studies have been made using transparent materials such as water, oils and gases. The physical properties of these fluids differ markedly from those of liquid metals, as shown in Table I. The disparity is particularly pronounced in the values of the density and thermal conductivity.

To understand the significance of the differences in the physical properties it is useful to look at the dimensionless parameters that are of importance to natural convection, namely the Grashof number and the Prandtl number. The Grashof number, Gr is the ratio of the buoyancy force times the inertia force over the shear force squared and is defined as follows:

$$Gr = \frac{\beta g L^3 \Delta T}{\nu^2} \quad (1.1.1)$$

TABLE I COMPARISON OF FLUID PROPERTIES

FLUID	VISCOSITY (cp)	SPECIFIC HEAT $\left(\frac{\text{cal}}{\text{gm} \cdot ^\circ\text{C}}\right)$	THERMAL CONDUCTIVITY $\left(\frac{\text{cal}}{\text{cm} \cdot \text{sec} \cdot ^\circ\text{C}}\right)$	DENSITY $\left(\frac{\text{gm}}{\text{cm}^3}\right)$	THERMAL COEFFICIENT OF EXPANSION $\left(\frac{1}{^\circ\text{C}}\right)$	PRANDTL NUMBER	GRASHOF NUMBER
Liquid tin ⁸	1.88	0.054	8.0×10^{-2}	6.953	1.02×10^{-4}	0.013	3.6×10^6
" lead ⁸	2.39	0.038	3.9×10^{-2}	10.62	1.15×10^{-4}	0.024	5.8×10^6
" steel ⁸	6.5	0.12	7.0×10^{-2}	6.95	2.0×10^{-4}	0.11	6.0×10^5
" Al	4.5	0.259	2.0×10^{-1}	2.37	-	0.058	-
Water	1.38	1.0	1.4×10^{-3}	1.00	1.2×10^{-4}	10.0	1.3×10^6
Air(50 ⁰ C)	0.019	0.25	2.11×10^{-4}	0.0011	-	0.225	-
NH ₃ Cl ¹⁵	1.30	0.776	1.12×10^{-3}	1.013	1.86×10^{-5}	9.0	2.8×10^4
Oil #1 ²¹	2.5×10^4	0.239	2.36×10^{-4}	1.54	1.98×10^{-4}	2.5×10^5	1.9×10^{-3}
Oil #2 ²¹	1.9×10^3	0.45	4.92×10^{-4}	1.06	7.6×10^{-4}	1.7×10^4	6.1×10^{-1}

where β = Coefficient of thermal expansion

g = Acceleration due to gravity

L = Characteristic length of the system

ΔT = Temperature difference

ν = Kinematic viscosity

The Prandtl number, Pr is the ratio of the momentum to the thermal diffusivity and is defined as:

$$Pr = \frac{\mu C_p}{k} \quad (1.1.2)$$

where μ = viscosity

C_p = Specific heat

k = Thermal conductivity

Table I shows the difference in the Prandtl number between the transparent and metallic materials. Also given in Table I is the Grashof number which has been calculated for a one degree temperature difference and an arbitrary characteristic length.

The Grashof number and the Prandtl number are very important to the heat transfer characteristics of the system. The temperature distribution is related to the Rayleigh number which is the product of these numbers. In natural convection the Nusselt number is usually a function of the Grashof number and the Prandtl number. The Nusselt

number, Nu is a dimensionless parameter which is defined as:

$$\text{Nu} = \frac{h L}{k} \quad (1.1.3)$$

where h is the heat transfer coefficient.

1.1.2 Forced Convection

Forced convection refers to fluid motion which is caused by external forces rather than by buoyancy forces. Many examples of forced convection can be found in metallurgical systems. Figure 1.2 shows the range of flow patterns that can be produced by electromagnetic stirrers used in the continuous casting of steel. The exact extent and velocity of the fluid flow is not clear at present.

In continuous casting the input stream of molten metal represents a considerable source of momentum to the liquid pool. The flow pattern produced and the extent of its effect is determined by the manner in which the stream enters the liquid pool, as shown in Figure 1.3. Below the mould as the momentum from the input stream is dissipated, it is unclear to what degree the flow is caused by the input stream or by natural convection. The flow region represents a situation where there is combined forced and free convection.

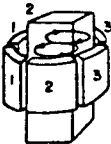
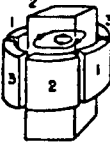
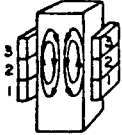
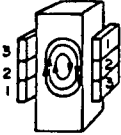
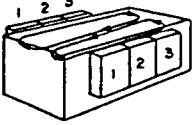
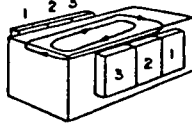
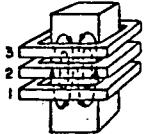
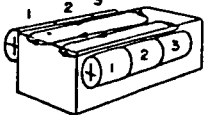
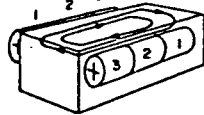
Motor type	Direction (application)	Stirring motion (3 phase: 1 → 2 → 3)	
		Symmetrical	Opposed
Rotary	Circular (billet-bloom)		
Linear	Vertical (bloom-slab)		
Linear	Horizontal (slab)		
Tubular (internal)	Vertical (billet-bloom)		
Tubular (external)	Horizontal (slab)		

FIGURE 1.2 Flow patterns induced by electromagnetic stirring.¹⁶

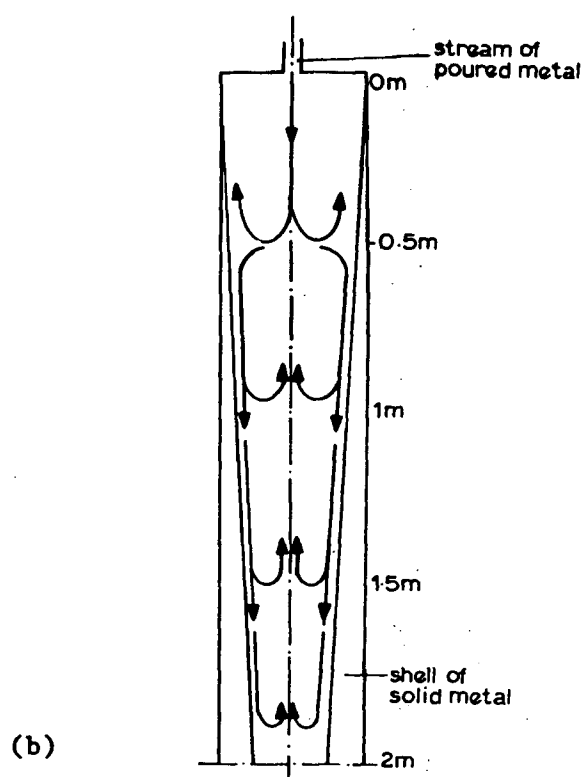
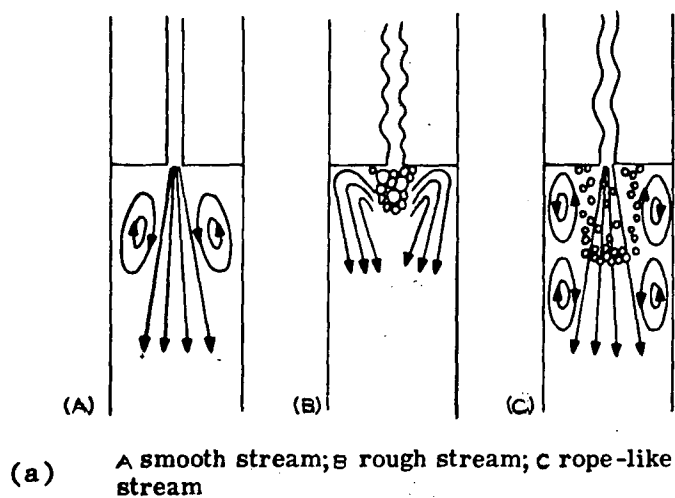


FIGURE 1.3 Effect of input stream on fluid flow in liquid pool
 (a) Flow patterns induced by different types of input streams.²⁰ (b) Example of how input stream induces flow below the mould.²⁰

1.2 CONVECTION IN INDUSTRIAL PROCESSES

The interest in convective flow is best understood by looking at some of the applications where such flow is present. The behaviour of convecting liquid metal is of particular interest in the solidification of castings. The convecting fluid is a major determinant of the final cast structure due to its effect on heat and mass transfer. Figure 1.4 shows the pattern of fluid flow believed to be present at the solid-liquid interface. Natural convection produces counter current flow in the bottom end of large steel ingots which is thought to be responsible for the segregation pattern observed in these castings (see Figure 1.5).

In continuous casting, the flow in the liquid pool is more complex than that in ingots. Work with radioactive tracers² has shown that mixing is most pronounced in and near the mould but in regions below the mould the behaviour of the fluid is not clear. In mathematical models of the solidification profile in continuous casting, the liquid pool is assumed to be completely mixed everywhere. To account for the enhancement in the heat transfer due to convection in the liquid, the liquid is assumed to act as a conducting solid with an effective thermal conductivity, k_{eff} . The value of k_{eff} has been taken in the literature^{3, 4, 5} to be seven to ten times the stagnant thermal conductivity.

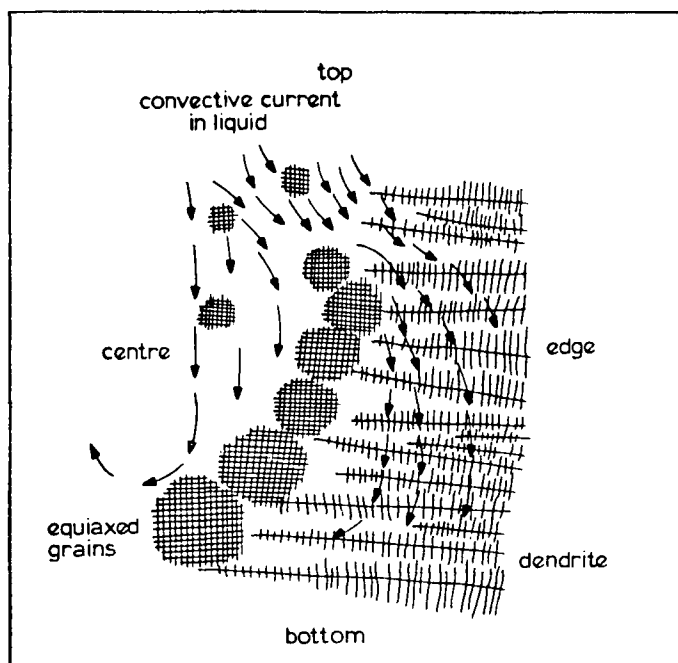


FIGURE 1.4 Fluid flow at solid-liquid interface.¹⁹

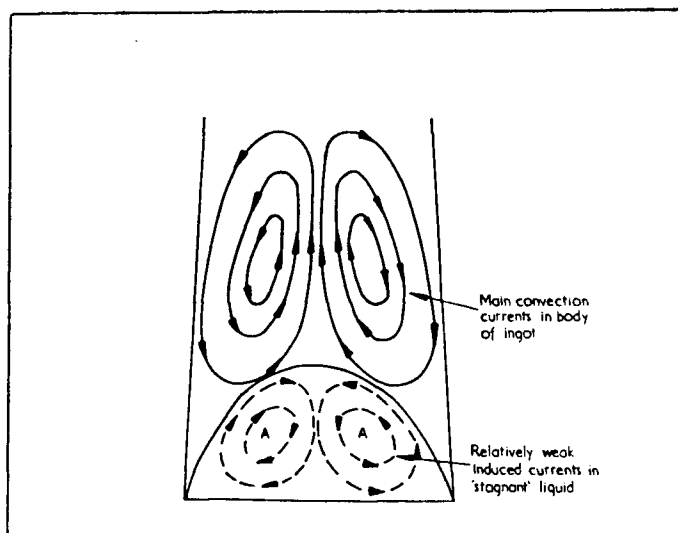


FIGURE 1.5 Convection currents in a solidifying ingot.²⁰

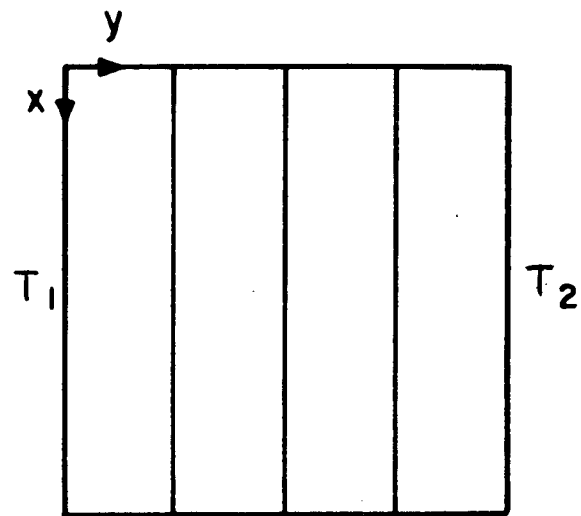
Convection is also of concern in crystal growth where the uniformity of the crystal composition is directly related to product quality. Experiments⁶ have shown that fluid flow due to convection is faster than the growth of the advancing interface therefore it cannot be ignored.

1.3 EXAMINATION OF PREVIOUS INVESTIGATIONS

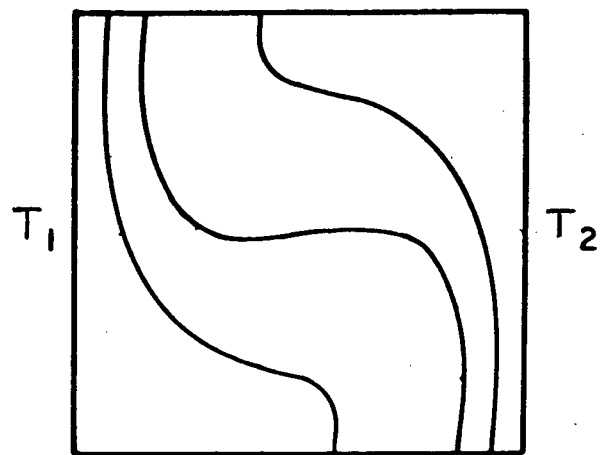
A good review of recent work on natural convection can be found in reference 7. Before discussing previous investigations some of the theory concerning natural convection will be introduced. Theoretical analysis of natural convection is based on the solution of the energy equation and the Navier-Stokes equations. The energy equation for a two-dimensional system is as follows:

$$-k\left(\frac{\partial^2 T}{\partial x^2} + \frac{\partial^2 T}{\partial y^2}\right) + \rho C_p \left(u \frac{\partial T}{\partial x} + v \frac{\partial T}{\partial y}\right) = \rho C_p \frac{\partial T}{\partial t} \quad (1.3.1)$$

where u and v are the x - and y -components of velocity, respectively. The first term in the equation represents the heat from conductive input. The second term is the convective transport contribution. Assuming no heat generation these two quantities are equal to the heat accumulation which is the term on the right-hand side of the equation. The result of the convective terms in this equation is that the isotherms for convective heat transfer are not straight as for heat transfer by conduction. Instead they are bent as shown in Figure 1.6.



(a)



(b)

FIGURE 1.6 Temperature isotherms for (a) purely conductive heat flow and (b) convective heat flow ($T_2 > T_1$).⁸

Since the x- and y-components of velocity appear in the energy equation the velocity field must be known to solve for the temperature field. For forced convection the velocity field can be solved independent of the thermal field. However for natural convection, the temperature appears in the equation for momentum transport in the x-direction (note - the x-direction is taken to be vertical for this system of reference):

$$\frac{\partial u}{\partial t} + u \frac{\partial u}{\partial x} + v \frac{\partial u}{\partial y} = -g\beta(T-T_0) - \frac{1}{\rho} \frac{\partial P}{\partial x} + \nu \left(\frac{\partial^2 u}{\partial x^2} + \frac{\partial^2 u}{\partial y^2} \right) \quad (1.3.2)$$

This coupling of the thermal and velocity fields makes theoretical analysis difficult.

Analytical solutions for these equations have been developed by Batchelor^{9,10} for steady-state natural convection in a rectangular cavity. The velocity profile predicted by the solution of Batchelor is shown in Figure 1.7(a). More recently, numerical solutions have been developed by Wilkes¹¹, Vahl Davis¹² and others^{8,13,14,15}. Results reported by Stewart are shown in Figure 1.7(b) for a range of Grashof numbers with a fixed Prandtl number. According to the numerical results of Stewart, the maximum in the velocity profile shifts toward the boundary with increasing Rayleigh number whereas the profile remains constant according to the solution of Batchelor. Since the analytical model of Batchelor breaks down at large Rayleigh numbers numerical

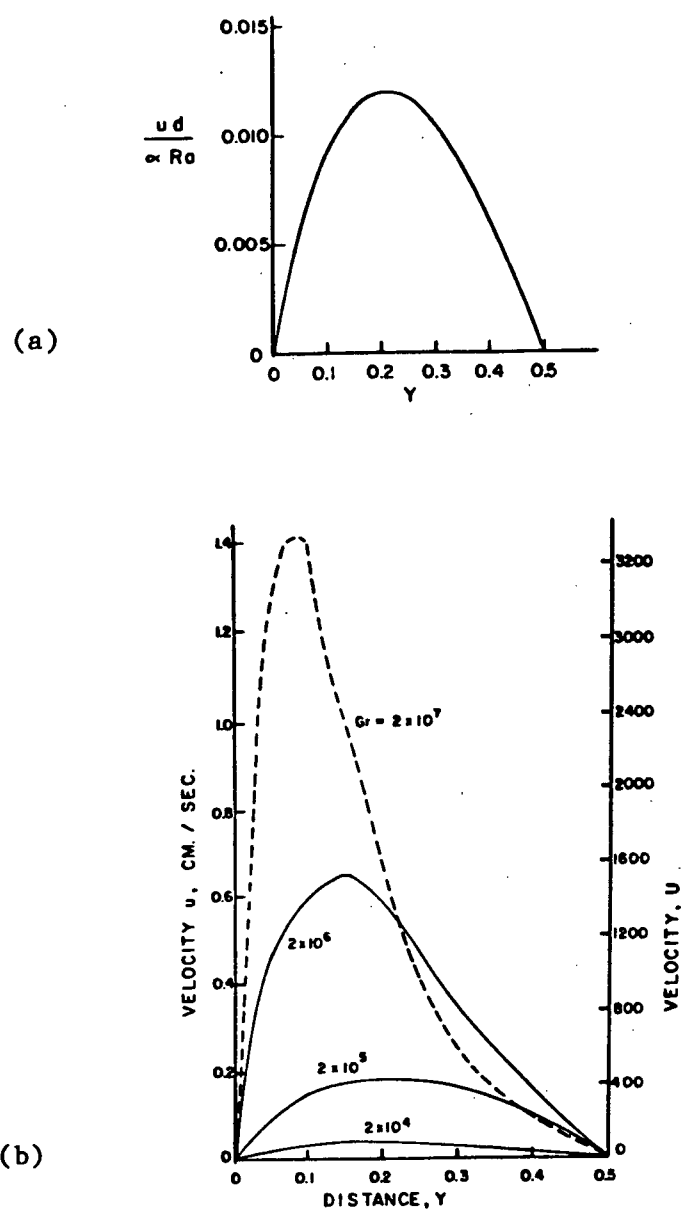


FIGURE 1.7 Vertical (x) velocity plotted versus horizontal position across mid-plane of cavity ($x=0.5$) according to (a) the analytical model of Batchelor and (b) the numerical model of Stewart which shows velocity profiles for $Pr=0.0127$ and various Grashof numbers.

models are more useful for the modelling of metal systems because the Rayleigh number for many liquid metal systems is greater than 10^4 .

In addition to the numerical model, Stewart conducted one of the few studies which used liquid metal for the experiments. This work established a correlation between the time per cycle and the temperature difference across a thin square cavity, as shown in Figure 1.8. The relationship was valid for the type of two-dimensional flow shown in Figure 1.9(a). For large temperature differences across the cell, the flow pattern showed a vortex type motion (see Figure 1.9(b)) exhibiting three-dimensional rather than two-dimensional characteristics. Similar three-dimensional flow patterns were produced if the cell thickness exceeded a certain value. For such flow it is difficult to define the time per cycle and therefore difficult to relate it to the temperature difference across the cell.

1.4 HEAT TRANSFER ANALYSIS

The work by Stewart established that the temperature difference across a rectangular cavity determines the fluid velocity. Using such a cell, the temperature difference can be adjusted to study how the heat transfer across the cell is affected by the amount of fluid flow.

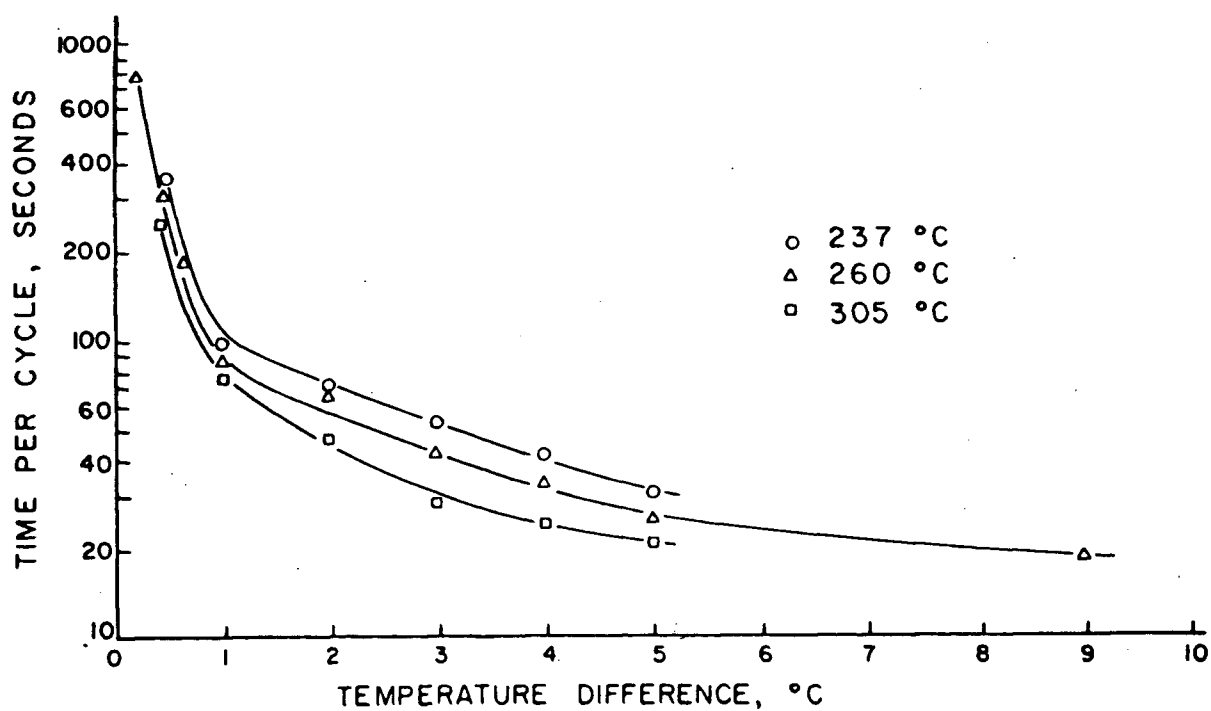
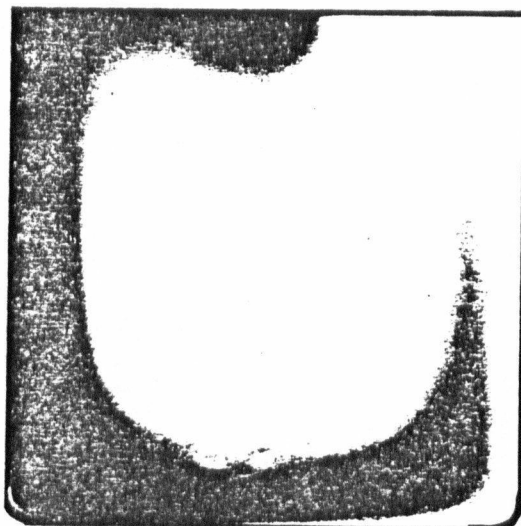
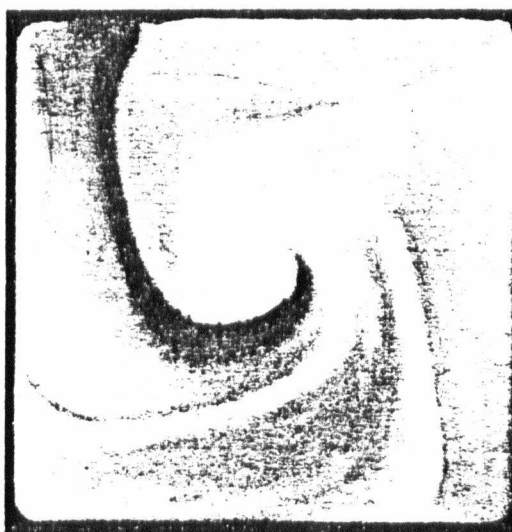


FIGURE 1.8 Correlation observed by Stewart between the time to complete one cycle around cell and the temperature difference across the cell for average melt temperatures of 237 °C, 260 °C and 305 °C .⁸



(a)



(b)

FIGURE 1.9 Radiographs from experiments of Stewart showing (a) two-dimensional laminar flow and (b) three-dimensional vortex flow.⁸

For this investigation, it is necessary to characterize the heat flow across the cell. The idea of an effective thermal conductivity was adopted to describe the heat transfer across the cell. Assuming that no heat is lost from the top, bottom or side walls then

$$\dot{q}_{\text{cold}} = \dot{q}_{\text{melt}} \quad (1.4.1)$$

where \dot{q}_{cold} is the rate of heat flow out of the cold end of the cell and \dot{q}_{melt} is the rate of heat flow across the melt. Assigning an effective thermal conductivity, k_{eff} to the melt then

$$\dot{q}_{\text{melt}} = k_{\text{eff}} \nabla T_{\text{melt}} \quad (1.4.2)$$

Since

$$\dot{q}_{\text{cold}} = k_{\text{cold}} \nabla T_{\text{cold}} \quad (1.4.3)$$

then

$$k_{\text{cold}} \nabla T_{\text{cold}} = k_{\text{eff}} \nabla T_{\text{melt}} \quad (1.4.4)$$

If we assume that the heat flow is primarily one-dimensional then,

$$k_{\text{cold}} \frac{T_{\text{cold}}}{d_{\text{cold}}} = k_{\text{eff}} \frac{T_{\text{melt}}}{d_{\text{melt}}} \quad (1.4.5)$$

where d_{cold} and d_{melt} are the widths of the cold end and the melt, respectively and T_{cold} and T_{melt} are the temperature differences across the cold end and the melt, respectively. Rearranging equation 1.4.5 yields

$$T_{\text{cold}} = \frac{k_{\text{eff}}}{k_{\text{cold}}} \cdot \frac{d_{\text{cold}}}{d_{\text{melt}}} \cdot T_{\text{melt}} \quad (1.4.6a)$$

$$= k_{\text{eff}} \cdot C \cdot T_{\text{melt}} \quad (1.4.6b)$$

where C is a constant. Therefore the slope of the tangent to the curve of T_{cold} versus T_{melt} can be used to determine a value for k_{eff} . Using this technique a value for k_{eff} can be defined for any temperature difference across the melt. Once k_{eff} is correlated to T_{melt} then the relationship between the temperature difference across the cell and the flow velocity could be used to relate k_{eff} to flow velocity.

In the standard heat transfer notation the factor $\frac{k_{\text{eff}}}{d_{\text{melt}}}$ could be thought of as h_{avg} , the average heat transfer coefficient for the melt. The average Nusselt number would then be,

$$\text{Nu}_{\text{avg}} = (h_{\text{avg}}) \frac{d_{\text{melt}}}{k_{\text{Sn}}} = \frac{k_{\text{eff}}}{d_{\text{melt}}} \cdot \frac{d_{\text{melt}}}{k_{\text{Sn}}} = \frac{k_{\text{eff}}}{k_{\text{Sn}}} \quad (1.4.7)$$

where k_{Sn} is the stagnant thermal conductivity of tin.

To summarize, this study looked at heat transfer across liquid metal that was flowing due to natural convection. Using the temperature difference across a thin square cavity to produce varying degrees of natural convection, the temperature differences across the cold end and the melt were measured to calculate a value for the effective thermal conductivity of the melt. This value when compared to the stagnant thermal conductivity indicated the magnitude of the enhancement in heat transfer due to the presence of convection. In addition to the experimental work a numerical model was developed to give insight into the thermal and fluid flow behaviour of the cell.

2.0 EXPERIMENTAL DESIGN

To study the problem of heat transfer with varying degrees of convective flow, the geometry of the flow cell was kept as simple as possible. The cell contained the liquid metal in a thin square enclosure which would produce laminar two-dimensional flow due to natural convection. The temperature of the ends of the cell were varied to change the convective flow velocity in the melt. The flow produced was measured by the flow techniques described in section 2.2. The temperature differences were measured across the melt and the cold end. These values could then be used to determine the heat flow across the melt. The liquid metal used in these experiments was 99.999% pure tin. Table II gives the properties of liquid tin at various temperatures.

2.1 DESIGN OF EXPERIMENTAL CELLS

Three cell systems were developed over the course of this study. Certain design features were common to all three cells. The thickness of the liquid cell was 0.32 cm which should have been small enough to ensure two-dimensional flow, according to Stewart. The heat transfer measurements required that heat flow occurred only through the end pieces therefore the bottom and side walls were made of insulating materials.

TABLE II PROPERTIES OF LIQUID TIN⁸

TEMPERATURE (°C)	VISCOSITY (cp)	SPECIFIC HEAT $\left(\frac{\text{cal}}{\text{gm-}^{\circ}\text{C}}\right)$	THERMAL CONDUCTIVITY $\left(\frac{\text{cal}}{\text{cm-sec-}^{\circ}\text{C}}\right)$	DENSITY $\left(\frac{\text{gm}}{\text{cm}^3}\right)$	COEFFICIENT OF THERMAL EXPANSION $\left(\frac{1}{^{\circ}\text{C}}\right)$
237	2.02	0.0541	0.0798	6.9698	1.0215
260	1.88	0.0543	0.0806	6.9538	1.0239
305	1.68	0.0546	0.0809	6.9217	1.0287

2.1.1 Cell I

To use the correlation between time per cycle and the temperature difference across the melt determined by Stewart, the cell geometry and dimensions which he used were adopted for this design, which is shown in Figure 2.1. The bottom and side walls were made from 0.32 cm glass sheet. The cold end piece was made of stainless steel. The low thermal conductivity of the stainless would produce a significant gradient across the end piece even for low temperature differences across the melt. This ability was considered desirable since the heat transfer behaviour for low temperature differences across the melt was of particular interest because the most rapid change in flow velocity occurs in this range. The cold end was cooled by argon gas jets located in the assembly attached to the end (see Fig 2.1). The hot end of the cell consisted of a copper block with a T-shaped cross-section that had a hole to allow for the heating assembly. The heater consisted of chromel heating wire which was wrapped around a ceramic sheath. Power was supplied by a variac.

Before assembling the cell the inside surfaces were coated with colloidal graphite to prevent liquid metal from attacking the cell walls and to seal any gaps between components. The walls of the cell were held together by bolts through the bottom piece and by the specially designed end pieces, as shown in Figure 2.1. The top of the cell was open to allow for the thermocouple wires coming out of the melt. The

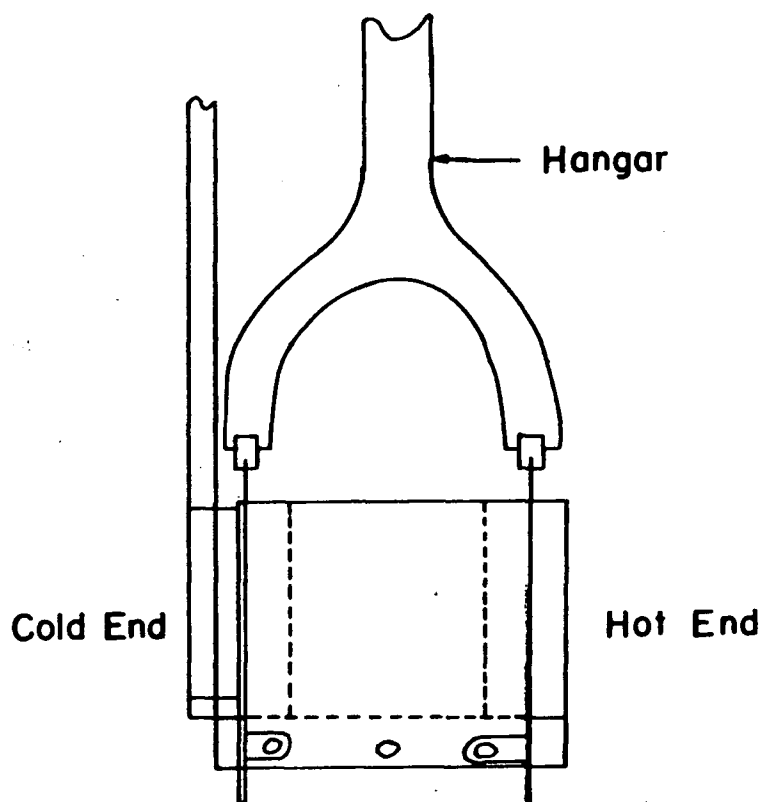
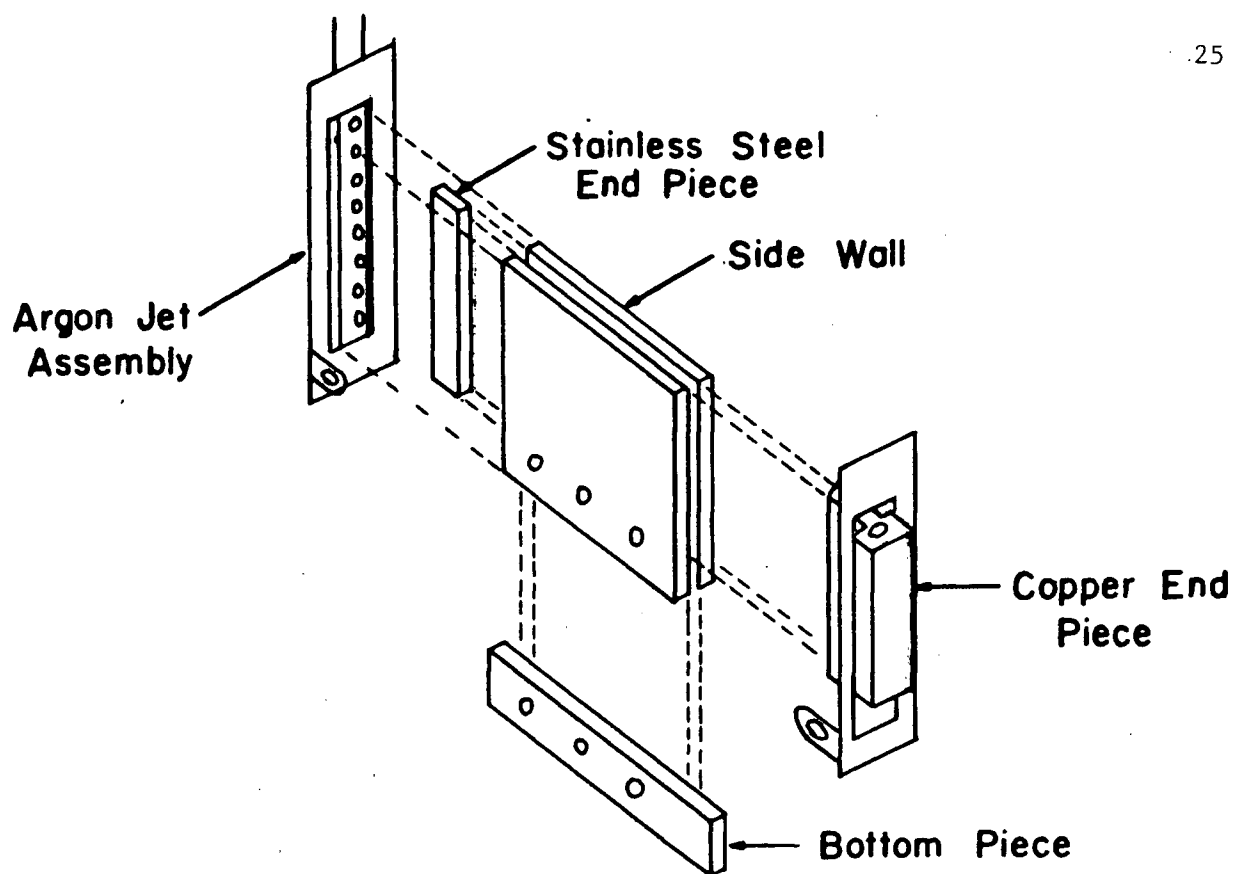


FIGURE 2.1 Design of experimental cell I

mould was suspended in the furnace by a hangar attached to the ends of the cell. The furnace temperature was controlled by a Honeywell temperature controller (model 5500101).

2.1.2 Cell II

Since this cell was to be used for quench experiments the walls were made of 0.48 cm stainless steel instead of glass which would crack due to thermal shock if quenched. Although the overall cell dimensions were the same as for cell I, new end pieces were designed due to problems with the end pieces in cell I. The cold end was made of copper instead of stainless steel. This copper piece had a U-shaped copper tube soldered to the back face. The tube was used to provide the Ar gas cooling instead of the jets used in cell I. Two thermocouples were soldered between the tube and the end piece. A thermocouple probe was used to measure temperatures near the hot and cold ends of the melt once the cell was operating.

The bottom piece of the cell was made of teflon to minimize heat flow along the bottom. The cell was bolted through the bottom and clamps were used along the side edges.

2.1.3. CELL III

Results from cells I and II lead to the design of the larger cell shown in Figure 2.2. A different furnace was necessary to accommodate the new cell. This cell design eliminated the need for bolts through the bottom of the cell. Instead, clamps were used along the bottom and sides of the cell, as shown in the figure. There was a special assembly at the cold end which incorporated the clamps and argon jets and provided a shield around the end to prevent argon from flowing into the furnace.

To provide more reliable attachment of the thermocouples to the outside face of the cold end, the cold end piece was designed with three threaded holes which allowed the thermocouples to be held in place by screws. However the inside thermocouples were still spotwelded in place since the use of screws would distort the interface between the melt and the end piece. Due to the number of thermocouples, a thermocouple switch was used to monitor the output of the thermocouples.

It was found that composite cell walls were best for quenching. The cell wall consisted of an inner wall, made from 0.08 cm aluminum sheet and an outer wall, made from 0.016 cm stainless steel sheet, which were separated by 0.016 cm teflon spacers at the edges. The resulting air gap between the walls provided an insulating layer in the wall. To

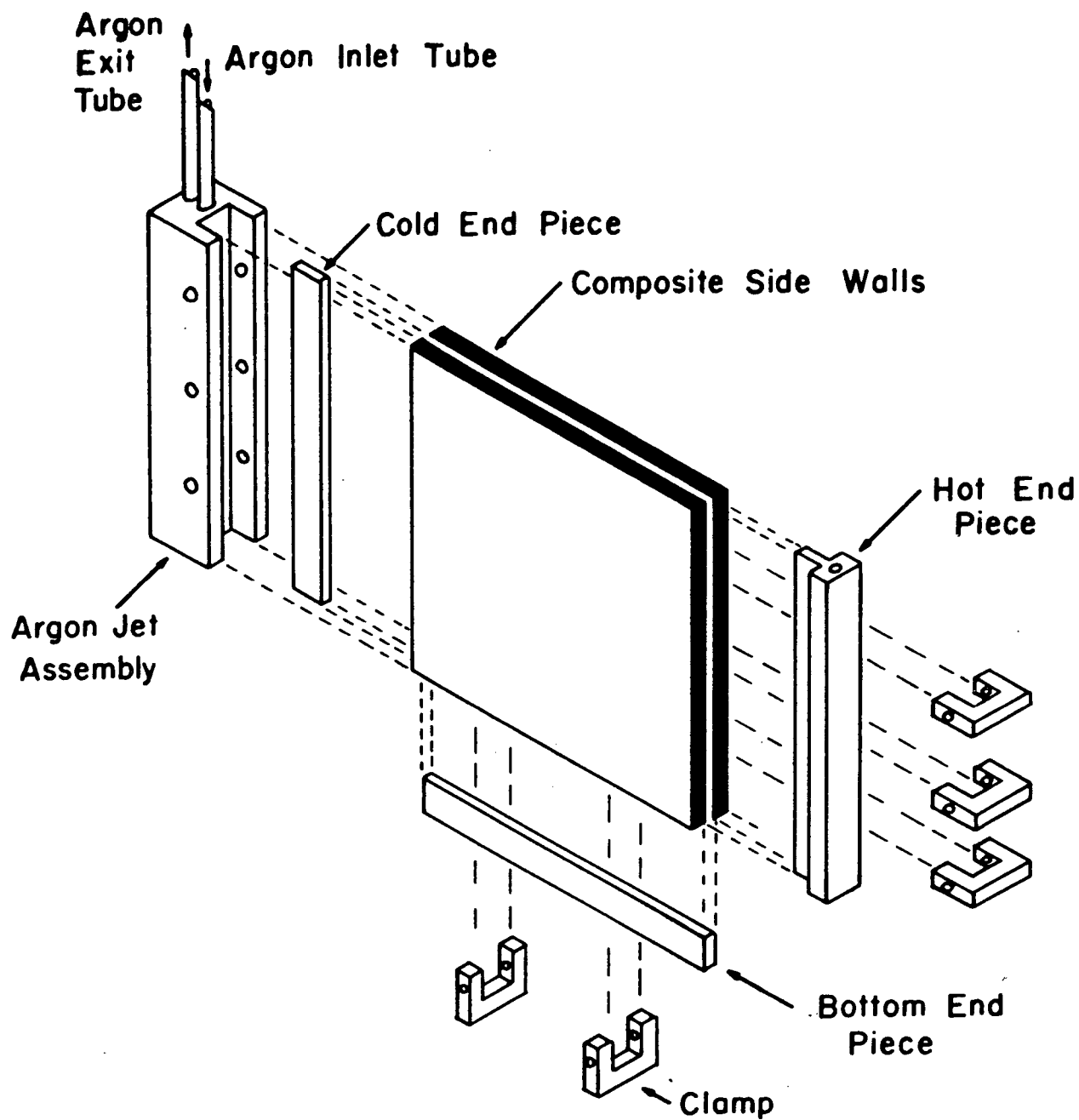


FIGURE 2.2 Design of experimental cell III.

quench the melt, water was forced into this air gap from a thin-walled stainless steel tube (o.d. ≈ 1.2 cm) with the end flattened to allow insertion into the gap. Since only the aluminum sheet separated the cooling water from the melt, the molten metal could be quenched in less than two seconds using this technique.

2.2 FLUID FLOW MEASUREMENT

Two methods were used to measure the flow velocities in the melt. The first method consisted of monitoring the activity of a small piece of radioactive copper added to the melt. The second procedure consisted of adding radioactive tin (Sn^{113}) to the tin melt and then quenching the melt to establish the path of the radioactive tin in the melt.

The general procedure for the copper particle experiment is as follows:

i) The temperature of the melt was monitored by a thermocouple probe. When the cell reached thermal equilibrium, a piece of radioactive copper (Cu^{64}), less than 2 mm in diameter was inserted into the melt.

ii) Lead bricks were arranged so that the activity of the copper

particle could be monitored from the top or side of the cell by a fast-rate scintillation counter. The position of the copper particle could be determined by estimating the absorption due to the tin. The expected periodicity in the count rate would be directly related to the period of the fluid flow in the cavity.

The general procedure which was followed for the experiments using the radioactive tin (Sn^{113}) as tracer was:

i) Before inserting the Sn^{113} into the melt, the temperature at end of the melt was measured using a thermocouple probe. Temperatures were taken at approximately the middle of the inside face of each end.

ii) The radioactive tin (Sn^{113}) was added near the cold end of the cell and after a given time the cell was quenched.

iii) After quenching, the solid block of tin was removed from the cell and placed on a sheet of X-ray film. Another sheet of film was placed on top and a glass sheet put on top to ensure good contact between the film and the sample. The film was exposed for two to three days then developed. The resulting dark areas on the film indicated the location of the Sn^{113} and thus showed the extent of fluid flow in the melt between the moment the radioactive tin was added and the moment when the sample was quenched.

2.3 TEMPERATURE MEASUREMENT

Chrome-alumel thermocouples were used for the temperature measurements in this study. For cell I, 0.1 mm uncoated thermocouple wire inside ceramic sheaths was used. For cells II and III, 0.025 cm wire was used since the finer wire was easier to embrittle during the spot-welding and would often break near the weld. In addition, coated wire was used instead of the ceramic sheaths since the larger ceramic sheaths might obstruct the liquid metal from complete contact with the end piece.

The locations of the thermocouples in each cell are shown in Figure 2.3. The use of spot-welded thermocouples instead of a thermocouple probe was preferred for the heat transfer measurements since the location of the probe could not be defined precisely and therefore it would be difficult to reproduce its location for each measurement. However, for the quench tests, a thermocouple probe was used because it would have been necessary to replace spot-welded thermocouples after each sample was removed from the cell.

The cold junctions of the thermocouples in cells I and II were maintained in an ice-water bath. The junctions in cell III were connected directly to the thermocouple switch. A thermometer attached to the thermocouple switch was used to determine the temperature of the

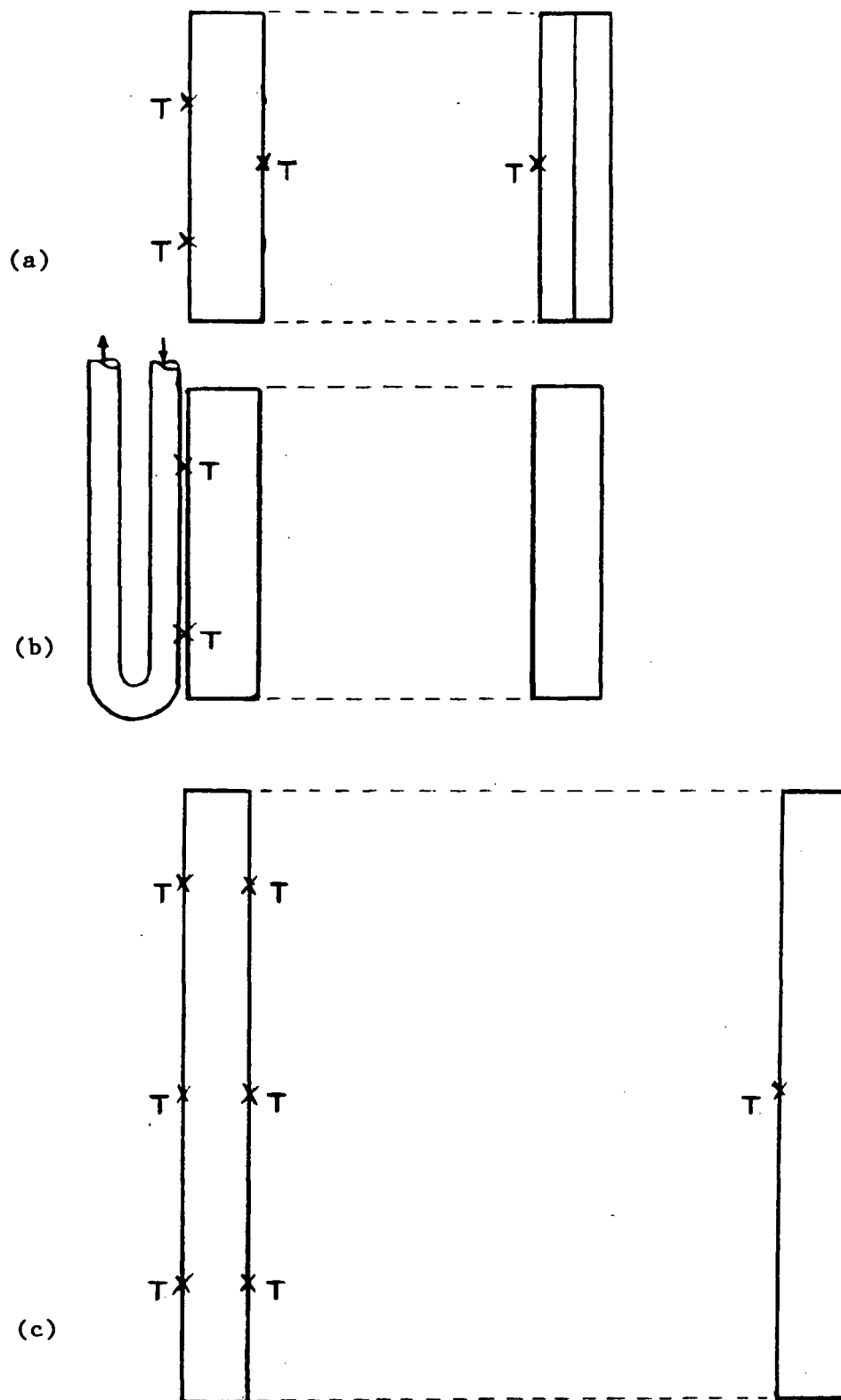


FIGURE 2.3 Location of thermocouples in experimental cells a) cell I, b) cell II and c) cell III (thermocouple location is marked by T).

cold junction.

The output from the thermocouples was recorded on a Honeywell chart recorder (model no. 194). The range of the chart recorder was adjusted to be either one or two millivolts full-scale deflection, depending on the magnitude of the temperature differences between the thermocouples.

3.0 EXPERIMENTAL RESULTS

3.1 RESULTS FROM FIRST EXPERIMENTAL CELL

Several runs were made using the first cell with the top of the cell open and with it partially covered. Sufficiently large temperature differences were produced without the use of the heater. Figure 3.1 shows the results plotted as ΔT_{ss} , the temperature difference across the stainless steel end versus ΔT_{melt} , the temperature difference across the melt. The experiments with the top of the cell covered and uncovered both showed linear relationships between the temperature difference across the cold end and that across the melt. The constant slope in Figure 3.1 indicates that k_{eff} , the effective thermal conductivity, was constant.

3.1.1 Calculation of the Effective Thermal Conductivity

The value of k_{eff} can be calculated from m , the slope of the graph of ΔT_{cold} versus ΔT_{melt} using equation 1.4.6(a). According to equation 1.4.6(a),

$$m = \frac{k_{eff}}{k_{cold}} \cdot \frac{d_{cold}}{d_{melt}} \quad (3.1.1)$$

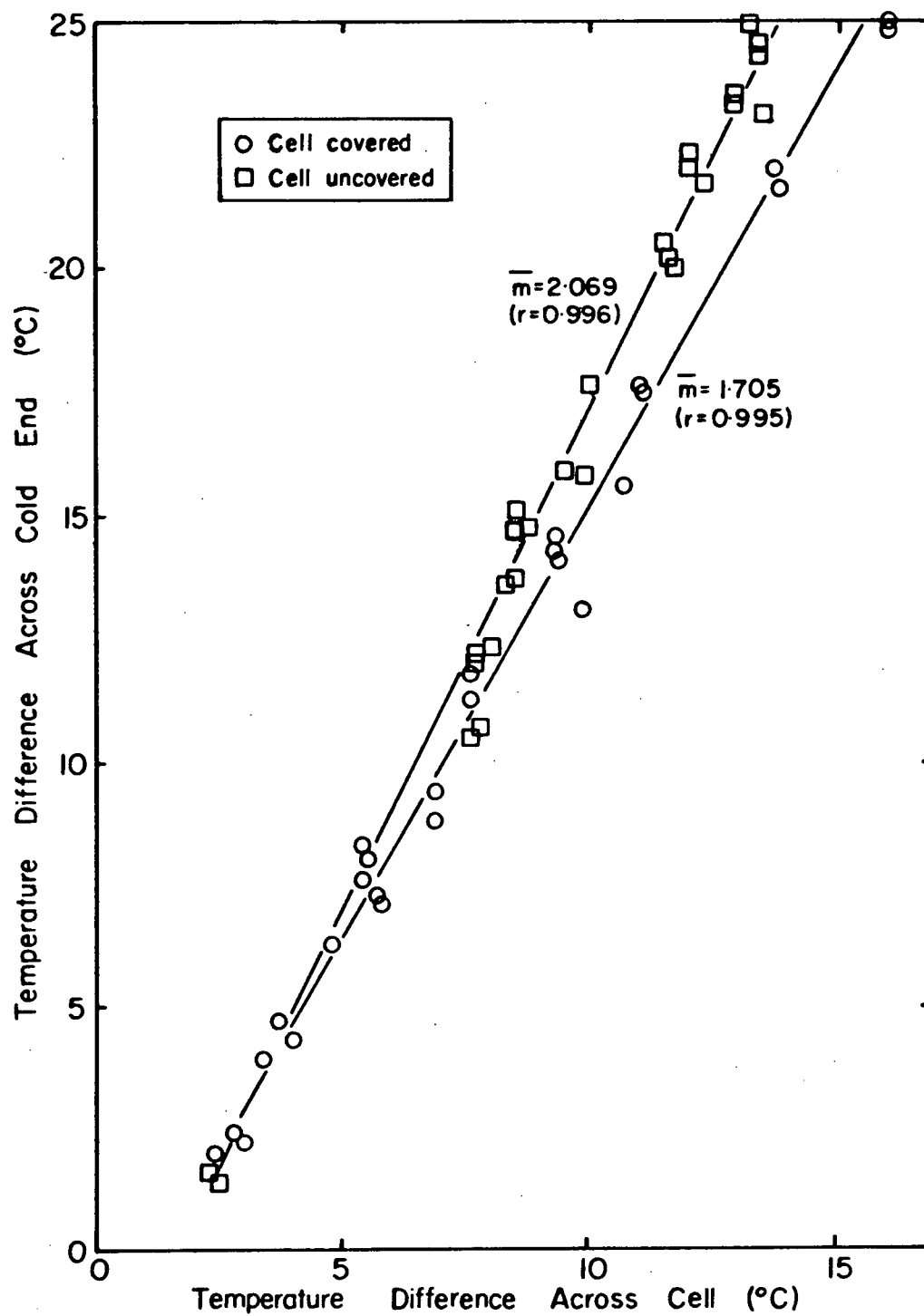


FIGURE 3.1 Graph showing results from cell I with top of cell covered and uncovered. Slopes were calculated using linear regression of data points. The correlation coefficient is given in brackets.

Therefore,

$$k_{\text{eff}} = m \cdot \left(\frac{k_{\text{cold}} \cdot d_{\text{melt}}}{d_{\text{cold}}} \right) \quad (3.1.2)$$

For cell I:

$$k_{\text{cold}} = \text{Thermal conductivity of stainless steel} = 0.044 \text{ cal/cm-sec-}^{\circ}\text{C}$$

$$d_{\text{melt}} = \text{Distance across melt} = 5.0 \text{ cm} \quad (3.1.3)$$

$$d_{\text{cold}} = \text{Distance across cold end} = 1.25 \text{ cm}$$

From figure 3.1:

$$\bar{m} \text{ (uncovered)} = 2.069 \quad (3.1.4a)$$

$$\bar{m} \text{ (covered)} = 1.705 \quad (3.1.4b)$$

Calculating the values for k_{eff} using equation 3.1.2 yields:

$$\begin{aligned} k_{\text{eff}} \text{ (uncovered)} &= 0.3641 \text{ cal/cm-sec-}^{\circ}\text{C} \\ &\cong 4.5 \times k_{\text{Sn}} \end{aligned}$$

$$\begin{aligned} k_{\text{eff}} \text{ (covered)} &= 0.3003 \text{ cal/cm-sec-}^{\circ}\text{C} \\ &\cong 3.8 \times k_{\text{Sn}} \end{aligned} \quad (3.1.5)$$

$$k_{\text{Sn}} \text{ (stagnant)} = 0.08 \text{ cal/cm-sec-}^{\circ}\text{C}$$

3.1.2 Discussion of Results from Cell I

There are several reasons why k_{eff} would be constant. It may have been constant because it was independent of the degree of convection. This condition would be expected when the enhancement in heat transfer due to convective flow had reached its limit. Looking at the degree of convection produced, the largest temperature differences employed across the melt were big enough to ensure that the maximum flow was achieved, according to Figure 1.8. Therefore it is possible that the heat transfer limit had been reached. Also according to Figure 1.8, the lowest temperature differences that were used would only produce flows that were marginally slower than the maximum flow. Therefore the reason k_{eff} remained constant was probably because the change in convective flow was too small to show an effect.

The magnitude of the effective thermal conductivity is about four times the stagnant thermal conductivity of tin. This factor is lower than the seven to ten times enhancement assumed in the mathematical modelling of continuous casting. It is possible that this number represents the maximum enhancement achievable with natural convection. However there may be another reason why k_{eff} is low.

The heat transfer through the cell is not completely determined by the characteristics of the molten bath. The rate of heat flow

through the cell is affected by the thermal resistances of the boundaries as well as the thermal resistance of the melt. The thermal resistance of the hot end of the cell (Cu) was lower than that for liquid tin, as shown in Table III. The thermal resistance of the cold end of the cell (stainless steel) is less than the thermal resistance of stagnant liquid tin but is greater than that presented by the convecting melt. From this analysis the heat transfer across the cell would appear to be limited by the stainless steel end piece rather than the behaviour of the melt. This reason could also explain why k_{eff} remained constant. To avoid this problem the next two cell designs employed copper for both ends of the cell.

3.2 RESULTS FROM CELL II

The next series of experiments were conducted with the second cell which duplicated the dimensions of the first cell but used different materials for its construction. The first experiments with this cell attempted to measure the degree of convective flow using the copper particle method. This method was preferred since the technique would provide information about the flow at the temperature measurement conditions rather than inferring the flow from a quench. As well, the change in convective flow could be observed when the temperature difference was adjusted, providing a look at the transient and steady state behaviour.

TABLE III COMPARISON OF THERMAL RESISTANCES

MATERIAL	THERMAL CONDUCTIVITY k $\left(\frac{\text{cal}}{\text{gm-sec-}^{\circ}\text{C}}\right)$	LENGTH L (cm)	THERMAL RESISTANCE* $R = \frac{L}{k A}$ $\left(\frac{\text{sec-}^{\circ}\text{C}}{\text{cal}}\right)$
Copper	0.928	1.27	1.37
Stainless steel	0.044	1.27	28.97
Liquid tin, stagnant	0.080	5.08	63.50
Liquid tin, convecting	0.30**	5.08	16.93

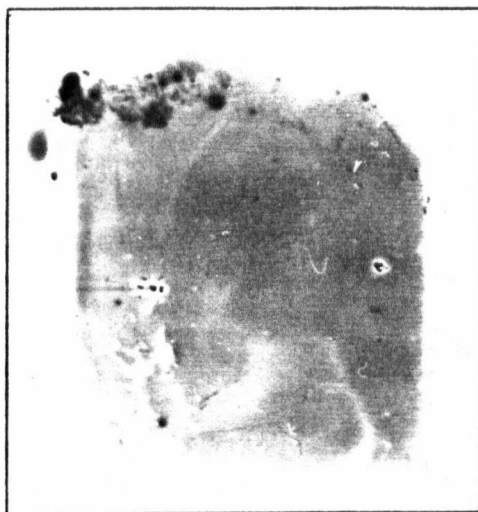
* - For comparison purposes the area, A has been taken = 1 cm³

** - Approximate value from equation 3.1.5

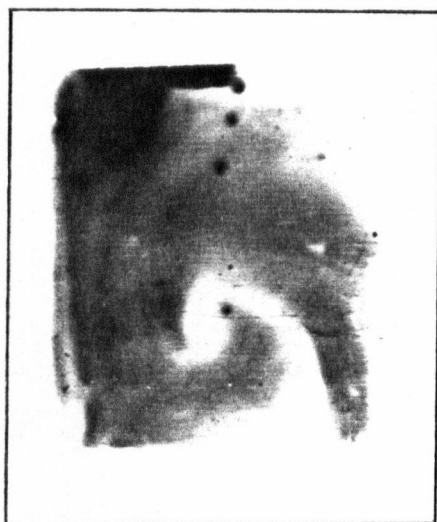
When the counting rates from the copper particle experiments failed to produce the expected periodicity the quench technique was used to look at the flow pattern in the cell. The radiographs from these experiments showed nearly uniform greying across the sample indicating that the tracer was well mixed by the time the quench was finished (see Figure 3.2(a)). Some samples showed evidence of vortex-type flow (see Figure 3.2(b)) which would explain why the copper particle experiments failed to show any periodicity. Other samples appeared to be very turbulent, as shown in Figure 3.2(c), but it is not certain whether the turbulence was present prior to the quench or whether it was caused by the quench. These results imply much higher velocities than those expected from the results of Stewart.

3.3 RESULTS FROM CELL III

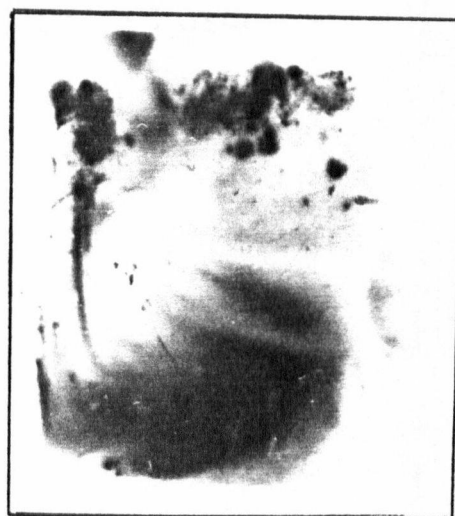
Since the previous cell size did not provide the range of convective flow that was expected it was decided to conduct experiments on a larger cell and to establish the relationship between the convective flow and the temperature difference across the cell by quenching the cell.



(a)



(b)



(c)

FIGURE 3.2 Quenched samples from cell II (a) Tracer is well mixed ($\Delta T = 6^{\circ}\text{C}$, time prior to quench ≈ 30 sec), (b) Sample showing vortex motion ($\Delta T = 8^{\circ}\text{C}$, time prior to quench ≈ 30 sec), (c) Sample exhibiting turbulent flow ($\Delta T = 5^{\circ}\text{C}$, time prior to quench ≈ 25 sec).

3.3.1 Results of Quench Tests

The first concern of the experiments on the new cell was the adequacy of the quench. The stainless steel walls of the previous cell were believed to have had too low thermal conductivity to provide a fast quench and it was suspected that some flow had occurred after the initiation of the quench. To verify this suspicion the first quench tests with cell III were performed using stainless steel walls which were made of two pieces of 0.16 cm stainless steel sheet glued together. The sample was quenched by rapidly filling up the inside can of the furnace with cooling water. The quench was very slow and the cooler liquid from the sides would fall to the bottom and produce the flow pattern shown in Figure 3.3(a). When quenched in the manner used for cell II by aiming jets of water at the walls the quench was much faster but the flow was still distorted during the quench producing the fork-like pattern shown in Figure 3.3(b). Figure 3.4 shows a successful quench obtained using the composite cell wall design described in section 2.1.3.

The radiographs of the quenched samples used to determine the time per cycle are shown in Figure 3.5. The resulting graph of the time per cycle versus the temperature difference across the melt is given in Figure 3.6 and is very similar to that observed by Stewart.

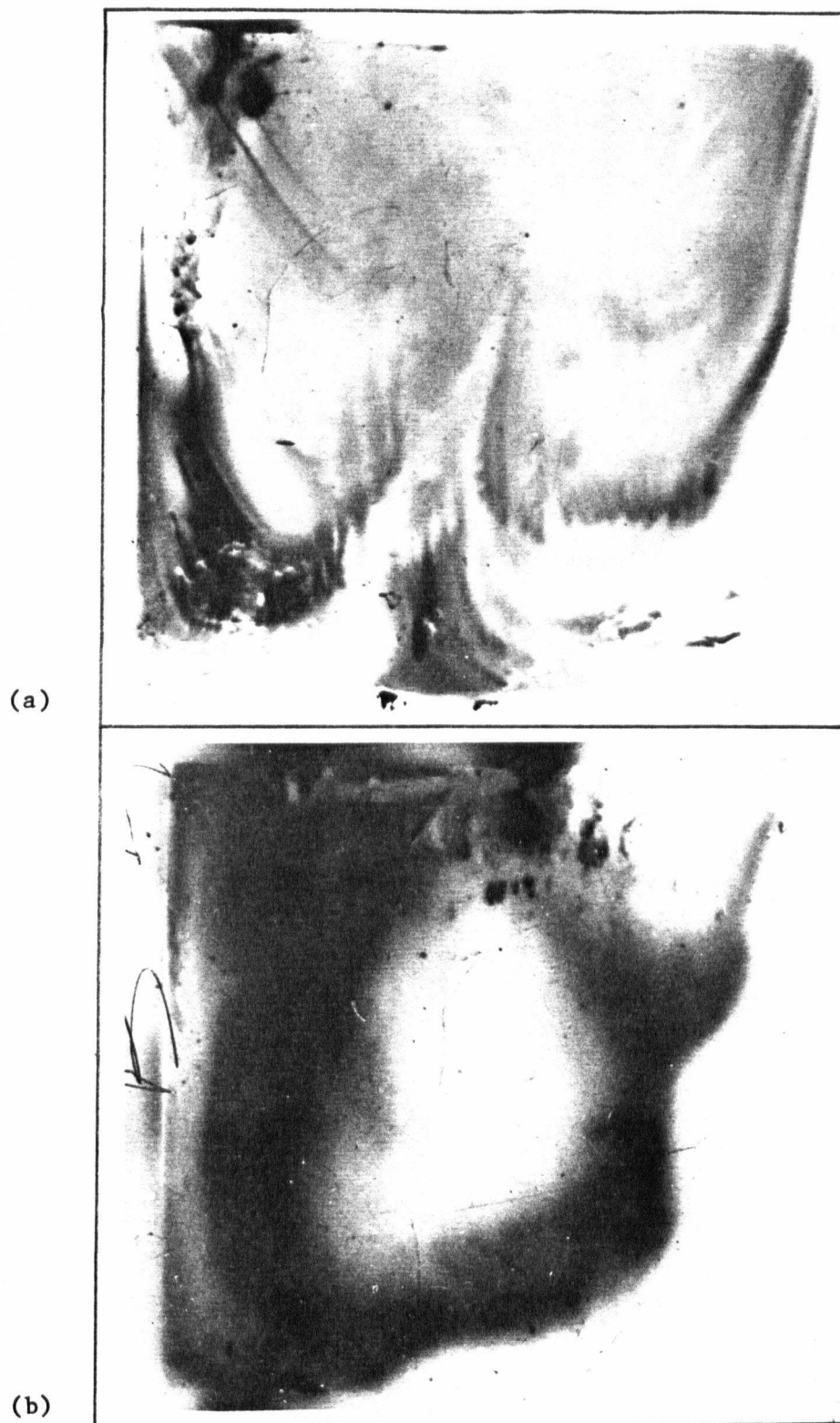


FIGURE 3.3 Examples of inadequate quenches from cell III (a) Sample quenched by rapidly filling inside of furnace with water and (b) Sample quenched using water jets aimed at side walls.

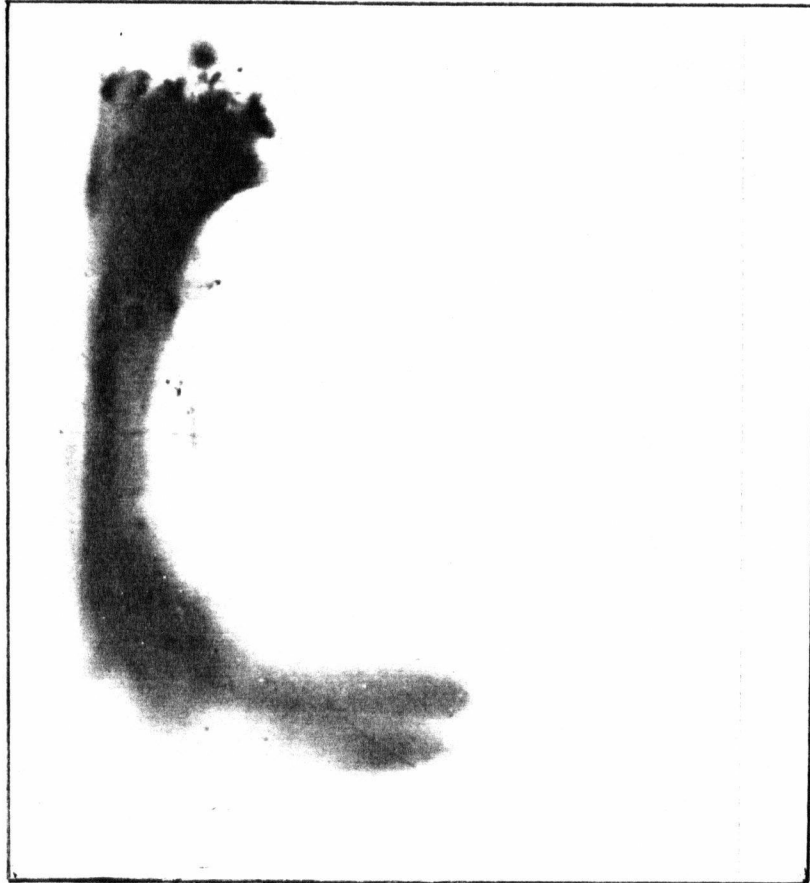
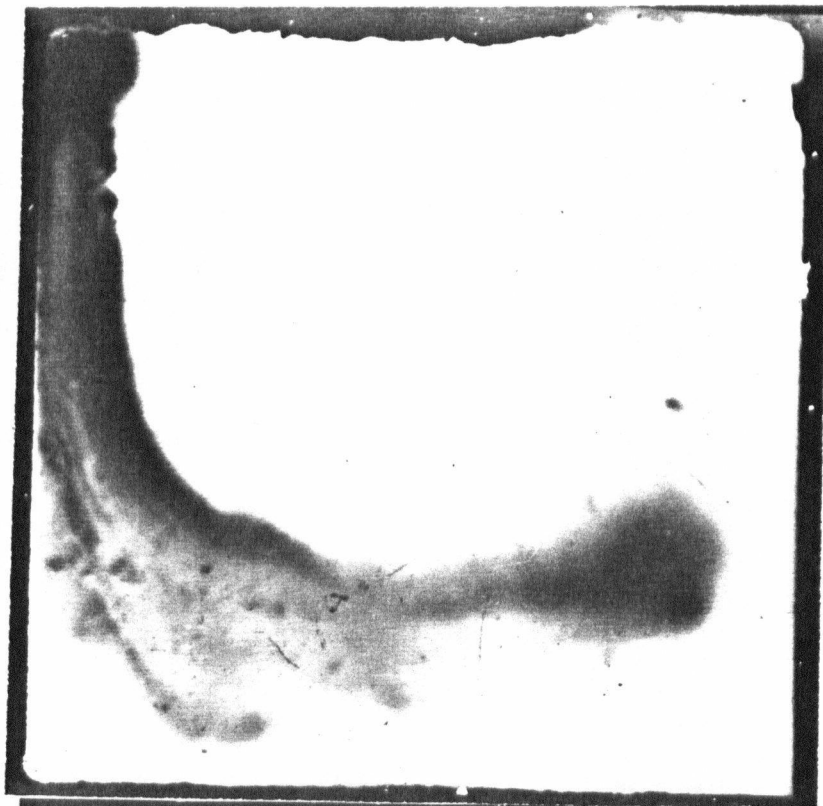


FIGURE 3.4 Successful quench sample achieved using composite cell wall design.

(a)



(b)



FIGURE 3.5 Quenched samples from cell III (a) $\Delta T=7.6$ $^{\circ}\text{C}$, time prior to quench = 20 sec (b) $\Delta T=7.2$ $^{\circ}\text{C}$, time prior to quench = 21 sec.



(c)



(d)

FIGURE 3.5 (Continued) Quenched samples from cell III (c) $\Delta T=1.4$ $^{\circ}\text{C}$ time prior to quench = 22 sec, (d) $\Delta T=4.4$ $^{\circ}\text{C}$, time prior to quench = 11 sec.

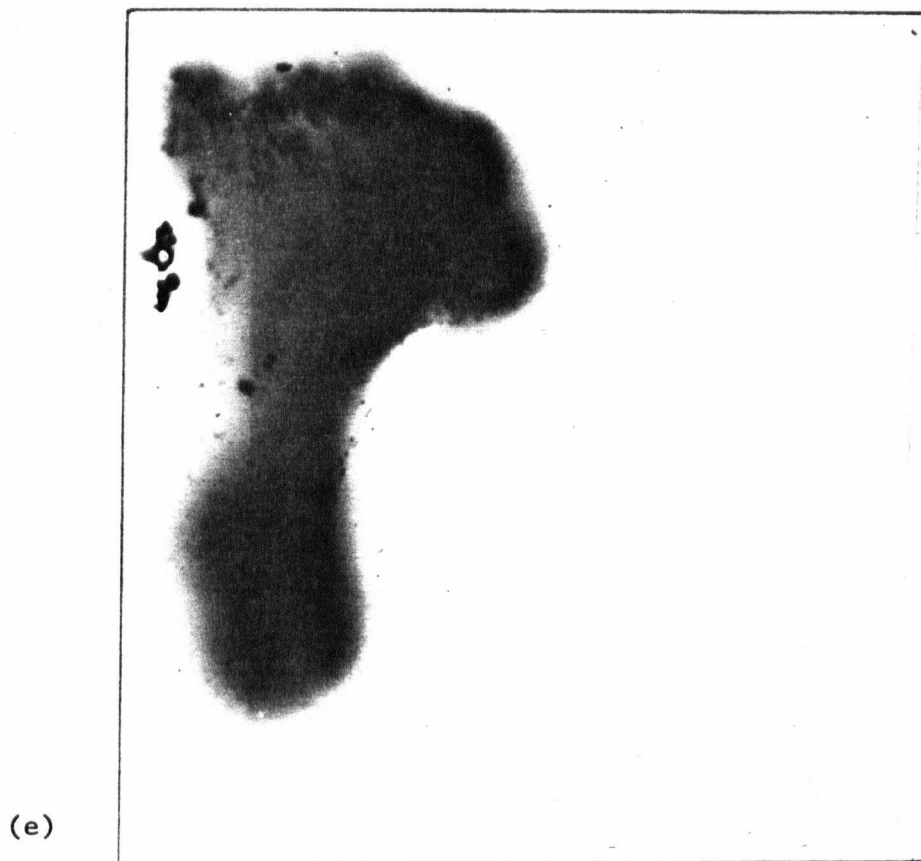


FIGURE 3.5 (Continued) Quenched samples from cell III (e) $\Delta T = 2.4^\circ\text{C}$
time prior to quench = 18 sec.

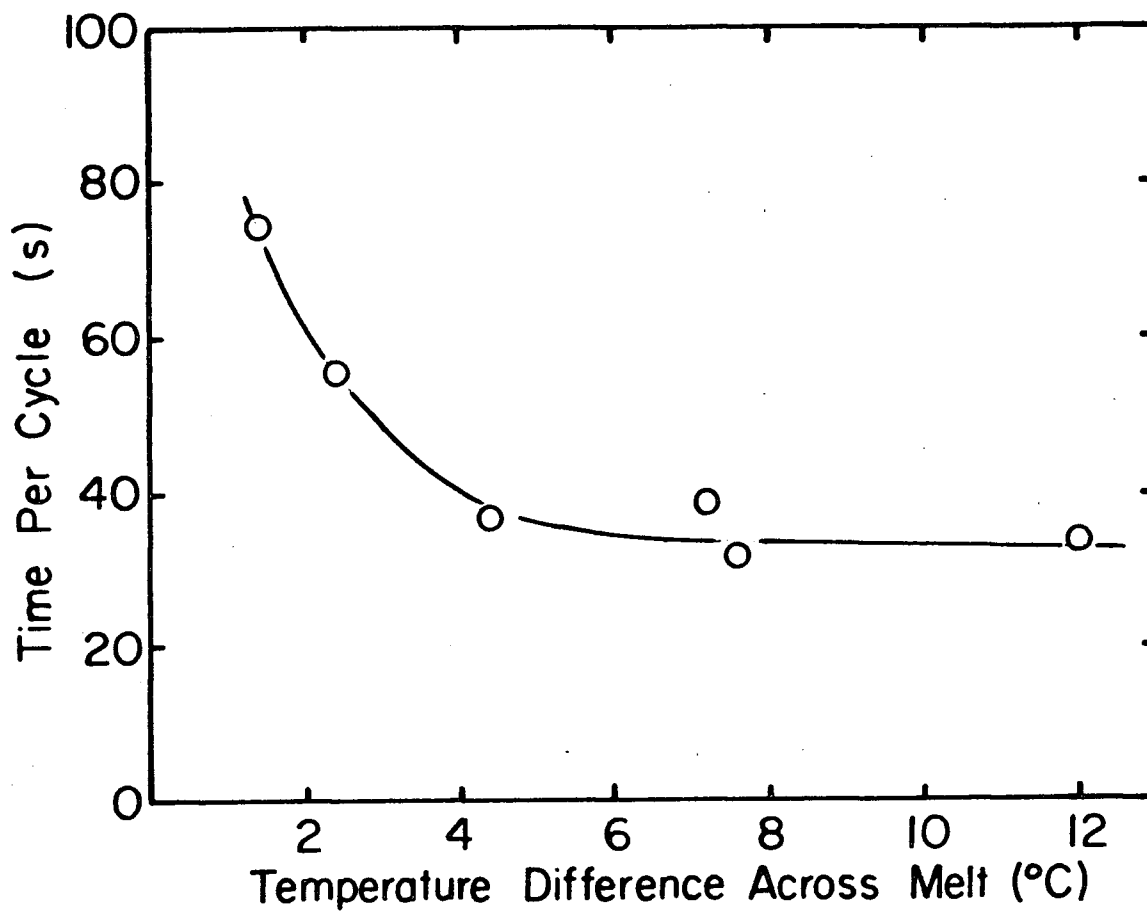
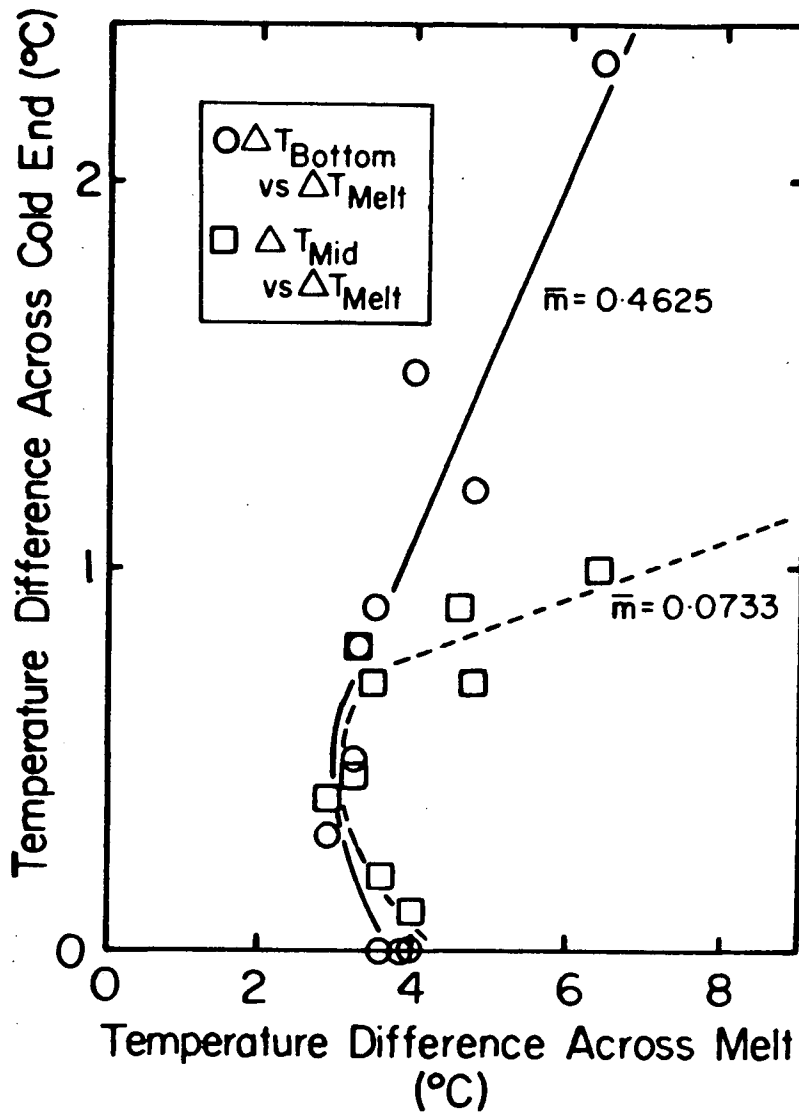


FIGURE 3.6 Relationship between time required per cycle and the temperature difference across the melt (Temperatures in melt were measured using a thermocouple probe).

3.3.2 Temperature Measurements

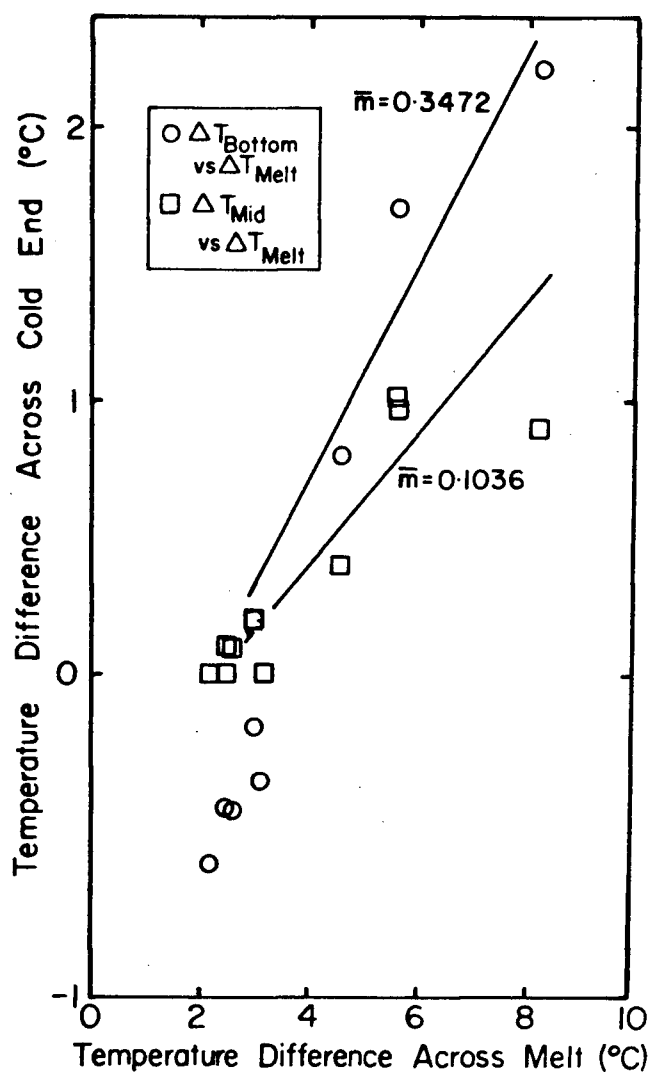
Having established that the flow was laminar and behaved in a predictable manner, detailed temperature measurements were performed. The measured temperatures were accurate to $\pm 0.3^{\circ}\text{C}$. The temperature difference across the melt was measured from the mid-point of the hot face to the mid-point of the cold face. Temperatures were measured at three points along the outside face and at three points along the inside face of the cold end, as shown in Figure 2.3(c). These temperatures were used to calculate the temperature difference across the cold end. Rather than using the average temperature of the outside and inside faces of the cold end to calculate a single temperature difference for the cold end, a temperature difference was calculated for each pair of thermocouples. Temperature differences were calculated for the bottom and middle sections of the cold end but not for the top section due to problems with the thermocouple at the top of the inside face.

Two experimental conditions were employed. For experiment A, both the heater in the hot end and argon gas cooling of the cold end were used to create the temperature difference across the melt. For experiment B, only argon gas cooling was used to produce the temperature difference. Figure 3.7 gives the plot of the temperature difference across the cold end versus the temperature difference across the melt for the two experiments. There are two distinct regimes in the results for experiment A, as shown in Figure 3.7(a). Initially, the



(a)

FIGURE 3.7 Graph of temperature differences across cold end versus temperature difference across melt for (a) experiment A which used a heater and argon cooling to produce the temperature difference across melt. Slopes indicated on graph were calculated using linear regression of data points.



(b)

FIGURE 3.7 (Continued) Graph of temperature differences across cold end versus temperature difference across melt for b) experiment B which only used argon cooling to produce the temperature difference across melt. Slopes indicated on graph were calculated using linear regression of data points.

temperature difference across the melt does not appear to be related to the temperature difference across the cold end then there is an abrupt transistion into the second regime where there is a linear relationship between the two temperature differences. The results for experiment B showed a gradual transistion into the linear region as indicated in Figure 3.7(b).

It was found that the linear behaviour in Figure 3.7 was associated with large argon flow rates. To investigate the dependence on flow rate, the temperature differences in the cell were plotted as a function of the argon flow rate. The argon flow rate is expressed as a dimensionless number corresponding to the scale reading on the flowmeter. Appendix II contains a chart which can be used to convert a given flow rate to millilitres per minute. Figure 3.8 shows these plots for experiment A. At low flow rates neither the temperature difference across the cold end nor that across the melt increased uniformly with increasing argon flow rate. At one point, the temperature difference across the melt decreased with increasing flow rate, as shown in Figure 3.8(b). This behaviour appears to be associated with the use of the heater since it did not occur in Figure 3.9 which shows the plots for experiment B where only argon cooling was used to produce the temperature difference across the melt.

Figure 3.10 shows the relationship between the actual temperatures and the argon flow rate for the two experiments. Although

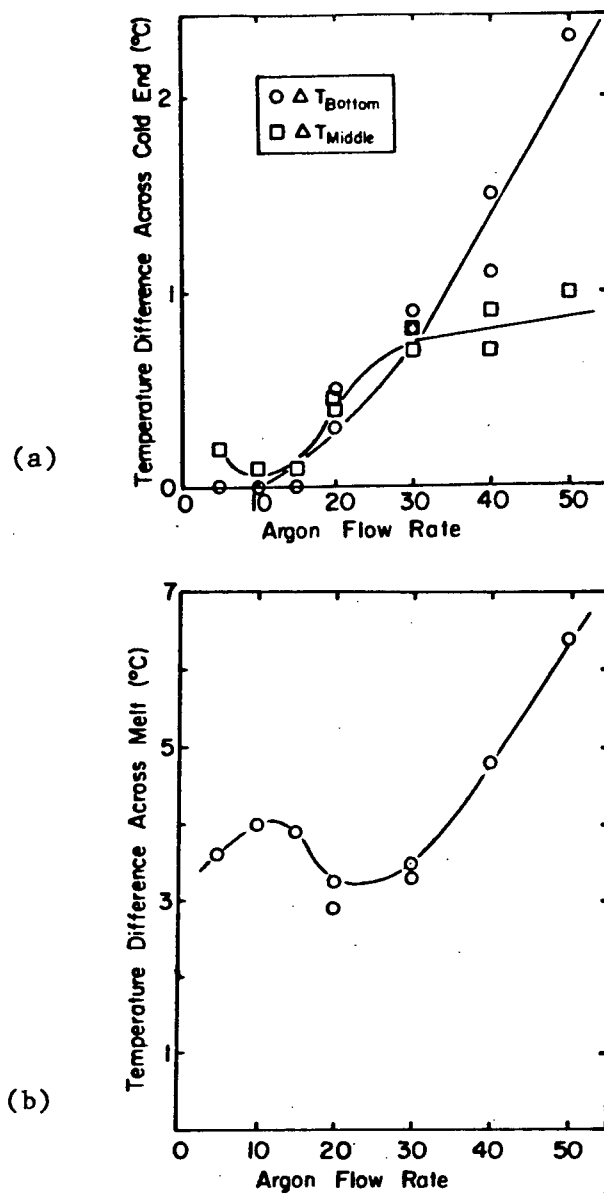


FIGURE 3.8 Graphs showing behaviour of temperature differences across (a) the cold end and (b) the melt versus argon flow rate for experiment A.

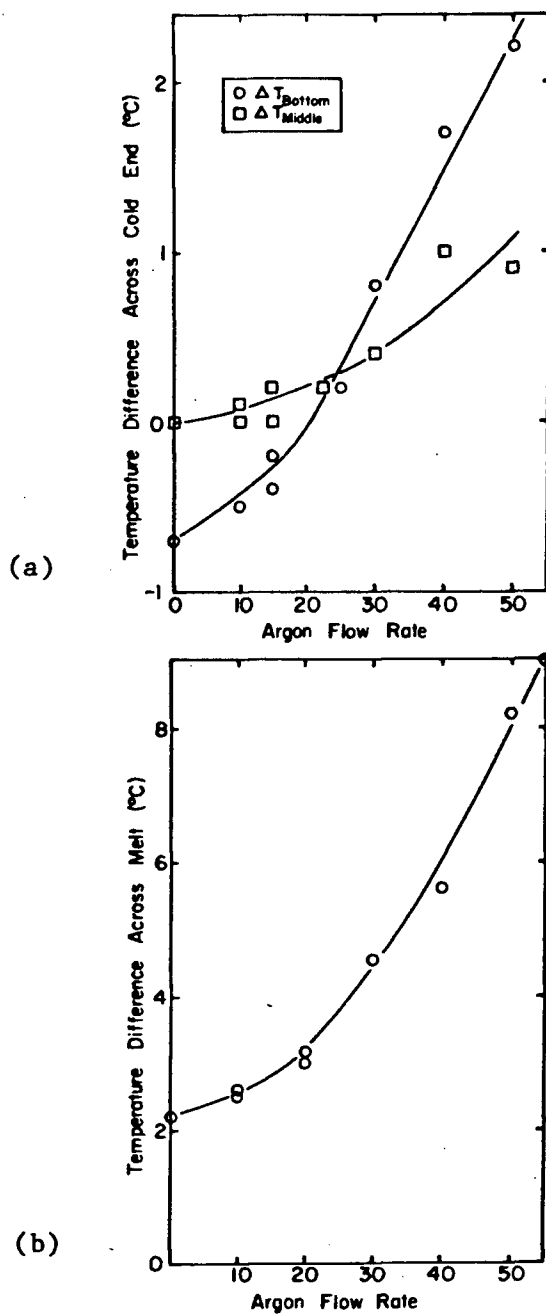


FIGURE 3.9 Graphs showing behaviour of temperature differences across (a) the cold end and (b) the melt versus argon flow rate for experiment B.

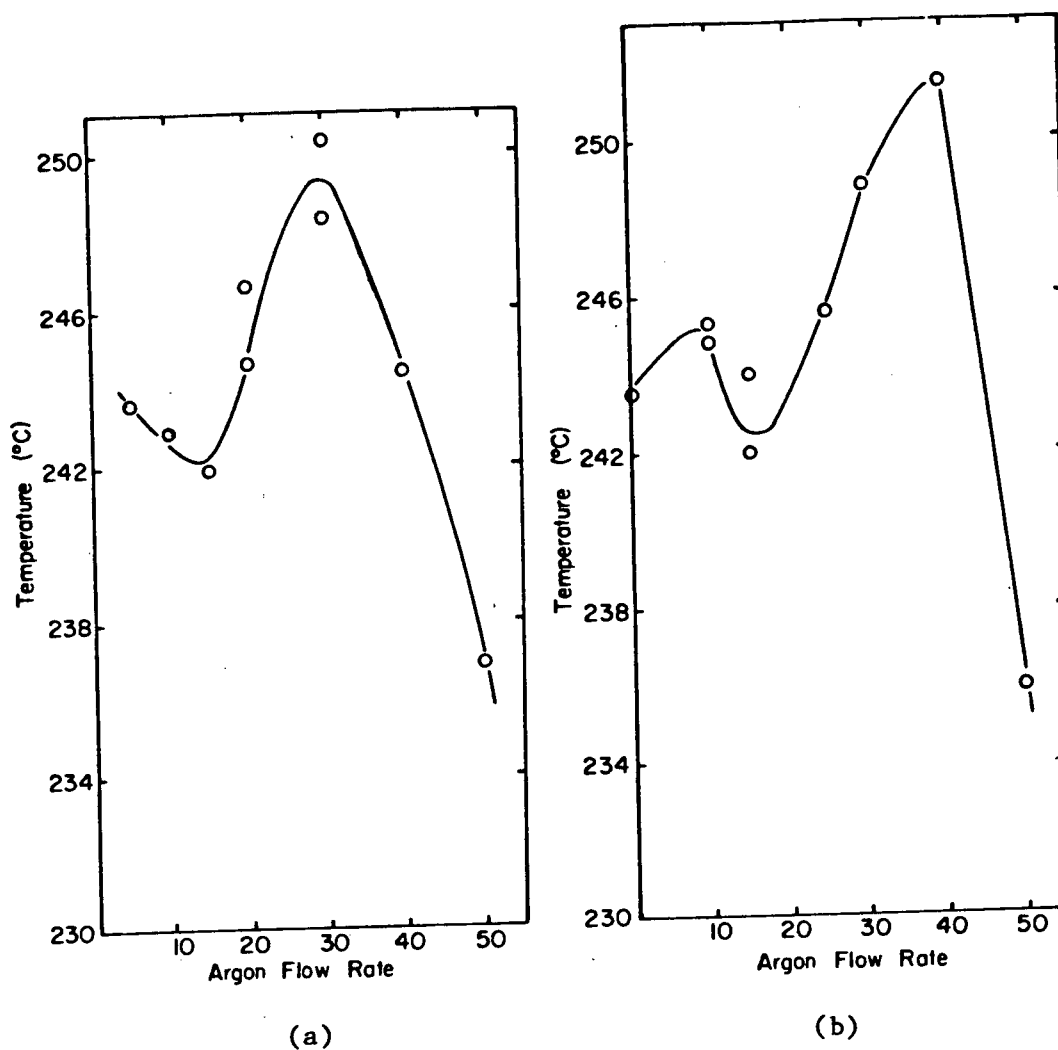


FIGURE 3.10 Graphs of temperature at centre of outside face of cold end versus argon flow rate for (a) experiment A and (b) experiment B.

the curves are only given for one thermocouple they are typical of all temperatures throughout the cell for a given experiment. In experiment A, the temperature showed an initial decrease (region I) which was followed by a large increase (region II) after which the temperature decreased steadily, as shown in Figure 3.10(a). In experiment B, the temperature curve was similar except for a small increase which preceded the initial decrease in temperature, as shown in Figure 3.10(b).

The temperature curve in Figure 3.10(a) could be explained if some argon gas had leaked into the furnace. Although the cold end was shielded to prevent argon gas from flowing into the furnace, some gas may have escaped. The forced convection produced in the furnace atmosphere by this flow of gas would increase the heat transfer rate between the furnace walls and the cell. This phenomena would explain the increase observed in region II. Beyond a certain argon gas flow rate the enhancement in the heat transfer in the furnace would reach some limit and the temperature would then decrease with increasing flow rate as observed in region III. It is interesting to note that the linearity observed in Figure 3.7(a) occurred for the temperature differences corresponding to the region III temperature data.

One additional observation should be made before proceeding to the next section. The temperatures at the bottom and middle of the inside face of the cold end were always within 0.2°C of each other and were often the same. Therefore the disparity in the observed values of

the temperature difference across the bottom and middle sections of the cold end is due to the difference in the temperatures at the outside face. The argon gas flow should have been approximately the same for both sections although if some nonuniformity existed it is likely that the flow was higher to the middle section than to the bottom section. Consequently there does seem to be any obvious explanation for the difference in heat flow rates that is implied by the difference in the temperatures.

3.3.3 Calculation of the Effective Thermal Conductivity

The values for k_{eff} were calculated from the slopes in Figure 3.7 using equation 3.1.2. The results are given in Table IV. The slopes for Figure 3.7(a) were calculated using linear regression of the data points corresponding to region III in Figure 3.10(a). The slopes in Figure 3.7(b) were calculated by using linear regression of the last three data points although only two actually lie in region IV of Figure 3.9(b).

For both experimental cases, the value of k_{eff} calculated from the data for the bottom section of the cold end is much higher than that calculated for the middle section of the cold end. Looking at the ratio of k_{eff} to k_{sn} , the normal thermal conductivity of tin, the enhancement is seven to ten times k_{sn} according to the data from the middle section

TABLE IV CALCULATION OF EFFECTIVE THERMAL CONDUCTIVITY

EXPERIMENT	LOCATION (COLD END)	k_{cold} $\left(\frac{\text{cal}}{\text{cm-sec-}^{\circ}\text{C}}\right)$	d_{melt} (cm)	d_{melt} (cm)	$\frac{1}{m}$	k_{eff} $\left(\frac{\text{cal}}{\text{cm-sec-}^{\circ}\text{C}}\right)$	$\frac{k_{\text{eff}}}{k_{\text{Sn}}}$
A-Using heater & Ar cooling	Middle	0.927	10.0	1.25	0.0733	0.5435	6.8
	Bottom	0.927	10.0	1.25	0.4625	3.430	~ 43
B-Only argon cooling used	Middle	0.927	10.0	1.25	0.1036	0.7685	9.6
	Bottom	0.927	10.0	1.25	0.3472	2.575	~ 32

and is thirty to forty times k_{sn} according to data from the bottom section. Judging from these results, it is not reasonable to use a plot of the temperature difference across the bottom section of the cold end versus the temperature difference across the mid-plane of the melt to calculate k_{eff} .

4.0 MATHEMATICAL MODEL

In previous mathematical models of fluid flow in a rectangular cavity, the hot and cold ends of the cell have been assumed to be isothermal. However in a real system it is difficult to ensure uniform temperatures at the ends and there is usually some temperature difference in the vertical direction. This model was developed to observe the effect of non-uniform boundary temperatures. In addition, the model was used to compare convective flow in liquid tin with that in liquid steel.

4.1 GOVERNING EQUATIONS

The energy equation, the Navier-Stokes equations and the continuity equation are needed to solve for the temperature and velocity fields. The following are the form of these equations for the two-dimensional system shown in Figure 4.1:

The energy equation:

$$\frac{\partial T^*}{\partial t^*} + u^* \frac{\partial T^*}{\partial x^*} + v^* \frac{\partial T^*}{\partial y^*} = \frac{k}{\rho C_p} \left(\frac{\partial^2 T^*}{\partial x^{*2}} + \frac{\partial^2 T^*}{\partial y^{*2}} \right) \quad (4.1.1)$$

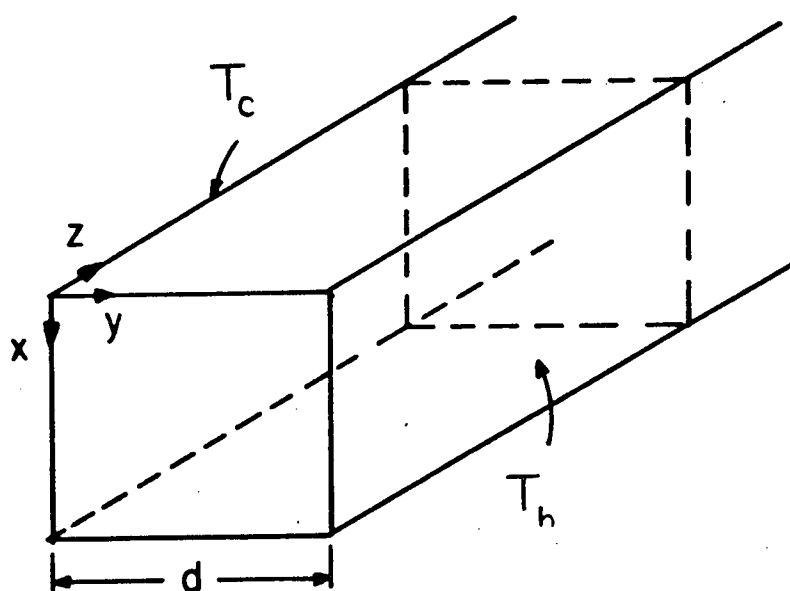


FIGURE 4.1 System of reference for mathematical model.

The Navier-Stokes equations:

-for momentum transfer in the x-direction,

$$\frac{\partial u^*}{\partial t^*} + u^* \frac{\partial u^*}{\partial x^*} + v^* \frac{\partial u^*}{\partial y^*} = - \frac{1}{\rho_m} \frac{\partial P^*}{\partial x^*} + \nu \left(\frac{\partial^2 u^*}{\partial x^{*2}} + \frac{\partial^2 u^*}{\partial y^{*2}} \right) - g\beta(T^* - T_o^*) \quad (4.1.2)$$

-for momentum transfer in the y-direction,

$$\frac{\partial v^*}{\partial t^*} + u^* \frac{\partial v^*}{\partial x^*} + v^* \frac{\partial v^*}{\partial y^*} = - \frac{1}{\rho_m} \frac{\partial P^*}{\partial y^*} + \nu \left(\frac{\partial^2 v^*}{\partial x^{*2}} + \frac{\partial^2 v^*}{\partial y^{*2}} \right) \quad (4.1.3)$$

The continuity equation:

$$\frac{\partial u^*}{\partial x^*} + \frac{\partial v^*}{\partial y^*} = 0 \quad (4.1.4)$$

In applying these equations the following assumptions have been made:

- 1) Fluid properties have been assumed constant except for one term which accounts for the temperature dependence of the density

- 2) Viscous dissipation and compressibility effects have been neglected
- 3) There is no heat generation in the fluid
- 4) The applied temperature difference is small compared to $1/\beta$ (where β is the coefficient of thermal expansion)

4.1.1 Dimensionless Variables

The asterisks used in equations 4.1.1 to 4.1.4 have been used to distinguish the marked variables from their dimensionless form. For computational purposes it is easier to use the dimensionless variables in the governing equations therefore the following dimensionless variables were introduced:

$$\begin{aligned}
 x &= \frac{x^*}{d}, & y &= \frac{y^*}{d}, & t &= \frac{t^* v}{d^2} \\
 u &= \frac{u^* d}{v}, & v &= \frac{v^* d}{v} & & (4.1.5) \\
 T &= \frac{T^* - T_o^*}{T_h^* - T_o^*}, & P &= \frac{P^* d^2}{\rho_m v^2}
 \end{aligned}$$

$$Pr = \frac{\mu C_p}{k}, \quad Gr^\bullet = \frac{g \beta d^3 (T_h^* - T_o^*)}{\nu^2}$$

where T_h^* = Temperature of the hot end

T_o^* = Average temperature of the cell

$$= \frac{T_h^* + T_c^*}{2}$$

T_c^* = Temperature of the cold end

d = Width across cell

The Grashof number as defined here is a modified version of the standard Grashof number since it is calculated using one-half the temperature difference across the cell rather than the total temperature difference. The superscript (\bullet) has been used to distinguish the modified Grashof number from the standard Grashof number.

Substituting these dimensionless parameters into equations 4.1.1 to 4.1.4. yields:

$$\frac{\partial T}{\partial t} + u \frac{\partial T}{\partial x} + v \frac{\partial T}{\partial y} = \frac{1}{Pr} \left(\frac{\partial^2 T}{\partial x^2} + \frac{\partial^2 T}{\partial y^2} \right) \quad (4.1.6)$$

$$\frac{\partial u}{\partial t} + u \frac{\partial u}{\partial x} + v \frac{\partial u}{\partial y} = -Gr \cdot T - \frac{\partial P}{\partial x} + \frac{\partial^2 u}{\partial x^2} + \frac{\partial^2 u}{\partial y^2} \quad (4.1.7)$$

$$\frac{\partial v}{\partial t} + u \frac{\partial v}{\partial x} + v \frac{\partial v}{\partial y} = -\frac{\partial P}{\partial y} + \frac{\partial^2 v}{\partial x^2} + \frac{\partial^2 v}{\partial y^2} \quad (4.1.8)$$

$$\frac{\partial u}{\partial x} + \frac{\partial v}{\partial y} = 0 \quad (4.1.9)$$

Equations 4.1.7 and 4.1.8 can be combined by differentiating equation 4.1.7 with respect to y and equation 4.1.8. with respect to x , subtracting and using equation 4.1.9 to eliminate terms to give,

$$\begin{aligned} \frac{\partial}{\partial t} \left(\frac{\partial u}{\partial y} - \frac{\partial v}{\partial x} \right) + u \frac{\partial^2 u}{\partial x \partial y} + v \frac{\partial^2 u}{\partial y^2} - u \frac{\partial^2 v}{\partial x^2} - v \frac{\partial^2 v}{\partial y \partial x} = \\ -Gr \cdot \frac{\partial T}{\partial y} + \frac{\partial (\nabla^2 u)}{\partial y} - \frac{\partial (\nabla^2 v)}{\partial x} \end{aligned} \quad (4.1.10)$$

4.1.2 Stream Function and Vorticity

To simplify equation 4.1.10, the concepts of the stream function and the vorticity were introduced. The vorticity, ξ is defined as:

$$\xi = \frac{\partial v}{\partial x} - \frac{\partial u}{\partial y} \quad (4.1.11)$$

The stream function, ϕ is defined by the following equations:

$$u = \frac{\partial \phi}{\partial y} \quad (4.1.12)$$

$$v = - \frac{\partial \phi}{\partial x} \quad (4.1.13)$$

Substituting the vorticity into equation 4.1.10 yields the vorticity equation:

$$\frac{\partial \xi}{\partial t} + u \frac{\partial \xi}{\partial x} + v \frac{\partial \xi}{\partial y} = Gr \cdot \frac{\partial T}{\partial y} + \nabla^2 \xi \quad (4.1.14)$$

Equation 4.1.9 is automatically satisfied by the definition of the stream function. To solve for the stream function, equations 4.1.12 and 4.1.13 are substituted into equation 4.1.11 to give the stream function equation:

$$\xi = - \left(\frac{\partial^2 \phi}{\partial x^2} + \frac{\partial^2 \phi}{\partial y^2} \right) \quad (4.1.15)$$

Equations 4.1.6, 4.1.12, 4.1.13, 4.1.14 and 4.1.15 form the set of equations used to solve the problem of natural convection in a square cavity.

4.2 INITIAL AND BOUNDARY CONDITIONS

The temperature and velocity profiles calculated in this model are steady-state. However to reach a solution, the time-derivatives have been retained in the governing equations so that the computer will produce a time-varying solution which converges to the steady-state solution. This technique requires the definition of initial conditions for the temperature, stream function and vorticity. The initial conditions used were,

$$\begin{array}{lcl} t=0 & 0 = x = 1.0 \\ & 0 = y = 1.0 \end{array} \left. \vphantom{\begin{array}{l} t=0 \\ 0 = x = 1.0 \\ 0 = y = 1.0 \end{array}} \right\} \xi = 0, \phi = 0, T = 0 \quad (4.2.1)$$

The solution of the system of equations also requires the definition of boundary conditions. Since the velocity must be zero at the boundaries the gradient of the stream function was taken to be zero at the the boundaries. The top and bottom surfaces were assumed to be either insulating or perfectly conducting. The ends were taken to be either isothermal or having a linear temperature drop. Expressed numerically the boundary conditions were,

$$t > 0 \quad x = 0.0, 1.0 \quad \psi = \frac{\partial \psi}{\partial x} = 0$$

i) Insulated boundary

$$\frac{\partial T}{\partial x} = 0$$

ii) Perfectly conducting

$$T = -1.0 + 2.0*(1 - y)$$

$$y=0.0 \quad \phi = \frac{\partial \phi}{\partial y} = 0 \quad (4.2.2)$$

i) Isothermal end

$$T = -1.0$$

ii) With temperature drop

$$T = -1.0 + (PCT/2)*x$$

$$y = 1.0 \quad \phi = \frac{\partial \phi}{\partial y} = 0$$

i) Isothermal end

$$T = +1.0$$

ii) With temperature drop

$$T = (1-PCT/2)*1.0 - (PCT/2)*x$$

where PCT = temperature drop along end expressed as percentage of ΔT_{melt}

4.3 THE FINITE DIFFERENCE EQUATIONS

The solution of the differential equations is achieved by using finite difference approximations to the governing equations. The

numerical technique used in this model was the implicit alternating technique, commonly referred to as the ADI method. The model used the ADI technique to solve for the temperature, vorticity and stream function equations. Other models^{12,15} have used a relaxation technique to solve for the stream function equation (equation 4.1.15). However these models were developed for use with much higher Prandtl numbers and lower Grashof numbers than those used for this model and had reported problems when using low Prandtl numbers. Since the model by Stewart was successful at the low Prandtl numbers and high Grashof numbers that would be needed for this model the same approach was adopted.

The ADI technique divides the time step, $\Delta\tau$ into two parts. For the first half of the time step all the x-derivatives are implicit and all the y-derivatives are explicit. Implicit derivatives are evaluated at $t=t_2$ and explicit derivatives are evaluated at $t=t_1$, where $t_2=t_1+\Delta\tau/2$. The values for $t=t_1$ represent the values at the previous half of the time step and are known at $t=t_2$. The values at $t=t_2$ are unknown and must be solved before proceeding to the second half of the time step. For the second half of the time step, the y-derivatives are implicit and the x-derivatives are explicit.

The finite difference approximations were generated from expansions based on the square grid system of points as shown in Figure 4.2. The subscripts i and j indicate the position of the node in the x and y directions respectively. The following equations use an asterisk

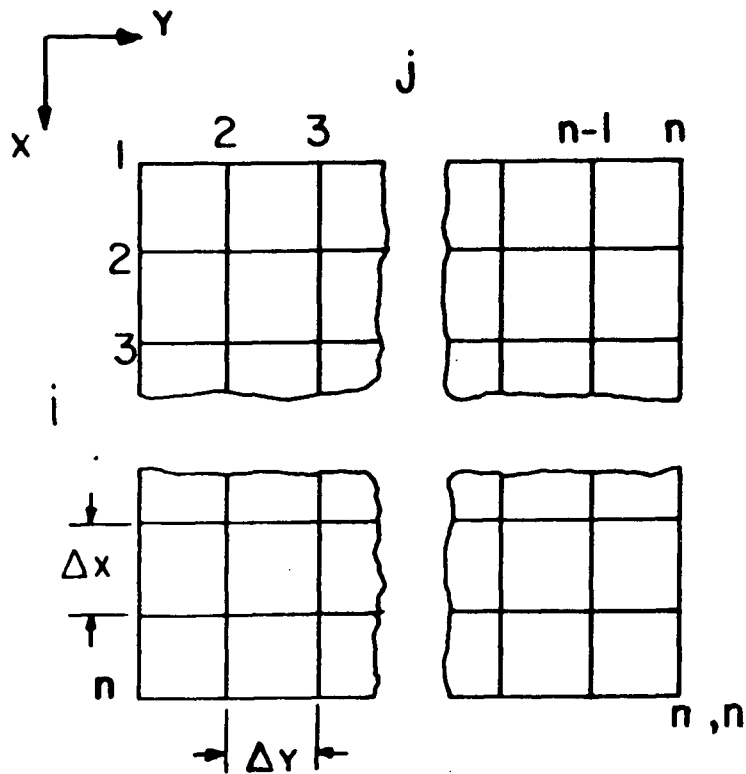


FIGURE 4.2 Grid system used in mathematical model.

superscript (*) to denote variables that are evaluated at $t=(n+1/2)\Delta\tau$, and the apostrophe superscript (') to denote variables that are evaluated at $t=(n+1)\Delta\tau$. Variables without superscripts are evaluated at $t=n\Delta\tau$. The finite difference approximation to the temperature equation for the first half of the time step is,

$$\begin{aligned} \frac{T_{i,j}^* - T_{i,j}}{\Delta\tau/2} + u_{i,j} \frac{T_{i+1,j}^* - T_{i-1,j}^*}{2\Delta x} + v_{i,j} \frac{T_{i,j+1}^* - T_{i,j-1}^*}{2\Delta y} = \\ \frac{1}{Pr} \frac{T_{i-1,j}^* - 2T_{i,j}^* + T_{i+1,j}^*}{(\Delta x)^2} + \frac{1}{Pr} \frac{T_{i,j-1}^* - 2T_{i,j}^* + T_{i,j+1}^*}{(\Delta y)^2} \quad (4.3.1) \end{aligned}$$

For the second half of the time step,

$$\begin{aligned} \frac{T_{i,j}' - T_{i,j}^*}{\Delta\tau/2} + u_{i,j} \frac{T_{i+1,j}^* - T_{i-1,j}^*}{2\Delta x} + v_{i,j} \frac{T_{i,j+1}^* - T_{i,j-1}^*}{2\Delta y} = \\ \frac{1}{Pr} \frac{T_{i-1,j}^* - 2T_{i,j}^* + T_{i+1,j}^*}{(\Delta x)^2} + \frac{1}{Pr} \frac{T_{i,j-1}^* - 2T_{i,j}^* + T_{i,j+1}^*}{(\Delta y)^2} \quad (4.3.2) \end{aligned}$$

The finite difference equation for the vorticity for the first half of the time step,

$$\frac{\xi_{i,j}^* - \xi_{i,j}}{\Delta\tau/2} + u_{i,j} \frac{\xi_{i+1,j}^* - \xi_{i-1,j}^*}{2\Delta x} + v_{i,j} \frac{\xi_{i,j+1}^* - \xi_{i,j-1}^*}{2\Delta y} =$$

$$Gr \cdot \frac{T'_{i,j+1} - T'_{i,j-1}}{2\Delta y} + \frac{\xi_{i-1,j}^* - 2\xi_{i,j}^* + \xi_{i+1,j}^*}{(\Delta x)^2} + \frac{\xi_{i,j-1} - 2\xi_{i,j} + \xi_{i,j+1}}{(\Delta y)^2} \quad (4.3.3)$$

For the second half of the time step,

$$\frac{\xi'_{i,j} - \xi^*_{i,j}}{\Delta\tau/2} + u_{i,j} \frac{\xi^*_{i+1,j} - \xi^*_{i-1,j}}{2\Delta x} + v_{i,j} \frac{\xi'_{i,j+1} - \xi'_{i,j-1}}{2\Delta y} = Gr \cdot \frac{T'_{i,j+1} - T'_{i,j-1}}{2\Delta y} + \frac{\xi^*_{i-1,j} - 2\xi^*_{i,j} + \xi^*_{i+1,j}}{(\Delta x)^2} + \frac{\xi'_{i,j-1} - 2\xi'_{i,j} + \xi'_{i,j+1}}{(\Delta y)^2} \quad (4.3.4)$$

To solve the stream function equation, a time derivative is introduced to equation 4.1.15 to produce an unsteady state solution which converges to the steady state problem. Using this approach the finite difference equation for the stream function for the first half of the time step, is,

$$\frac{\phi^*_{i,j} - \phi_{i,j}}{\Delta\tau/2} = \xi'_{i,j} + \frac{\phi^*_{i-1,j} - 2\phi^*_{i,j} + \phi^*_{i+1,j}}{(\Delta x)^2} +$$

$$\frac{\phi_{i,j-1} - 2\phi_{i,j} + \phi_{i,j+1}}{(\Delta y)^2} \quad (4.3.5)$$

For the second half of the time step,

$$\frac{\phi'_{i,j} - \phi^*_{i,j}}{\Delta \tau/2} = \xi_{i,j} + \frac{\phi^*_{i-1,j} - 2\phi^*_{i,j} + \phi^*_{i+1,j}}{(\Delta x)^2} +$$

$$\frac{\phi'_{i,j-1} - 2\phi'_{i,j} + \phi'_{i,j+1}}{(\Delta y)^2} \quad (4.3.6)$$

To solve the temperature, vorticity and stream function equations, the above equations are rearranged to collect all the unknown terms on one side of the equation and the known terms on the right hand side of the equation. A complete list of the rearranged equations can be found in appendix II of reference 8. The resulting coefficient matrix for the unknown variables is a tridiagonal matrix which can be easily inverted for solution. Once the temperature, vorticity and stream function have been calculated for each node, the new velocities are calculated. Using equations 4.1.12 and 4.1.13, the following expansions were generated to solve for the velocities:

$$u_{i,j} = \left(\frac{\partial \phi}{\partial y} \right)_{i,j} = \frac{\phi_{i,j-2} - 8\phi_{i,j-1} + 8\phi_{i,j+1} - \phi_{i,j+2}}{12\Delta y} \quad (4.3.7)$$

$$v_{1,j} = -\left(\frac{\partial \phi}{\partial x}\right)_{1,j} = \frac{\phi_{i-2,j} - 8\phi_{i-1,j} + 8\phi_{i+1,j} - \phi_{i+2,j}}{12 \Delta x} \quad (4.3.8)$$

For points near the boundary a different expansion was used which was of the form:

$$u_{1,2} = \frac{-3\phi_{1,2} + 6\phi_{1,3} - \phi_{1,4}}{6 \Delta y} \quad (4.3.9)$$

$$v_{2,j} = \frac{3\phi_{2,j} - 6\phi_{3,j} + \phi_{4,j}}{6 \Delta x} \quad (4.3.10)$$

Expansions of a similar form were used for the other boundaries.

An additional calculation was performed to determine the boundary vorticities since no boundary condition was defined for the vorticity. Equation 4.1.15 was used to solve for the boundary vorticities. To satisfy the condition that the velocity must be zero normal to the boundary,

$$\text{at } x=0,1 \quad \frac{\partial^2 \phi}{\partial y^2} = 0 \quad \text{and at } y=0,1 \quad \frac{\partial^2 \phi}{\partial x^2} = 0 \quad (4.3.11)$$

Therefore at the boundary, equation 4.1.15 becomes,

$$\text{at } x=0,1 \quad \xi = -\frac{\partial^2 \phi}{\partial x^2} \quad \text{and at } y=0,1 \quad \xi = -\frac{\partial^2 \phi}{\partial y^2} \quad (4.3.12)$$

The expansions used for the boundaries were of the form,

$$\xi_{1,1} = - \frac{2\phi_{1,2}}{(\Delta y)^2} \quad (4.3.13)$$

4.4 RESULTS OF COMPUTER RUNS

During the development of the model it was found that a separate time step was needed for the solution of the stream function which was kept constant for all runs. This time step was larger than the time step used for the temperature and vorticity equations. In addition, convergence was much more rapid if the latter time step was changed as the program progressed. For Grashof numbers $>10^5$ even small changes in the temperature-vorticity time step would markedly affect the number of iterations that were required for convergence. No convergent solution was found for Grashof numbers $\geq 10^7$. From the results obtained, it would appear that adjusting the value of the stream function time step might increase model stability at the higher Grashof numbers. Close examination of the data used by Stewart did not reveal the time step used but it did show that a finer mesh size was used for Grashof number equal to 10^7 . The region of instability seems to occur for $Ra \geq 10^5$. This limit would seem to concur with the stability limit observed in other models of convection in a rectangular cavity^{12, 21}. The instability in the numerical model seems to be associated with the onset of secondary flows in the cavity.²¹

To test the computer program, isotherm, streamline and Nusselt number plots were generated for a square cavity with isothermal ends and insulated top and bottom boundaries using the Prandtl number for tin ($Pr = 0.0127$) and various Grashof numbers. Figures 4.3, 4.4 and 4.5 show the computer plots that were produced. The results were in excellent agreement with the plots generated by the numerical model of Stewart for similar Prandtl and Grashof values. In addition, velocity plots were generated which show the velocity distribution in the cell. The results, given in Figure 4.6, show the development of small secondary flows in the upper left and lower right corners of the velocity plot for $Gr = 10^6$.

The temperatures of the ends were adjusted so that there was a linear temperature drop from the top to the bottom of the ends. In the experiments, it was found that the temperatures at the top of the cell were usually cooler than at the bottom therefore the gradient in the model had the coolest temperatures at the top boundary. The temperature drop was expressed as a percentage of the temperature difference across the melt. For example, a 5% temperature drop at the end boundary would mean a difference of 0.1°C between top and bottom if the temperature difference across the cell was 2.0°C . Figure 4.7 shows the effect of a 5% and 10% temperature drop for $Pr=0.0127$ and $Gr=1.0 \times 10^5$. Figure 4.8 shows the effect of the same temperature drops for $Pr=0.0127$ and $Gr=1.0 \times 10^6$. The effect on the isotherms is particularly pronounced near the ends. The presence of the temperature gradients in the ends also

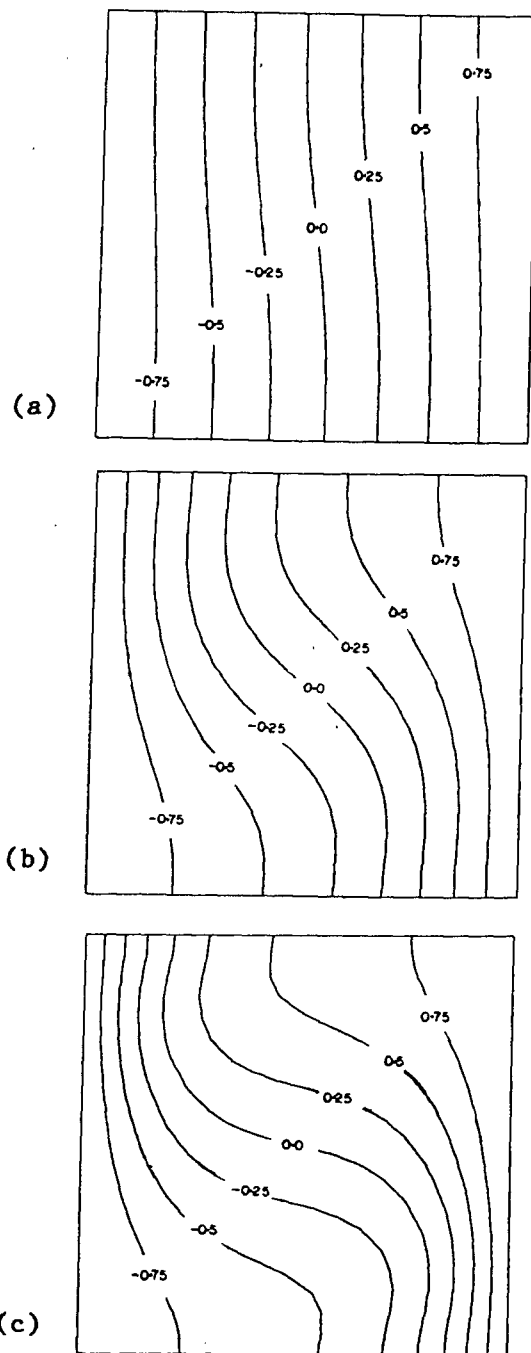


FIGURE 4.3 Isotherm distribution for $Pr=0.0127$ and (a) $Gr=1.0 \times 10^4$, (b) $Gr=1.0 \times 10^5$ and (c) $Gr=1.0 \times 10^6$.

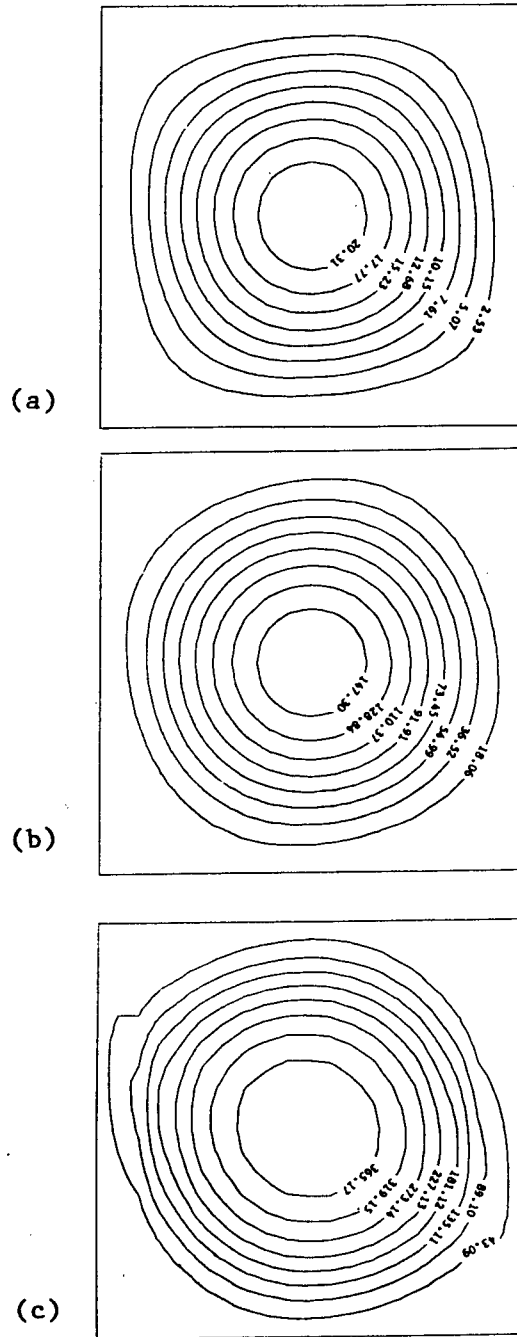


FIGURE 4.4 Streamline plot for $Pr=0.0127$ and (a) $Gr=1.0 \times 10^4$, (b) $Gr=1.0 \times 10^5$ and (c) $Gr=1.0 \times 10^6$.

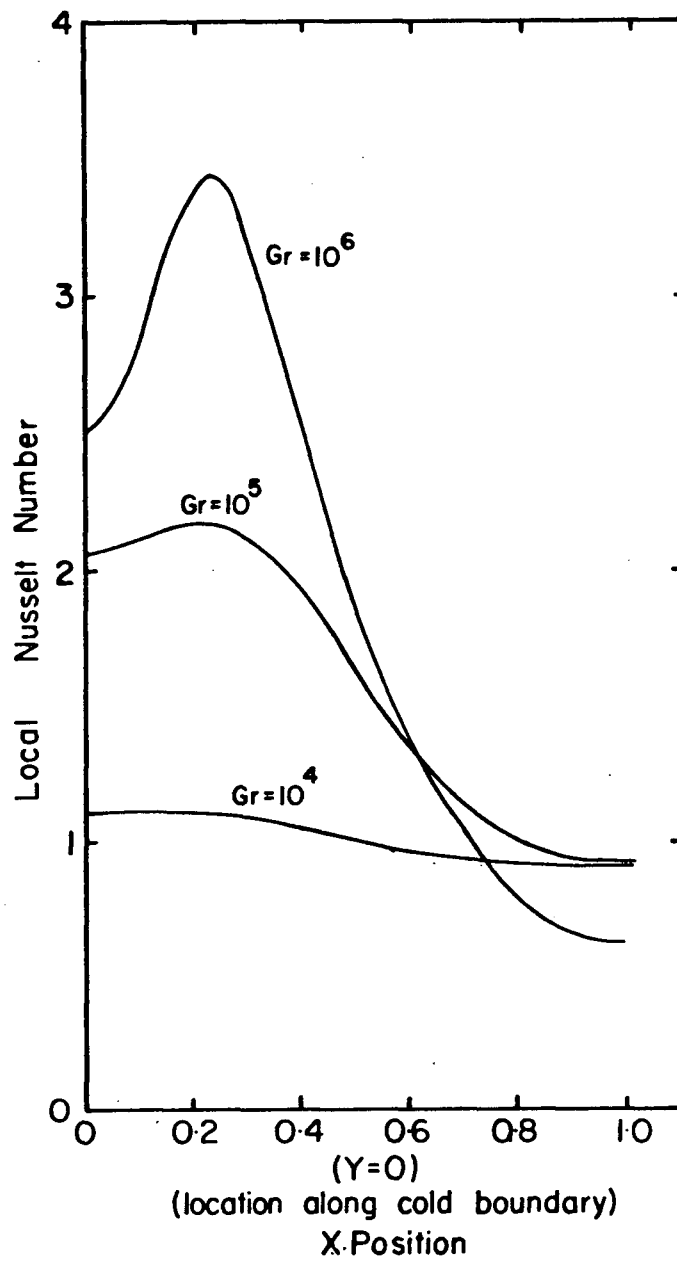


FIGURE 4.5 Nusselt number versus vertical (x) position along cold wall for $Pr=0.0127$ and $Gr=1.0 \times 10^4$, 1.0×10^5 and 1.0×10^6 .

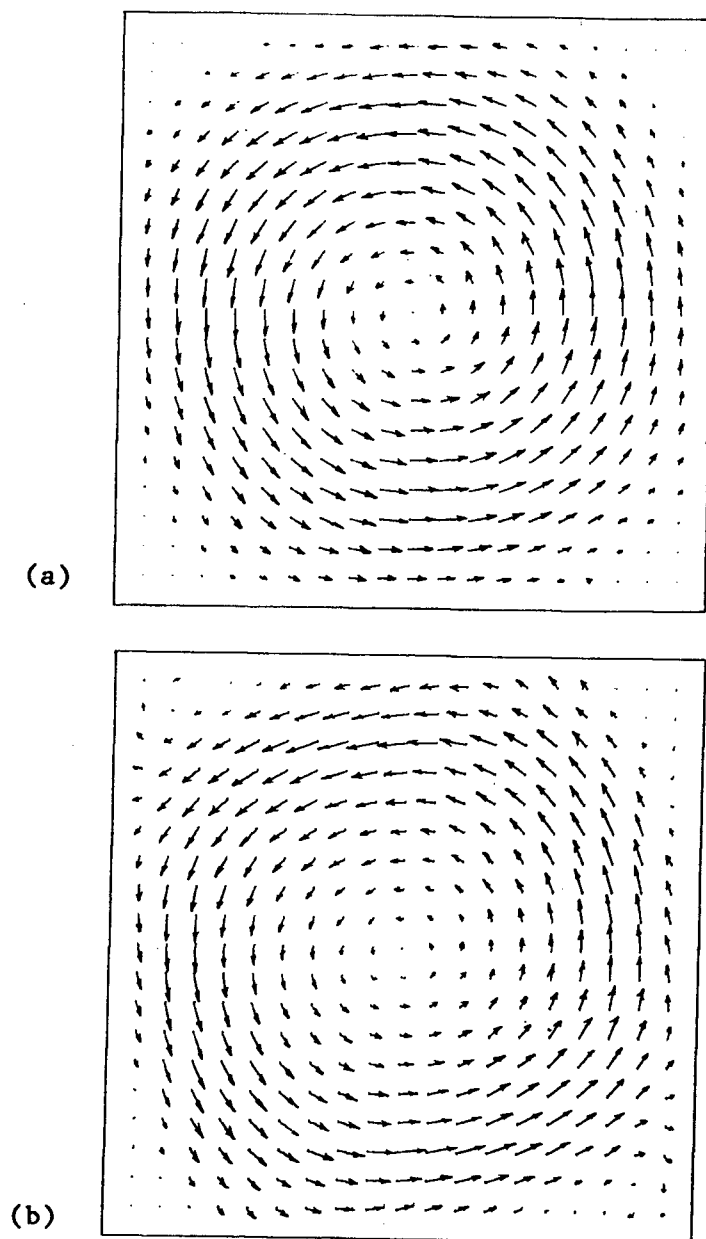


FIGURE 4.6 Normalized velocity field for $Pr=0.0127$ and (a) $Gr=10^5$ (maximum velocity = 487.44) and (b) $Gr=10^6$ (maximum velocity = 1185.09). Velocities given are dimensionless velocities.

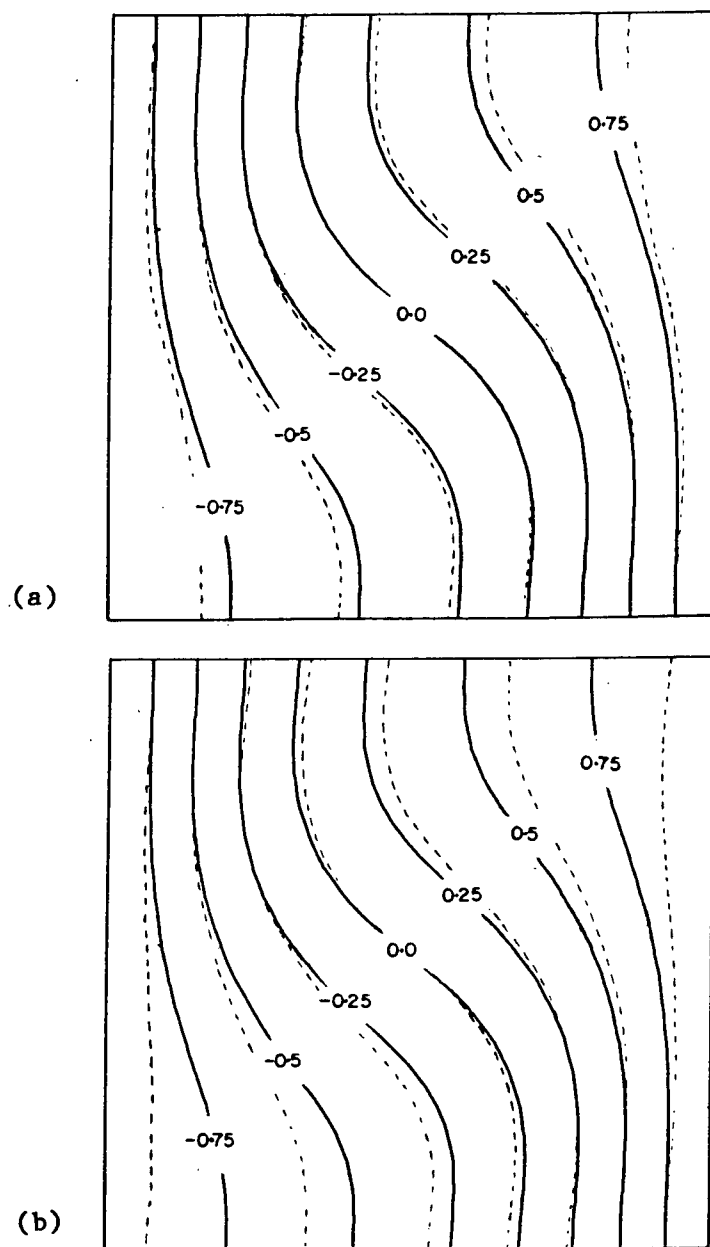


FIGURE 4.7 Isotherm plots with $Pr=0.0127$ and $Gr=1.0 \times 10^5$. Solid line indicates profiles for isothermal ends and dashed line indicates those for (a) a 5% drop along ends and (b) a 10% drop along ends.

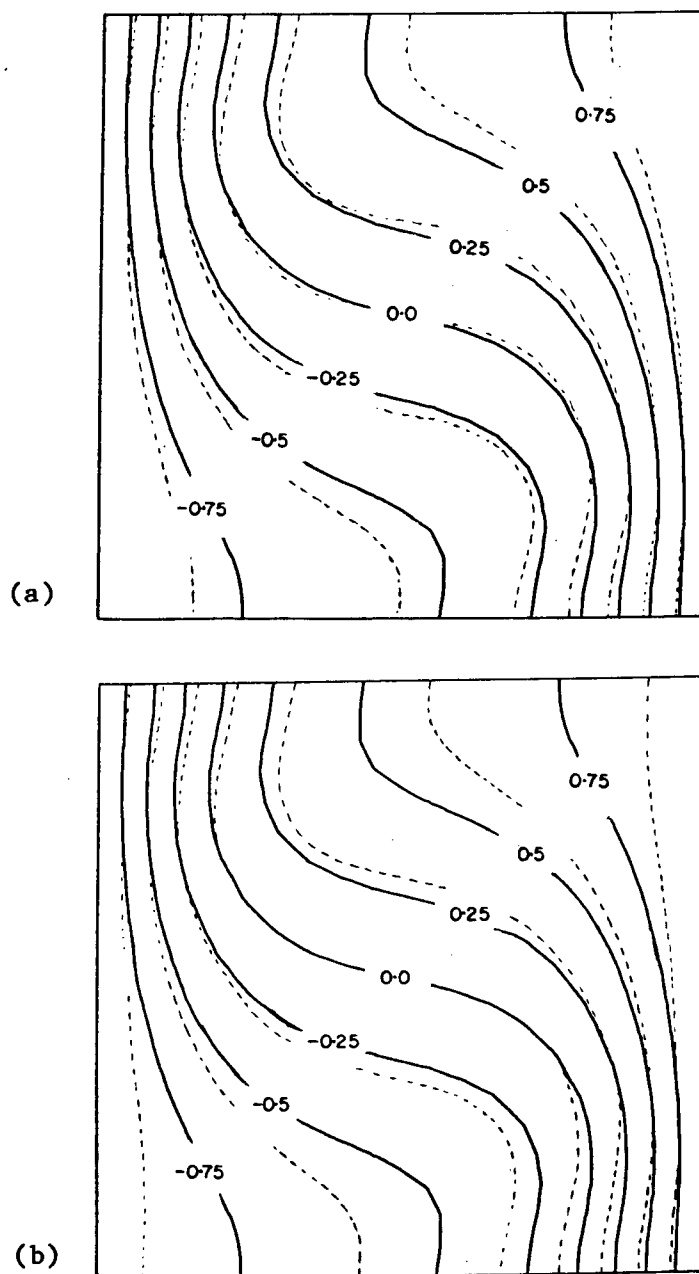


FIGURE 4.8 Isotherm plots with $Pr=0.0127$ and $Gr=1.0 \times 10^6$. Solid line indicates profiles for isothermal ends and dashed line indicates those for (a) a 5% drop along ends and (b) a 10% drop along ends.

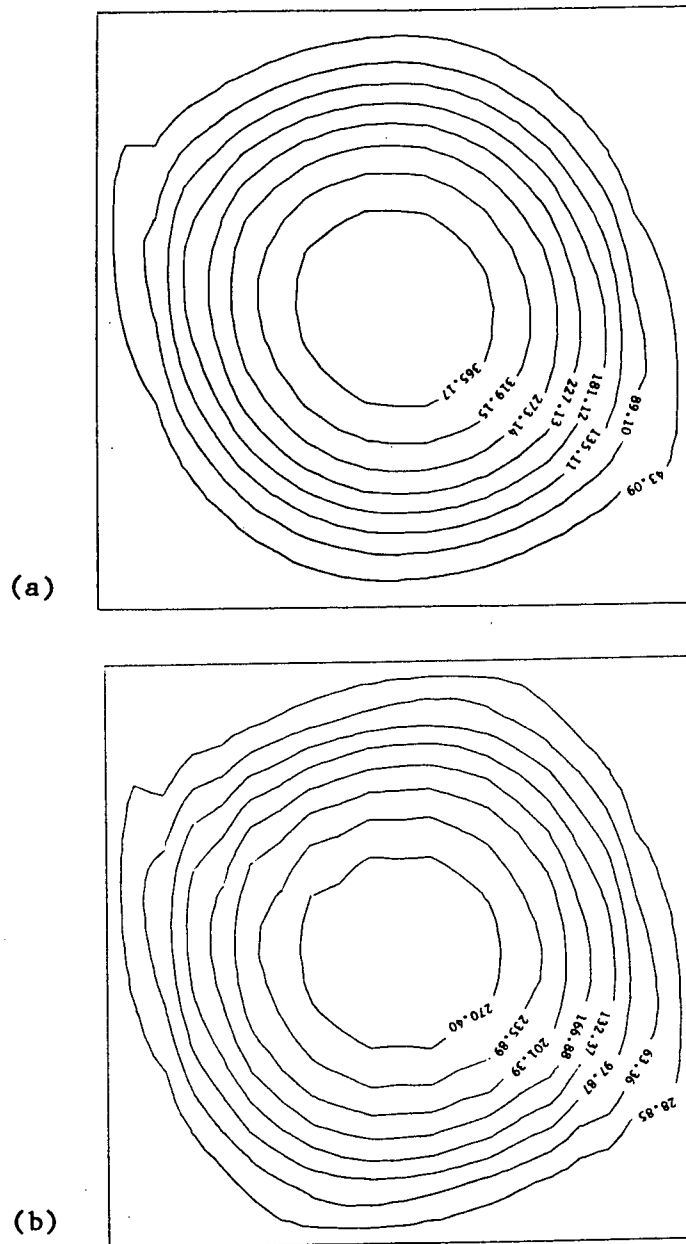


FIGURE 4.9 Streamline plot with $Pr=0.0127$ and $Gr=1.0 \times 10^6$ with (a) isothermal ends and (b) 10% drop along both ends (with coldest temperature at top).

affects the streamline distribution as shown in Figure 4.9. There is a slight effect on the shape of the streamlines. The maximum value of the stream function is lower when the gradients are present indicating slower velocities in the cavity. However the maximum velocity only decreased by about eight percent with a ten percent drop in the end temperatures.

The velocities that were measured for cell II appeared to be much higher than the velocities measured by Stewart. One major difference in the cell design between cell II and the cell used by Stewart was the fact that Stewart used a U-shaped piece inside the cell which connected the cold end to the hot end. This design avoided the problem of liquid tin leaking from the junction between the end piece and the bottom piece of the cell but it also provided a thermal link between the end pieces through which heat could flow. For such a situation it is conceivable that a temperature gradient would exist along the bottom of the cell. To investigate the effect of a temperature gradient along the bottom of the cell computer runs were performed with a linear gradient imposed along the bottom of the cell. For the results shown in Figures 4.10 and 4.11 the ends were taken to be isothermal and the top surface was insulating. The effect on the isotherms seems to be limited to the bottom of the cell. The values of the stream function are lower than when the bottom was taken to be insulating, especially for the higher Grashof number, indicating that the velocities would be slower. Computer runs were also performed for the case when there was linear temperature drops in both ends combined

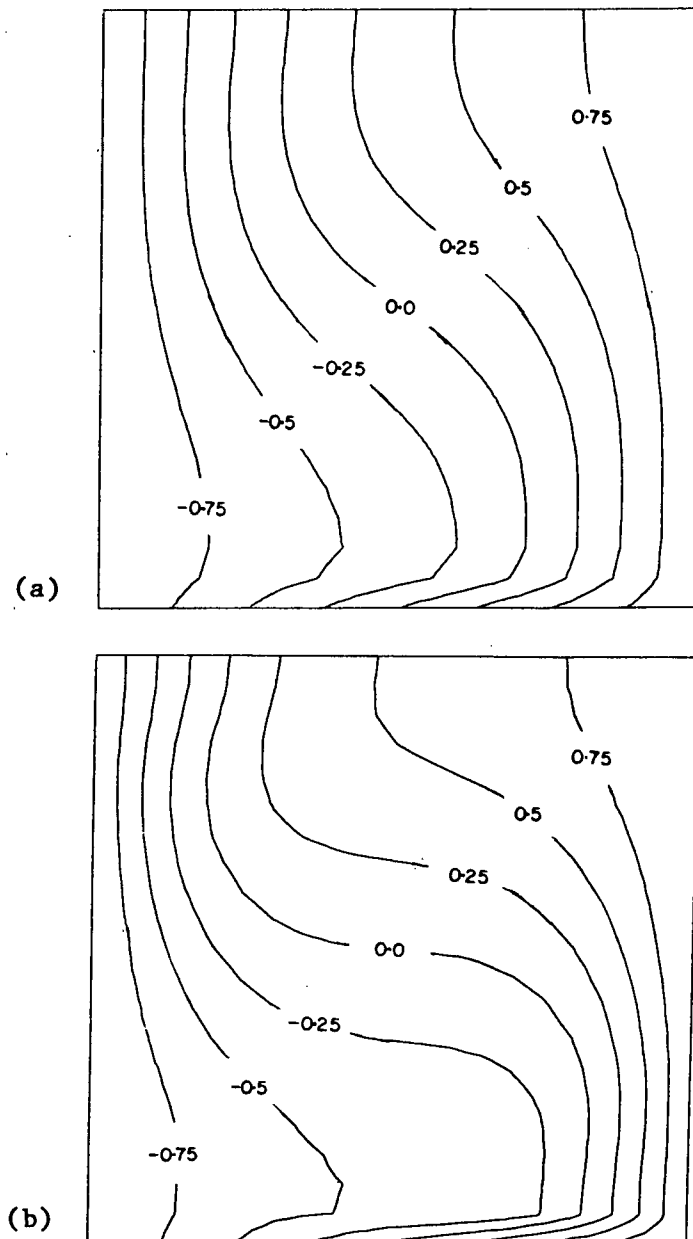


FIGURE 4.10 Isotherm plot with linear temperature gradient along bottom (isothermal ends and insulated top surface) with $Pr=0.0127$ and (a) $Gr=1.0 \times 10^5$ and (b) $Gr=1.0 \times 10^6$.

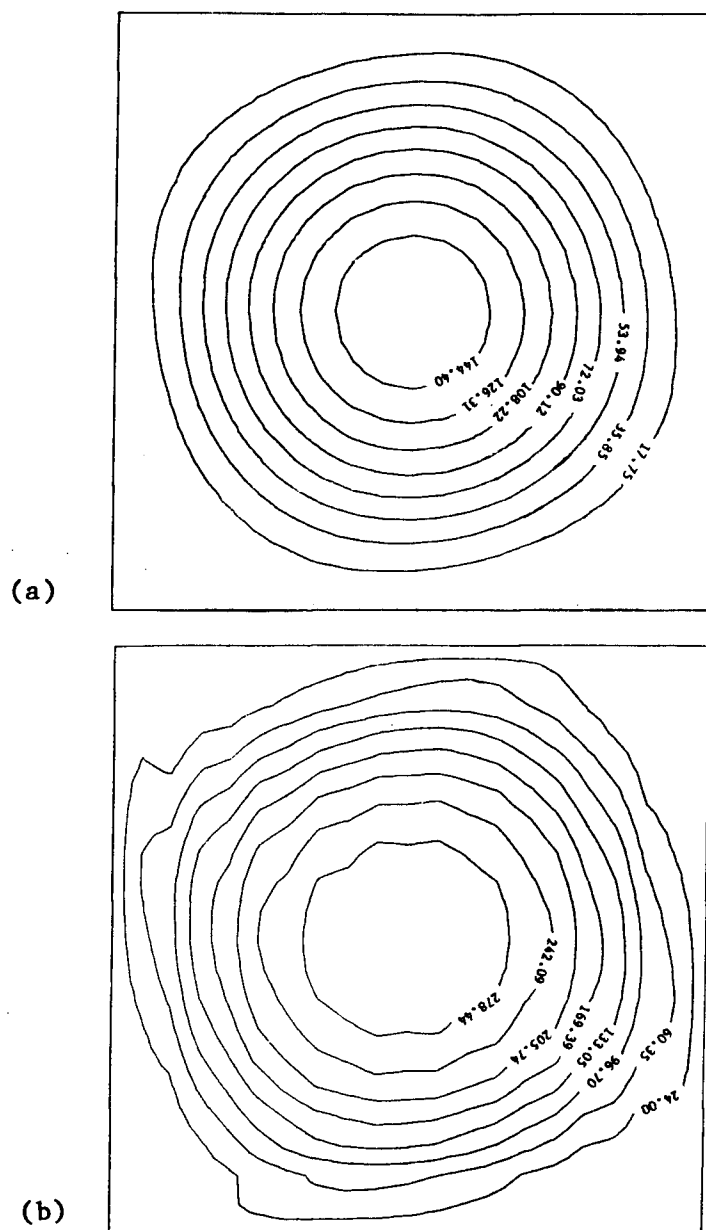


FIGURE 4.11 Streamline plots with linear temperature gradient along bottom (isothermal ends and insulated top surface) with $Pr=0.0127$ and (a) $Gr=1.0 \times 10^5$ and (b) $Gr=1.0 \times 10^6$.

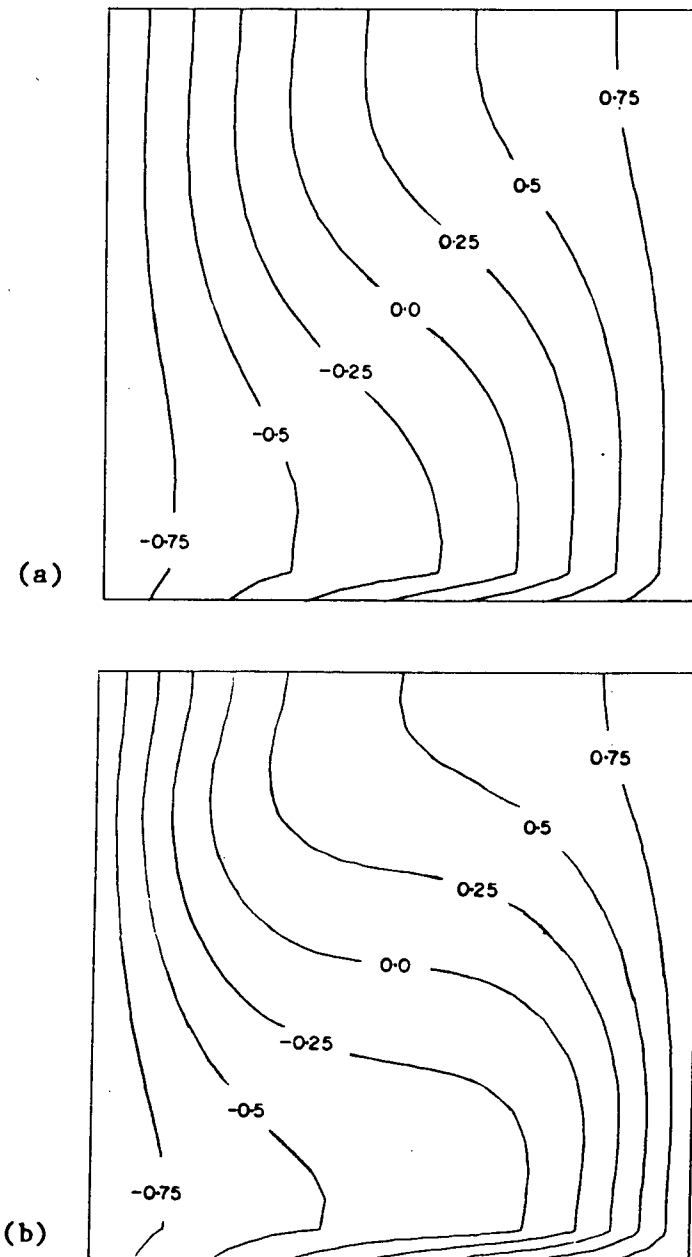


FIGURE 4.12 Isotherm plots with linear temperature gradient along bottom and 10% temperature drop along ends with $Pr=0.0127$ and (a) $Gr=1.0 \times 10^5$ and (b) $Gr=1.0 \times 10^6$.

with the linear temperature gradient along the bottom. The results do not differ greatly from those produced when assuming isothermal end temperatures with the linear gradient along the bottom, as shown in Figure 4.12.

The reduction in velocity due to the presence of the gradient along the bottom does not appear to be large enough to account for the difference in the results from cell II and the results of Stewart. Another factor which may have influenced the flow velocity is the heat flow out the side walls. The walls of the cell used by Stewart were made of 0.0625 inch aluminum sheet whereas the side wall for cell II was made of 0.1875 inch stainless steel. Therefore the walls for cell II were less conductive. A three-dimensional mathematical model would be necessary to estimate the effect on the velocities but such a model is beyond the scope of this study.

Finally, computer runs were performed to compare the differences in the responses of liquid tin and liquid steel to temperature differences of 0.5 °C and 0.01 °C. The results are shown in Figures 4.13 to 4.19. The isotherm plots do not differ greatly although there is more curvature in the isotherms for liquid steel. The difference in the streamline distribution is more noticeable for the 0.5 °C temperature difference. The velocity gradients in steel are much steeper near the edges of the cell at this temperature difference, as shown in Figure 4.18. However looking at the vertical scale, the

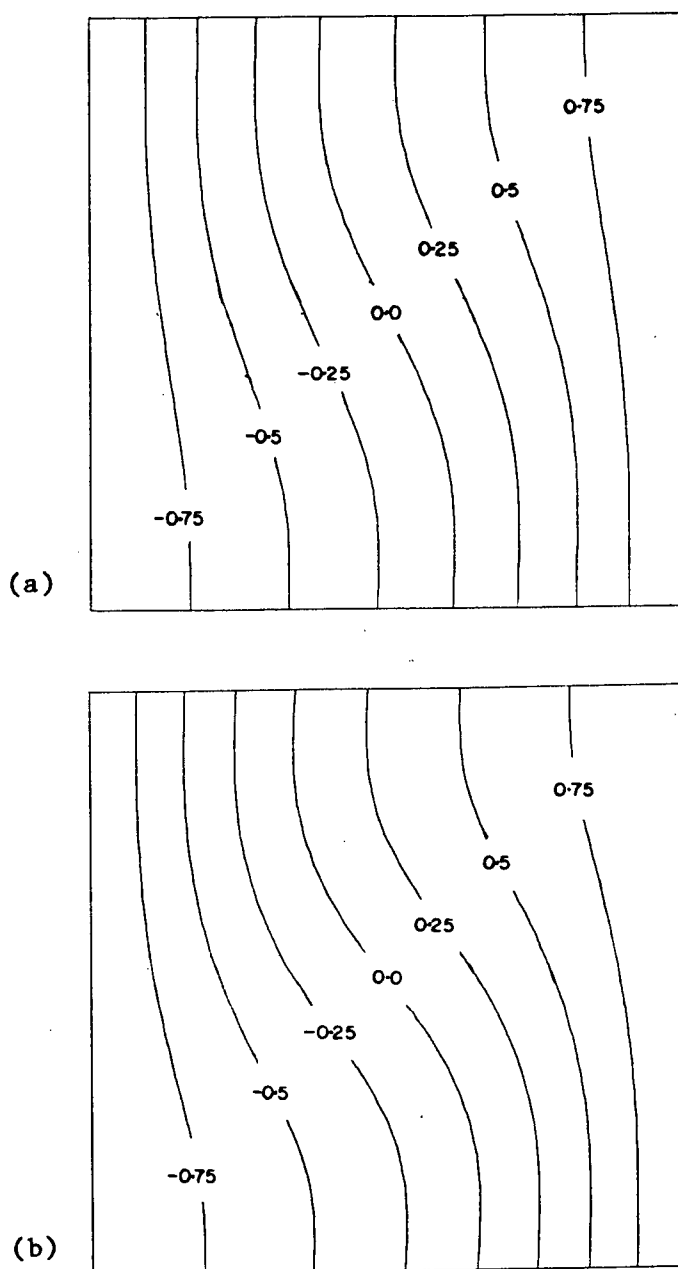


FIGURE 4.13 Isotherm distribution for a temperature difference of 0.01°C across cell for (a) liquid tin ($Pr=0.0127$ and $Gr=3.6 \times 10^4$) and (b) liquid steel ($Pr=0.11$ and $Gr=6.0 \times 10^3$).

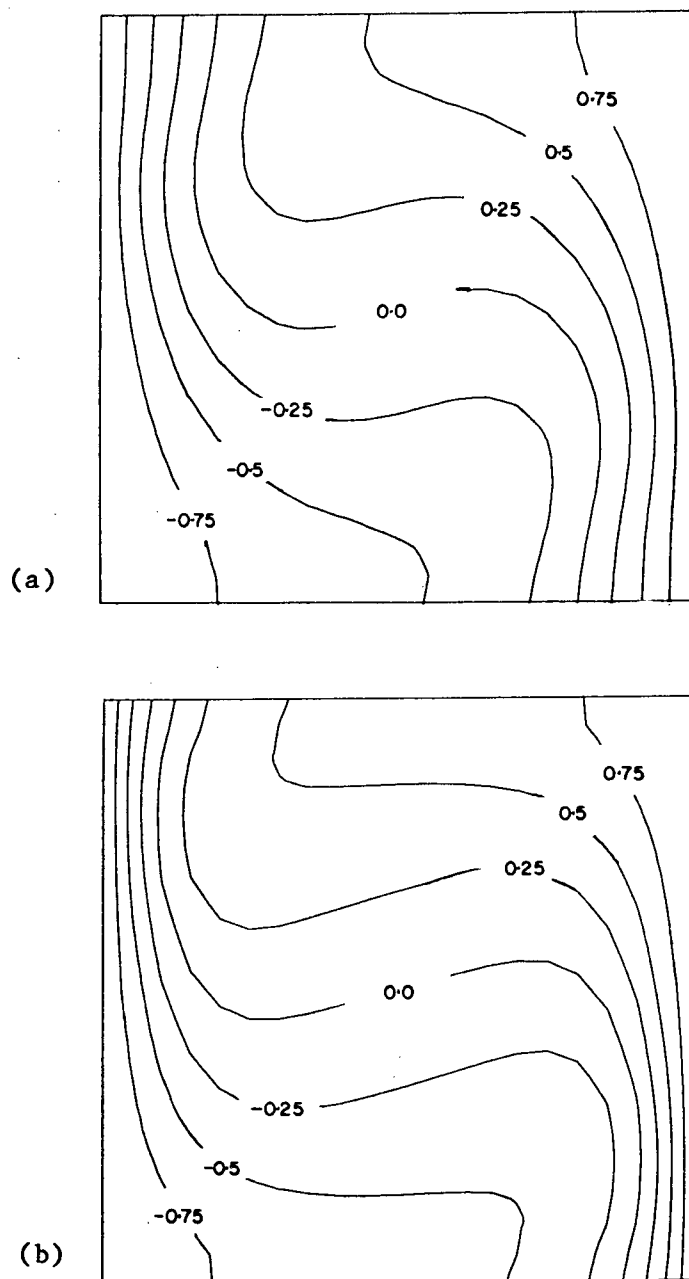


FIGURE 4.14 Isotherm distribution for a temperature difference of 0.5°C across cell for (a) liquid tin ($\text{Pr}=0.0127$ and $\text{Gr}=1.8 \times 10^6$) and (b) liquid steel ($\text{Pr}=0.0127$ and $\text{Gr}=3.0 \times 10^5$).

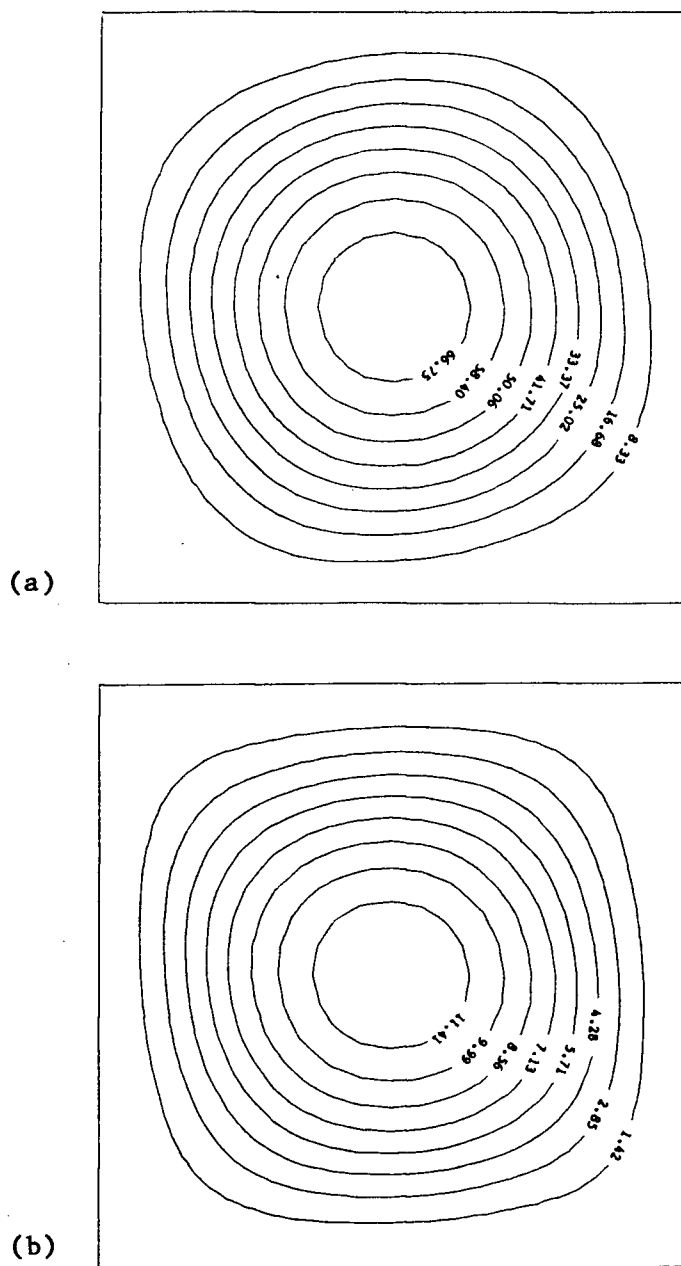


FIGURE 4.15 Streamline distribution for a temperature difference of 0.01°C across cell for (a) liquid tin ($\text{Pr}=0.0127$ and $\text{Gr}=3.6 \times 10^4$) and (b) liquid steel ($\text{Pr}=0.11$ and $\text{Gr}=6.0 \times 10^3$).

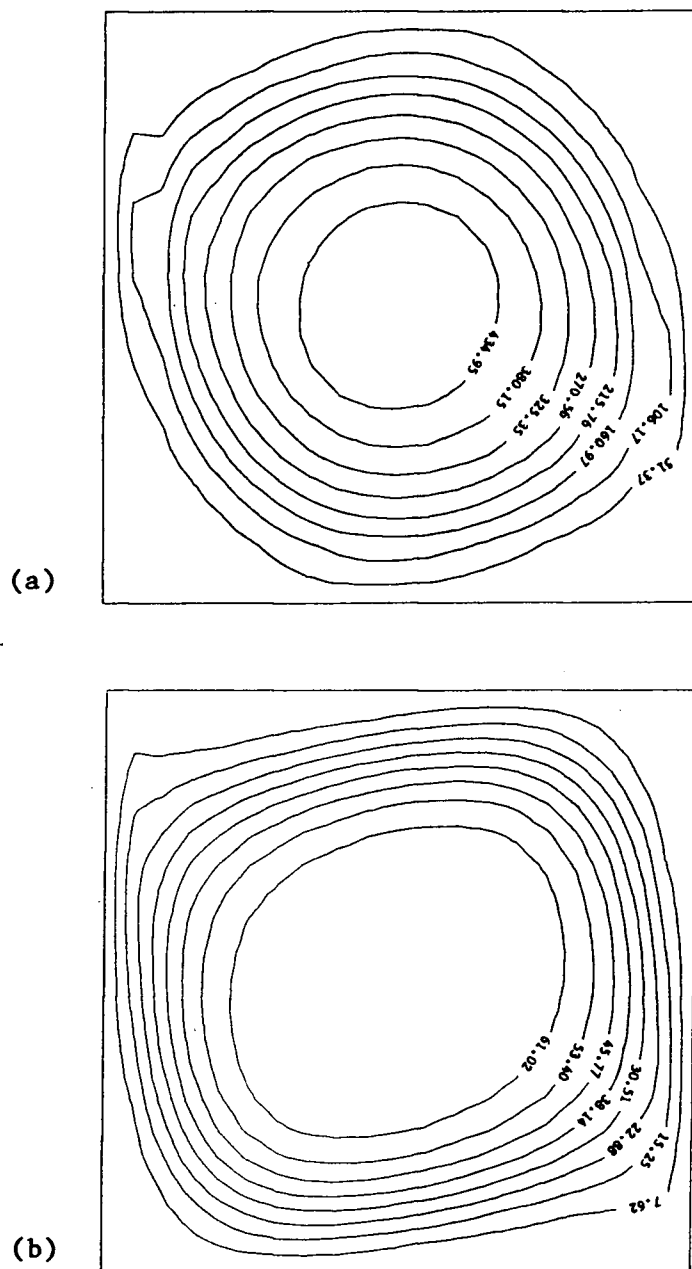


FIGURE 4.16 Streamline distribution for a temperature difference of 0.5°C across cell for (a) liquid tin ($\text{Pr}=0.0127$ and $\text{Gr}=1.8 \times 10^6$) and (b) liquid steel ($\text{Pr}=0.11$ and $\text{Gr}=3.0 \times 10^5$).

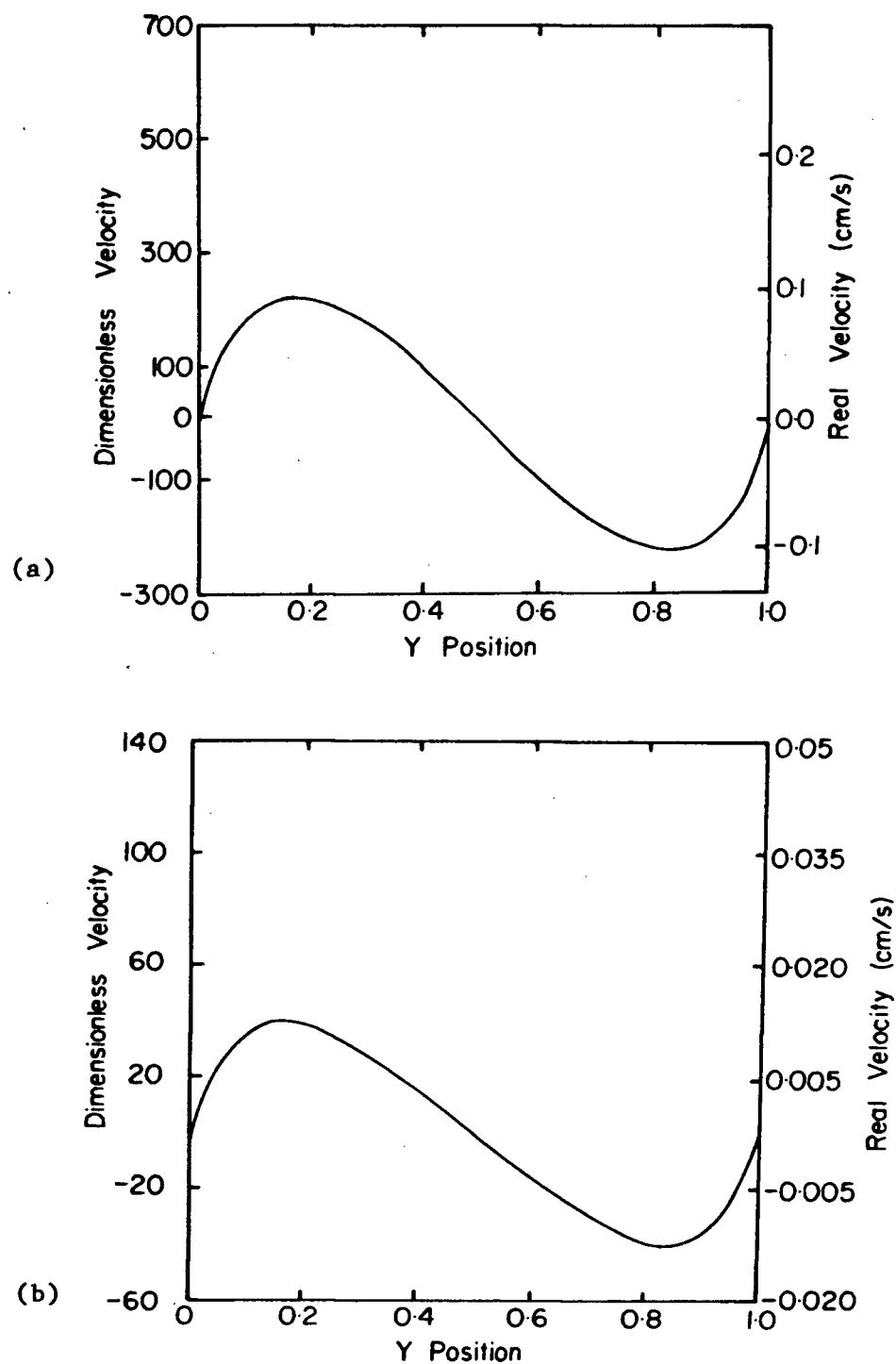


FIGURE 4.17 Vertical (x) velocity versus horizontal (y) position at $x=0.5$ for a temperature difference of 0.01°C across cell in (a) liquid tin ($Pr=0.0127$ and $Gr=3.6 \times 10^4$) and (b) liquid steel ($Pr=0.11$ and $Gr=6.0 \times 10^3$).

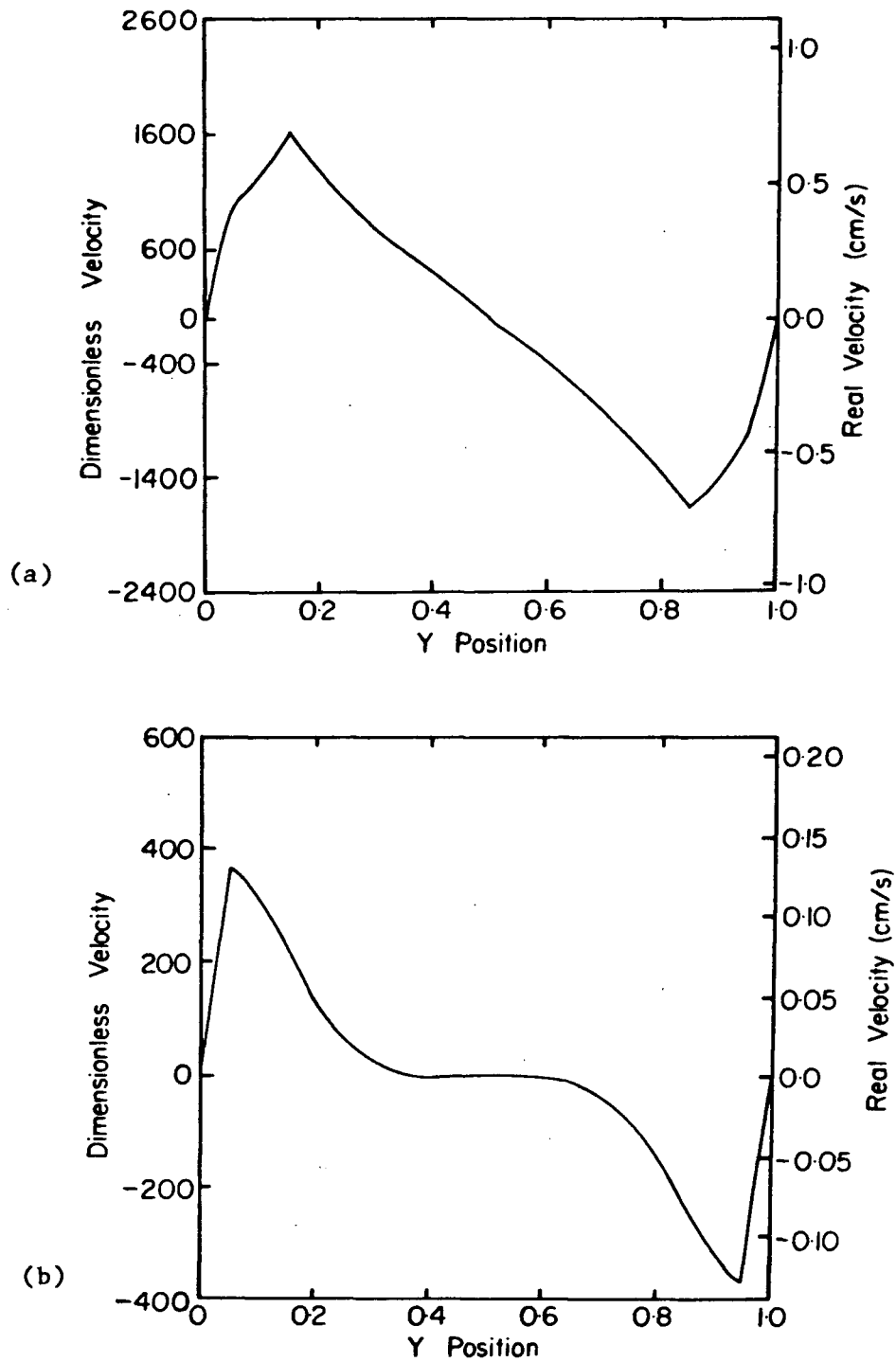


FIGURE 4.18 Vertical (x) velocity versus horizontal (y) position at $x=0.5$ for a temperature difference of 0.5°C across cell in (a) liquid tin ($Pr=0.0127$ and $Gr=1.8 \times 10^6$) and (b) liquid steel ($Pr=0.11$ and $Gr=3.0 \times 10^5$).

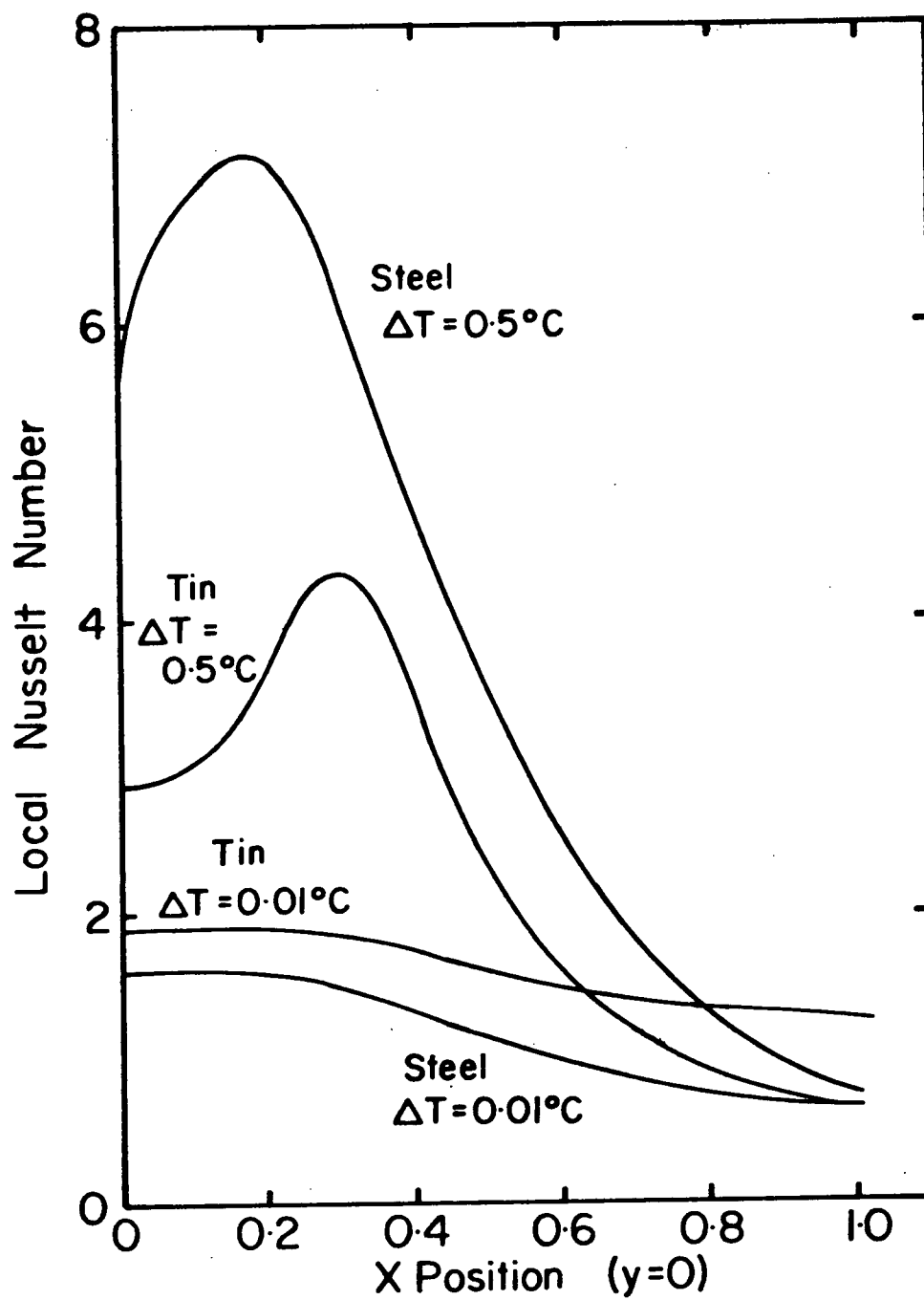


FIGURE 4.19 Plot of local Nusselt number versus position along cold wall for tin and steel at temperature differences of 0.01°C and 0.5°C .

velocities in liquid tin are much higher than those in liquid steel. The velocity scale for liquid tin is five times that for steel in Figure 4.17 and six times in Figure 4.18.

5.0 SUMMARY REMARKS

One of the aims of this study was to observe how the heat transfer changed with increasing convective flow in a liquid metal. The interest was in determining at what convective flow rate the heat transfer across the cell became independent of the degree of convection. As long as the heat transfer was related to the flow velocity then the degree of flow could not be ignored in mathematical models which estimate a value for the effective thermal conductivity. However once the linear limit was reached then it would only be important to know that fluid flow is present not the actual flow velocity.

Looking at the data from cell I, the heat transfer rate appeared to be linear over the entire range of temperature differences employed. However the linearity observed was probably due to the fact that the thermal resistance of the stainless steel end was higher than that for the convecting melt. In fact, the thermal conductivity of stainless is about one-half the thermal conductivity of stagnant liquid tin. This situation is opposite to the situation encountered in liquid-solid heat transfer in solidification. For most metals, the thermal conductivity of the solid state is higher than the thermal conductivity of the liquid state therefore the results from cell I were not representative of the behaviour during solidification.

The results from cell I raise some questions about a recent study²² which examined natural convective heat transfer across a parallelogrammic enclosure. In this study water and silicone oil were used as the experimental media. The cold end of the cell consisted of a copper plate immediately adjacent to the convecting fluid followed by a series of four glass plates which were the same thickness as the copper plate after which there was another copper plate. Thermocouples were positioned between the glass plates to measure the temperature differences across the plates. Knowing the thermal conductivity of the glass, the plates served as a heat flux meter. Since the thermal conductivity of glass is much lower than that for copper, the thermal resistance of the glass heat flux meter would be much higher than thermal resistance of the copper. In fact the thermal conductivity of glass is comparable to the stagnant thermal conductivity of water so that the thermal resistance of the glass plates was probably the same order of magnitude as the convecting fluid. Based on the results from cell I it seems likely that the heat transfer across the parallelogram was influenced by the heat flux meter.

To calculate a value for the effective thermal conductivity it is assumed that all heat flow is through the cold end. The difference in the slopes for the covered and uncovered cell indicate that the heat lost from the top of the cell cannot be ignored. The value of k_{eff} is approximately twenty percent lower using data from the covered cell than when using data from the uncovered cell. However the effect of the heat loss appears to a constant fraction of the heat transfer across the

cell so that the shape of the ΔT_{cold} versus ΔT_{melt} curve is not affected.

In the results from cell III, the behaviour at low flow rates was not clear. Using both argon cooling and the heater it was difficult to achieve temperature differences across the cell that were less than 3.5°C . Using only argon cooling, the data at the lower temperature differences is hard to interpret because the temperature difference across the bottom section of the cold end was negative. The negative sign means that heat should have been flowing into the cold end of the cell instead of out of the cell. Once the linear limit was reached, the magnitude of the effective thermal conductivity was calculated to be seven to ten times the thermal conductivity of stagnant liquid tin.

According to Figure 3.7, the temperature difference across the bottom section was higher than the temperature difference across the middle section implying higher heat transfer rates across the bottom of the cell. This situation is in direct conflict with the predictions of the computer model as reflected in the Nusselt number plots shown in Figures 4.5 and 4.19. According to these plots, the heat transfer rate at the bottom of the cold end should be less than that across the centre of the cold end. The highest heat transfer rates should be encountered at the top of the cell. Unfortunately data was not available for the upper section of the cold end but further experimentation is necessary to resolve the disagreement in the heat flow distribution.

REFERENCE LIST

1. Cole, G.S. and G.F Bolling, The Solidification of Metals, 1968, London, The Iron and Steel Institute, 323-329.
2. Lait, J.E., J.K. Brimacombe and F. Weinberg, Iron. and Steelmaking, 1974, No. 1, 35-42.
3. Mizakar, E.A., Trans. Met. Soc. AIME, 1969, vol 239, 1747-1753.
4. Szekely, J. and V. Stanek, Met. Trans., 1970, vol 1, 119-126.
5. Lait, J.E., J.K. Brimacombe and F. Weinberg, Iron. and Steelmaking, 1974, No. 2, 90-97.
6. MacAuley, L.C. and F. Weinberg, Met. Trans., 1973, Vol 4, 2097-2107.
7. Catton, I., Proc. Sixth Int. Heat Transfer Conf., 1978, 13-31.
8. Stewart, Murray, PhD Thesis, 1970, University of British Columbia.
9. Batchelor, G.K., Q. Appl. Math., 1954, Vol 12, 209-233.
10. Batchelor, G.K., J. Fluid Mech., 1956, Vol 1, 177.
11. Wilkes, J.O. and S.W. Churchill, A.I.Ch.E.J., 1966, Vol 12, 161-166.
12. De Vahl Davis, G., Int. J. Heat Mass Tran., 1968, Vol 11, 1675-1693.
13. Gershuni, G.Z., E.M. Zhukhouiskii and E.L. Tarunin, 1966, Mech, Liquids Gases, Akad. Sci. USSR No. 5, 56-62.
14. Poots, G., Q. J. Mech. Appl. Math., 1958, Vol 11, No 3, 257-273.

15. Szekely, J. and A.S. Jassal, Met. Trans. B, 1978, Vol 9B, 389-398.
16. Marr, H.S., Iron & Steel Int., 1979, 29-41.
17. Heaslip, L. et al., Proc. 2nd Process Technol. Conf., Chicago, 1981, AIME, 54-63.
18. Kohn, A., The Solidification of Metals, 1968, London, The Iron and Steel Institute, 415-420.
19. Moore, J.J., and N.A. Shah, Int. Met. Review, 1983, Vol 28, 338-356.
20. Blank, J.R. and F.B. Pickering, The Solidification of Metals, 1967, London, The Iron and Steel Institute, 370-376.
21. Szekely, J. and M.R. Todd, Int. J. Heat Mass Transfer, 1971, Vol 14, 467-482.
22. Maekawa, T. and I. Tanasawa, Proc. Seventh Int. Heat Transf. Conf., Munchen, Fed Rep Germany, Vol 2, 227-232.

APPENDIX ILIST OF SYMBOLS

C_p	= Specific heat
d	= Distance across cell
g	= Acceleration due to gravity
Gr	= Grashof number
Gr^*	= Modified Grashof number
h	= Heat transfer coefficient
k	= Thermal conductivity
k_{eff}	= Effective thermal conductivity
k_{Sn}	= Thermal conductivity of tin
L	= Characteristic length
Nu	= Nusselt number
P^*	= Pressure
P	= Dimensionless pressure
Pr	= Prandtl number
\dot{q}	= Heat flow rate
Ra	= Rayleigh number
t^*	= Time
t	= Dimensionless time
T^*	= Temperature
T	= Dimensionless temperature

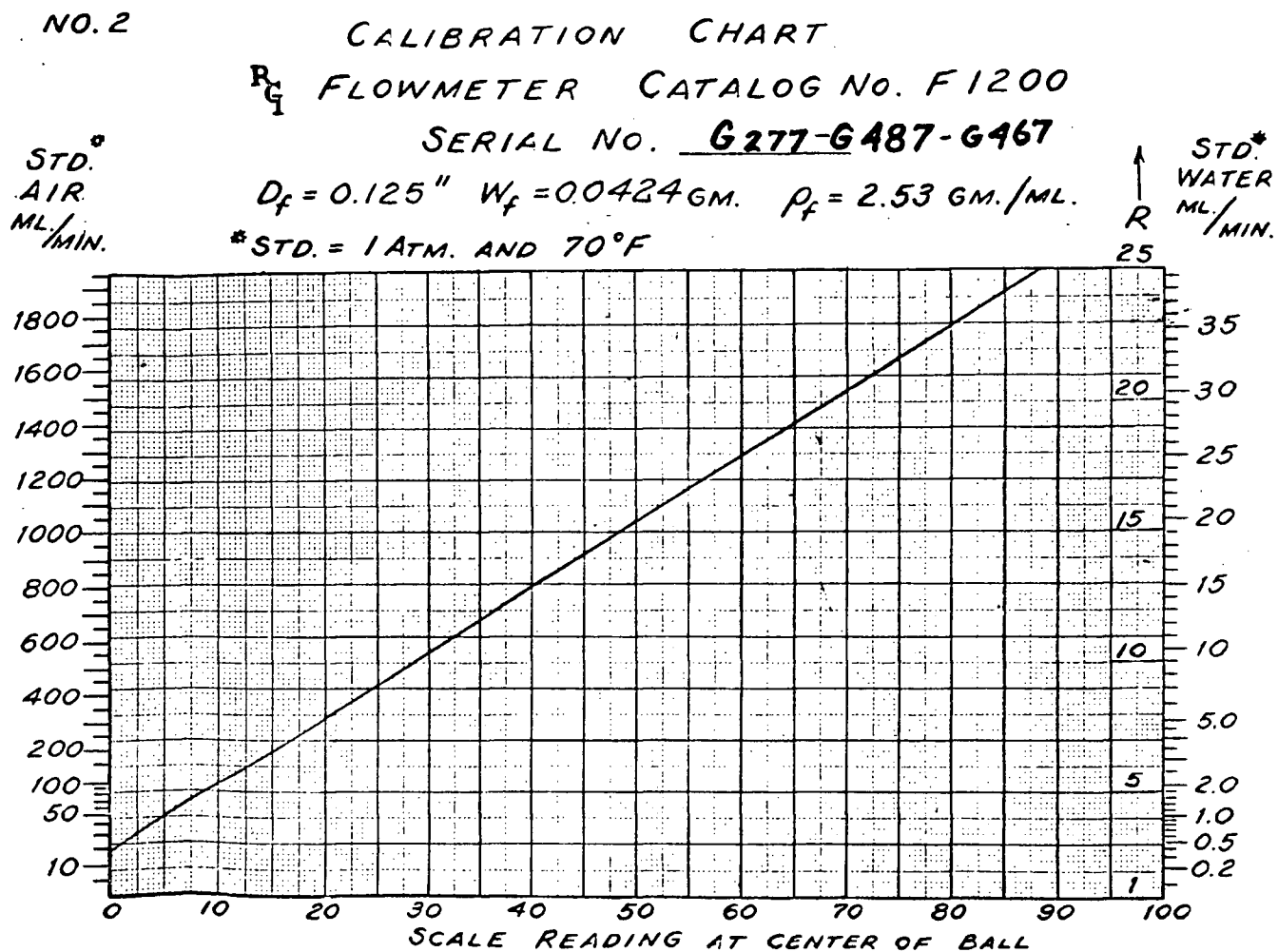
u^*	= Velocity in x-direction
u	= Dimensionless velocity in x-direction
v^*	= Velocity in y-direction
v	= Dimensionless velocity in y-direction
x^*	= Coordinate in vertical direction
x	= Dimensionless coordinate in vertical direction
y^*	= Coordinate in horizontal direction
y	= Dimensionless coordinate in horizontal direction

Greek symbols

β	= Thermal coefficient of expansion
ΔT	= Temperature difference
$\Delta \tau$	= Time step (computer program)
ξ	= Vorticity
μ	= Viscosity
ν	= Kinematic viscosity
ρ	= Density
ρ_m	= Mean density
ψ	= Stream function

APPENDIX II

Chart for Argon Flow Rate Conversion



```

1  C
2  C
3  C ***** THIS IS MODEL5 *****
4  C
5  C      THIS PROGRAM IS A MODIFICATION OF MODEL4
6  C      THIS VERSION ALLOWS THE TIME STEP TO BE CHANGED
7  C      AT ANY ARBITRARY ITERATION NUMBER(S)
8  C
9  C      INTEGER FL,FLAG,IFLAG,IERR
10 C
11 C      REAL*8 TA,TB,GR,PR,DT,DX,DY,DIF,DIFF,CHECK,SFC
12 C      REAL*8 C1,C2,C3,C4,C5,C6,C7,C8,C9,C10,C11,C12,C13,C14
13 C      REAL PCTHOT,PCTCOL
14 C
15 C      INPUT PRANDTL NUMBER (PR) ; GRASHOFF NUMBER (GR) ;
16 C      DELTA T (DT)
17 C
18 C      READ(6,20)PR,GR,DTA,DTB,DT,DT2
19 C      20 FORMAT(6F10.3)
20 C
21 C      SFC=0.08D0
22 C      LIM=21
23 C      DX=0.05D0
24 C      DY=0.05D0
25 C      TA=-1.0D0
26 C      TB= 1.0D0
27 C      N=441
28 C      REAL*8 T1(21,21),T2(21,21),X1(21,21),X2(21,21),S1(21,21),S2(21,21)
29 C      REAL*8 A(19),B(19),C(19),R(19),D(21),E(21),F(21),T(21)
30 C      REAL*8 U(21,21),V(21,21)
31 C
32 C      K1=2/DT2 + 2/DX**2
33 C      K2=2/DT2 - 2/DX**2
34 C      K3=2/DT2 + 2/DY**2
35 C      K4=2/DT2 - 2/DY**2
36 C      LI1=LIM-1
37 C      LI2=LIM-2
38 C      FLAG=0
39 C
40 C      INITIALIZE MATRICES
41 C
42 C      DO 50 J=1,LIM
43 C      DO 50 I=1,LIM
44 C      T1(I,J)=0.0
45 C      T2(I,J)=0.0
46 C      X1(I,J)=0.0
47 C      X2(I,J)=0.0
48 C      S1(I,J)=0.0
49 C      S2(I,J)=0.0
50 C      U(I,J) =0.0
51 C      50 V(I,J) =0.0
52 C
53 C      DO 54 I=1,19
54 C      A(I)=0.0
55 C      B(I)=0.0
56 C      C(I)=0.0
57 C      54 R(I)=0.0
58 C      DO 58 I=1,21

```

```

59      D(I)=0.0
60      E(I)=0.0
61      F(I)=0.0
62      58 T(I)=0.0
63      C
64      C
65      C LOADING FIXED TEMPERATURES
66      C
67      PCTHOT=0.0
68      PCTCOL=0.0
69      C
70      DO 60 I=1,LIM
71      T1(I,1)=TA+PCTCOL*I/LIM
72      T2(I,1)=TA+PCTCOL*I/LIM
73      T1(I,LIM)=(1-PCTHOT)*TB+PCTHOT*I/LIM
74      60 T2(I,LIM)=(1-PCTHOT)*TB+PCTHOT*I/LIM
75      C
76      C SOLVING FOR THE TEMPERATURES
77      C
78      C FIRST HALF OF TIME STEP
79      C
80      90 FLAG=FLAG +1
81      C
82      DT=DTA
83      IF (FLAG.GT.4) DT=DTB
84      IF (FLAG.GT.40) DT=DTC
85      C1=1/(2*DX)
86      C2=1/(2*DY)
87      C3=1/(PR*DX**2)
88      C4=1/(PR*DY**2)
89      C5=2/DT +2*C3
90      C6=2/DT -2*C3
91      C7=2/DT +2*C4
92      C8=2/DT -2*C4
93      C9=1/DX**2
94      C10=1/DY**2
95      C11=2/DT + 2*C9
96      C12=2/DT - 2*C9
97      C13=2/DT + 2*C10
98      C14=2/DT - 2*C10
99      WRITE(6, 93)FLAG
100     93 FORMAT(' ', ' START OF LOOP ',G6)
101     C
102     C
103     IFLAG=1.0
104     C
105     C SOLVING FOR COLUMNS 2 TO LIM-1
106     C
107     DO 110 J=2,LIM
108     DO 100 I=2,LIM
109     96 D(I)=-C1*U(I,J)-C3
110     E(I)=C5
111     F(I)= C1*U(I,J)-C3
112     100 T(I)=(C4+V(I,J)*C2)*T1(I,J-1)+(C4-V(I,J)*C2)*T1(I,J+1)
113     1+C8*T1(I,J)
114     D(I)=0
115     E(I)=C5
116     F(I)=-2*C3

```

```

117      T(1)=C4*T1(1,J-1)+C8*T1(1,J)+C4*T1(1,J+1)
118      D(LIM)=-2*C3
119      E(LIM)=C5
120      F(LIM)=0
121      T(LIM)=C4*T1(LIM,J-1)+C8*T1(LIM,J)+C4*T1(LIM,J+1)
122      CALL TRISLV(21,D,E,F,T,O,900)
123      DO 105 I=1,LIM
124      105 T2(I,J)=T(I)
125      110 CONTINUE
126      C
127      C
128      IFLAG=IFLAG+1
129      C
130      C
131      C SECOND HALF OF TIME STEP (TEMPERATURES)
132      C
133      C SOLVING FOR ROWS 2 TO LIM-1
134      C
135      DO 200 I=2,LI1
136      DO 175 J=3,LI2
137      K=J-1
138      A(K)=-V(I,J)*C2-C4
139      B(K)=C7
140      C(K)= V(I,J)*C2-C4
141      175 R(K)=(C3+U(I,J)*C1)*T2(I-1,J)+(C3-U(I,J)*C1)*T2(I+1,J)
142      1+C6*T2(I,J)
143      A(1)=0
144      B(1)=C7
145      C(1)= V(I,2)*C2-C4
146      R(1)=(C3+U(I,2)*C1)*T2(I-1,2)+(C3-U(I,2)*C1)*T2(I+1,2)
147      1+C6*T2(I,2)+(V(I,2)*C2+C4)*T1(I,1)
148      A(LI2)=-V(I,LI1)*C2-C4
149      B(LI2)=C7
150      C(LI2)=0
151      LI=LI1
152      R(LI2)=(C3+U(I,LI1)*C1)*T2(I-1,LI1)+(C3-U(I,LI1)*C1)*T2(I+1,LI1)
153      1+C6*T2(I,LI1)+(C4-V(I,LI1)*C2)*T1(I,LIM)
154      CALL TRISLV(19,A,B,C,R,O,900)
155      DO 180 J=2,LI1
156      K=J-1
157      180 T1(I,J)=R(K)
158      200 CONTINUE
159      C
160      C TOP ROW
161      C
162      DO 220 J=2,LI1
163      K=J-1
164      A(K)=-C4
165      B(K)=C7
166      C(K)=-C4
167      220 R(K)=C6*T2(1,J)+2*C3*T2(2,J)
168      A(1)=0
169      B(1)=C7
170      C(1)=-C4
171      R(1)=C6*T2(1,2)+2*C3*T2(2,2) +C4*T1(1,1)
172      A(LI2)=-C4
173      B(LI2)=C7
174      C(LI2)=0

```



```

175      R(LI2)=C6*T2(1,LI1)+2*C3*T2(2,LI1) +C4*T1(1,LIM)
176      CALL TRISLV(19,A,B,C,R,O,900)
177      DO 240 J=2,LI1
178          K=J-1
179      240 T1(1,J)=R(K)
180      C
181      C  BOTTOM ROW
182      C
183          DO 250 J=2,LI1
184              K=J-1
185              A(K)=-C4
186              B(K)=C7
187              C(K)=-C4
188      250 R(K)=C6*T2(LIM,J)+2*C3*T2(LI1,J)
189              A(1)=0
190              B(1)=C7
191              C(1)=-C4
192              R(1)=C6*T2(LIM,2)+2*C3*T2(LI1,2) +C4*T1(LIM,1)
193              A(LI2)=-C4
194              B(LI2)=C7
195              C(LI2)=0
196              R(LI2)=C6*T2(LIM,LI1)+2*C3*T2(LI1,LI1) +C4*T1(LIM,LIM)
197              CALL TRISLV(19,A,B,C,R,O,900)
198              DO 260 J=2,LI1
199                  K=J-1
200      260 T1(LIM,J)=R(K)
201      C
202      C
203      C
204          IFLAG=IFLAG+1
205      C
206      C  INTERIOR VORTICITIES
207      C  FIRST HALF OF TIME STEP
208      C
209      C  SOLVING FOR COLUMNS 2 TO LIM-1
210      C
211          DO 310 J=2,LI1
212          DO 300 I=3,LI2
213              K=I-1
214              A(K)=-U(I,J)*C1-C9
215              B(K)=C11
216              C(K)= U(I,J)*C1-C9
217      300 R(K)=(C10+V(I,J)*C2)*X1(I,J-1)+(-V(I,J)*C2+C10)*X1(I,J+1)
218              1+C14*X1(I,J)+GR*C1*(T1(I,J+1)-T1(I,J-1))
219              A(1)=0
220              B(1)=C11
221              C(1)= U(2,J)*C1-C9
222              R(1)=(C10+V(2,J)*C2)*X1(2,J-1)+(-V(2,J)*C2+C10)*X1(2,J+1)
223              1+C14*X1(2,J)
224              1+GR*C1*(T1(2,J+1)-T1(2,J-1))+(C9+U(2,J)*C1)*X2(1,J)
225              A(LI2)=-U(LI1,J)*C1-C9
226              B(LI2)=C11
227              C(LI2)=0
228              R(LI2)=C14*X1(LI1,J)+(C9-U(LI1,J)*C1)*X2(LIM,J)
229              1+(C10+V(LI1,J)*C2)*X1(LI1,J-1)+(-V(LI1,J)*C2+C10)*X1(LI1,J+1)
230              1+GR*C1*(T1(LI1,J+1)-T1(LI1,J-1))
231              CALL TRISLV(19,A,B,C,R,O,900)
232      DO 305 I=2,LI1

```

```

233      K=I-1
234      305 X2(I,J)=R(K)
235      310 CONTINUE
236      C
237      C
238      C
239      IFLAG=IFLAG+1
240      C
241      C SECOND HALF OF TIME STEP (VORTICITIES)
242      C
243      C SOLVING FOR ROWS 2 TO LIM-1
244      C
245      DO 350 I=2,LI1
246      DO 340 J=3,LI2
247      K=J-1
248      A(K)=-V(I,J)*C2-C10
249      B(K)=C13
250      C(K)= V(I,J)*C2-C10
251      340 R(K)=(C9+U(I,J)*C1)*X2(I-1,J)+(C9-U(I,J)*C1)*X2(I+1,J)
252      1+GR*C1*(T1(I,J+1)-T1(I,J-1))+C12*X2(I,J)
253      A(1)=0
254      B(1)=C13
255      C(1)= V(I,2)*C2-C10
256      R(1)=(C9+U(I,2)*C1)*X2(I-1,2)+(C9-U(I,2)*C1)*X2(I+1,2)
257      1+C12*X2(I,2)
258      1+GR*C1*(T1(I,3)-T1(I,1))+(V(I,2)*C2+C10)*X1(I,1)
259      A(LI2)=-V(I,LI1)*C2-C10
260      B(LI2)=C13
261      C(LI2)=0
262      LI=LI1
263      R(LI2)=(C9+U(I,LI1)*C1)*X2(I-1,LI1)+(C9-U(I,LI1)*C1)*X2(I+1,LI1)
264      1+C12*X2(I,LI1)+(-V(I,LI1)*C2+C10)*X1(I,LIM)
265      1+GR*C1*(T1(I,LIM)-T1(I,LI2))
266      CALL TRISLV(19,A,B,C,R,O,900)
267      DO 345 J=2,LI1
268      K=J-1
269      345 X1(I,J)=R(K)
270      C
271      350 CONTINUE
272      C
273      C
274      C
275      IFLAG=IFLAG+1
276      C
277      C STREAM FUNCTION
278      C FIRST HALF OF TIME STEP
279      C
280      FL=0
281      360 FL=FL+1
282      DO 400 J=2,LI1
283      DO 375 I=3,LI2
284      K=I-1
285      A(K)=-C9
286      B(K)=K1
287      C(K)=-C9
288      375 R(K)=X1(I,J)+C10*S1(I,J-1)+K4*S1(I,J)+C10*S1(I,J+1)
289      A(1)=0
290      B(1)=K1

```

```

291      C(1)=-C9
292      R(1)=X1(2,J)+C10*S1(2,J-1)+K4*S1(2,J)+C10*S1(2,J+1)
293      A(LI2)=-C9
294      B(LI2)=K1
295      C(LI2)=0
296      R(LI2)=X1(LI1,J)+C10*S1(LI1,J-1)+K4*S1(LI1,J)+C10*S1(LI1,J+1)
297      CALL TRISLV(19,A,B,C,R,O,900)
298      DO 380 I=2,LI1
299      K=I-1
300      380 S2(I,J)=R(K)
301      C
302      400 CONTINUE
303      C
304      C
305      IFLAG=IFLAG+1 -(FL-1)
306      C
307      C SECOND HALF OF TIME STEP (STREAM FUNCTION)
308      DO 475 I=2,LI1
309      DO 450 J=3,LI2
310      K=J-1
311      A(K)=-C10
312      B(K)=K3
313      C(K)=-C10
314      450 R(K)=X1(I,J)+C9*S2(I-1,J)+K2*S2(I,J)+C9*S2(I+1,J)
315      A(1)=0
316      B(1)=K3
317      C(1)=-C10
318      R(1)=X1(I,2)+C9*S2(I-1,2)+K2*S2(I,2)+C9*S2(I+1,2)
319      A(LI2)=-C10
320      B(LI2)=K3
321      C(LI2)=0
322      R(LI2)=X1(I,LI1)+C9*S2(I-1,LI1)+K2*S2(I,LI1)+C9*S2(I+1,LI1)
323      CALL TRISLV(19,A,B,C,R,O,900)
324      DO 460 J=2,LI1
325      K=J-1
326      460 S1(I,J)=R(K)
327      C
328      475 CONTINUE
329      C
330      IFLAG=IFLAG+1 -(FL-1)
331      C
332      C CHECK FOR CONVERGENCE OF STREAM FUNCTION
333      C
334      IF (FL.GT.50) GO TO 1000
335      TEST=C9*(4*S1(2,2)-S1(2,3)-S1(3,2))
336      IF (X1(2,2).EQ.O) GO TO 520
337      CHECK=(TEST-X1(2,2))/X1(2,2)
338      IF (FLAG.GT.10) SFC=0.05
339      IF (FLAG.GT.22) SFC=0.02
340      IF (CHECK.GT.SFC) GO TO 360
341      C
342      520 CONTINUE
343      C
344      C CALCULATION OF VELOCITIES
345      C
346      DO 550 I=2,LI1
347      DO 525 J=3,LI2
348      525 U(I,J)=(S1(I,J-2)-8*S1(I,J-1)+8*S1(I,J+1)-S1(I,J+2))/(12*DY)

```

```

349      U(I,2)=(-3*S1(I,2)+6*S1(I,3)-S1(I,4))/(6*DY)
350 550 U(I,LI1)=-(-3*S1(I,LI1)+6*S1(I,LI1-1)-S1(I,LI1-2))/(6*DY)
351      DO 600 J=2,LI1
352      DO 575 I=3,LI2
353 575 V(I,J)=(-S1(I-2,J)+8*S1(I-1,J)-8*S1(I+1,J)+S1(I+2,J))/(12*DX)
354      V(2,J)=(3*S1(2,J)-6*S1(3,J)+S1(4,J))/(6*DX)
355 600 V(LI1,J)=-(-3*S1(LI1,J)-6*S1(LI1-1,J)+S1(LI1-2,J))/(6*DX)
356 C
357 C
358 C
359 C
360 C
361 C CALCULATION OF BOUNDARY VORTICITIES
362      DO 625 J=2,LI1
363      X2(1,J)=-2*S1(2,J)*C9
364      X1(1,J)=X2(1,J)
365      X2(LIM,J)=-2*S1(LI1,J)*C9
366 625 X1(LIM,J)=X2(LIM,J)
367      DO 650 I=2,LI1
368      X2(I,1)=-2*S1(I,2)*C10
369      X1(I,1)=X2(I,1)
370      X2(I,LIM)=-2*S1(I,LI1)*C10
371 650 X1(I,LIM)=X2(I,LIM)
372 C
373 C
374 C
375 C CONVERGENCE CHECK OF TEMPERATURES
376 C
377      DIF=0
378      IF (FLAG.GT.700) GO TO 720
379      DO 700 J=2,20
380      DO 700 I=2,20
381      IF (T1(I,J).NE.0) DIFF=(T1(I,J)-T2(I,J))/T1(I,J)
382      IF (DABS(DIFF).GT.DIF) DIF=DABS(DIFF)
383 700 CONTINUE
384      IF (DIF.GT.0.005) GO TO 90
385 C
386      GO TO 725
387 720 WRITE(6,721)
388 721 FORMAT(' ','***** INTERRUPT IN EFFECT ')
389 C
390 C
391 725 CONTINUE
392 C
393 C
394 C OUTPUT TEMPERATURES AND VELOCITIES
395 C
396      DO 880 I=1,LIM
397      WRITE(6,850)I
398 850 FORMAT(' ','DATA FOR ROW NUMBER ',G5)
399      WRITE(6,860)(T1(I,J),J=1,LIM)
400      WRITE(6,865)(U(I,J),J=1,LIM)
401      WRITE(6,870)(V(I,J),J=1,LIM)
402 860 FORMAT(' ','TEMPERATURES:',21F9.6)
403 865 FORMAT(' ','X-VELOCITY:',21F10.3)
404 870 FORMAT(' ','Y-VELOCITY:',21F10.3)
405 880 CONTINUE
406 C

```

```

407      GO TO 3000
408      C
409      C *****
410      C
411      C ERROR STATEMENTS ASSOCIATED WITH TRISLV
412      C
413      C *****
414      C
415      900 WRITE(6,960) IFLAG
416      960 FORMAT(' ', ' SOLVE COULD NOT FIND A SOLUTION, FLAG = ',I6)
417      GO TO 3000
418      C
419      1000 CONTINUE
420      C INSERT WRITE STATEMENT WHICH SAYS STREAM FUNCTION NOT
421      C CONVERGING AFTER 10 ITERATIONS
422      C
423      WRITE(6,1200)
424      1200 FORMAT(' ', 'STREAM FCN NOT CONVERGING')
425      C
426      DO 1600 J=1,LIM
427      WRITE(6,1500)S1(2,J),S2(2,J)
428      1500 FORMAT(' ', 'S1 = ',F16.4,' S2= ',F16.4)
429      1600 CONTINUE
430      C
431      C
432      WRITE(6,1610)FLAG,CHECK
433      1610 FORMAT(' ', ' NO. OF LOOPS RUN = ',G8,' CHECK = ',F16.5)
434      C
435      C
436      GO TO 3000
437      C
438      2000 CONTINUE
439      C INSERT WRITE STATEMENT WHICH SAYS TEMPERATURES NOT CONVERGING
440      C
441      WRITE (6,2200)
442      2200 FORMAT(' ', 'TEMPERATURES NOT CONVERGING')
443      C
444      C
445      DO 2300 I=1,21
446      WRITE(6,2250)(T2(I,J),J=1,5)
447      2250 FORMAT(' ',5F16.5)
448      2300 CONTINUE
449      C
450      WRITE(6,2325)
451      2325 FORMAT(' ', 'STREAM FUNCTION')
452      C
453      DO 2400 I=2,20
454      WRITE(6,2350)(S1(I,J),J=1,5)
455      2350 FORMAT(' ',5F16.5)
456      2400 CONTINUE
457      C
458      GO TO 3000
459      C
460      3000 CONTINUE
461      C
462      STOP
463      END

```